Review of unsteady transonic aerodynamics: Theory and applications

Oddvar O. Bendiksen

Mechanical and Aerospace Engineering Department, University of California, Los Angeles, CA 90095-1597, USA

ARTICLE INFO

ABSTRACT

Unsteady transonic flow theory is reviewed and classical results from the nonlinear asymptotic theory are combined with new results from computational fluid dynamics. The emphasis is on applications to the field of aeroelasticity and on clarifying the limitations of linearized theories in problems involving mixed subsonic–supersonic flows. The inherent differences between nonlinear transonic aerodynamics and linear subsonic and supersonic aerodynamics are considered from a theoretical and computational standpoint, and the practical implications of these differences in formulating suitable aerodynamic models for aeroelastic stability calculations are discussed. Transonic similarity principles are reviewed and their relevance in understanding flutter, divergence, and control reversal phenomena of transonic aircraft is illustrated through practical examples.

© 2010 Elsevier Ltd. All rights reserved.

Contents

E-mail address: oddvar@seas.ucla.edu

1. Introduction

Transonic flows occur over aircraft flying near Mach 1, in the tip region of propeller blades, and in nozzles, turbines and compressors of jet engines. Transonic flows can be loosely defined as flows in which the local flow speed is close to the speed of sound. More precisely, a flow is considered transonic if both subsonic and supersonic regions exist near the body at the same time. For example, if an aircraft is flying at a subsonic speed ($M_\infty < 1$), local regions of supersonic flow will form on the wing surface if the flight Mach number M_∞ is above the so-called critical Mach number M_{cr} for the wing. The critical Mach number depends on the shape, thickness, and attitude of the wing–body combination, but typically falls in the range 0.6–0.8 for most aircraft under normal steady flight conditions such as cruise.

The theoretical study of transonic flow problems associated with aircraft started with von Kármán's 1947 paper on transonic similarity principles [1]. A series of theoretical and experimental studies followed, including the Ph.D. Thesis of Cole [2] and papers by Guderley and Yoshihara [3], Cole [4], Spreiter [5,6], Hayes [7], and Cole and Messiter [8]. Early experimental work on shock-boundary-layer interactions by Liepmann et al. [9] and by Ackeret et al. [10] are representative of the increasing interest in transonic flows relevant to emerging high-speed aircraft in the early years after World War II. By the time the books on the subject by Guderley [11] and Ferrari and Tricomi [12] appeared, a relatively good mathematical and physical understanding of steady transonic flow had been developed, at least for the two-dimensional inviscid case. At the same time as Ref. [12] came out (1968), Cole's text on perturbation methods [13] was published, wherein he presented a more modern mathematical approach to transonic flow problems based on the method of matched asymptotic expansions, pioneered by himself and Lagerstrom [14] over the previous 20 years. Later monographs on transonic flow that are relevant to the present review include the books by Cole and Cook [15], Moulden [16], Ramm [17], and Kuz'min [18]. See also the proceedings from the series of *Symposium Transsonicum* held between 1962 and 2002 [19–22] and the collection of papers in Vol. 12 of *Progress in Astronautics and Aeronautics* [23].

The year 1968 also marks the beginning of new developments in transonic flow research, brought about by a renewed interest in the transonic effects experienced by transport aircraft cruising at high subsonic Mach numbers. The first generation of US commercial jet aircraft was by then 10 years old, and the new "wide-body" or jumbo aircraft were in flight tests and about to enter service. The scientific computer was rapidly becoming a powerful tool in aerodynamic and structural analysis and design, including flutter calculations. Although computational procedures based on linear potential flow were well advanced at this point, these methods did not apply to the mixed subsonic–supersonic flow-fields encountered in transonic flows over aircraft wings.

Not much progress was made on calculating transonic flows until methods were developed to handle the mixed subsonic–supersonic flow-field in a mathematically and physically correct manner. A major step in this direction was the introduction of type-dependent difference formulas by Murman and Cole in a seminal paper published in 1971 [24]. Separate difference formulas were used in the elliptic and hyperbolic regions of the transonic small disturbance equation, to account for the local domain of dependence of the potential at a given point in the subsonic or supersonic regions. The discretized equations were solved numerically using an iterative line relaxation algorithm.

The publication of the Murman–Cole paper had an immediate impact on the calculation of transonic flows over aircraft wings and provided an important impetus to the emerging field of computational fluid dynamics (CFD). Over the next 20 years, rapid advances were made in the calculation of steady and unsteady transonic flows, from simple two-dimensional airfoils to the flow around a complete aircraft. At the same time, the application of these methods in computational aeroelasticity saw an explosive growth that continues to this day. For a brief historical review of the development of computational techniques for transonic flows, see Caughey and Jameson [25]. For a detailed discussion of the numerical challenges involved in the application of CFD to aircraft design, see Jameson [26].

The objective of this paper is to present a review of the theory of transonic aerodynamics and its implications in developing mathematical and CFD-based methods for unsteady transonic flows. The aim is not to give an in-depth presentation of the complete theory or all relevant computational methods or codes, but to use a combination of theoretical considerations, computational studies, and experimental data, to reach conclusions or formulate guiding principles that might be useful to the flutter engineer as well as the aircraft designer. The emphasis is on the mathematical theory and the physics it predicts at various levels of approximation, and on the differences between transonic and subsonic or supersonic flows and their implications.

Because transonic flutter prediction is such an important problem in aircraft design, much of the application section of this review will focus on the role that unsteady transonic flow theory plays in the field of modern aeroelasticity. Large commercial and military transport aircraft cruise at transonic Mach numbers, above the critical Mach number at which locally sonic flow first occurs, but below Mach 1. Supersonic transport and fighter aircraft must also be capable of sustained operation near Mach 1, where the flutter margin is typically at a minimum and non-classical flutter behaviors are often observed. Transonic flutter of aircraft wings and control surfaces are dominated by the inherent nonlinearities in the unsteady transonic flow, resulting from moving shocks on the wing surface and from shock-boundary layer interactions.

Previous reviews relevant to this paper include the reviews of CFD-based unsteady aerodynamics and aeroelasticity by Edwards and Malone [27], Edwards [28], and Bendiksen [29]. See also the classic reviews of transonic aerodynamic theory by Cole [30] and of unsteady transonic aerodynamics (experimental and theoretical) by Tijdeman and Seebass [31]. The reviews of nonlinear aeroelasticity by Dowell et al. [32], and nonlinear aeroelastic

prediction by de C. Henshaw et al. [33], are also of interest, although their primary focus is not on unsteady transonic aerodynamics.

Although the present review will deal exclusively with non-linear transonic flows, the 1961 monograph by Landahl on (linear) unsteady transonic flows [34] is still of interest, because of its many insightful discussions on the propagation of acoustic waves in a nonuniform transonic flow. See also his review article in Symposium Transsonicum II (1976) [35]. Reviews of computational approaches to linearization of unsteady aerodynamics and the corresponding aeroelastic problems can be found in Refs. [33,36].

2. Nonlinear aspects of transonic flow

2.1. Mixed subsonic–supersonic flow

At transonic flight Mach numbers above the critical Mach number for an aircraft wing, in the Mach number range $M_{cr} < M_\infty \approx 1$, local regions of embedded supersonic flow exist on and near the wing surface, as shown in Fig. 1. At the aft end of these regions, the flow is decelerated to subsonic speeds through a nearly normal shock wave. As the wing deforms in response to unsteady loads, the supersonic regions grow and shrink in harmony with the wing motion; thus the shocks move along the wing surface, changing in strength and possibly vanishing over part of the oscillation cycle. These moving shocks play an important role in some of the highly nonlinear flutter behaviors observed at Mach numbers near one. In order to model an aeroelastic system with mixed subsonic–supersonic flow-field with moving shocks, nonlinear field equations are required.

2.2. Why linear theory fails

Transonic flow over aircraft wings is inherently nonlinear, even in the limit of small disturbances. The nonlinearities arise because (1) the geometry of the wing (thickness, camber, and airfoil type) and angle of attack enter the first-order perturbation solution in a nonlinear manner; and (2) the mixed subsonic flow-field with moving shocks cannot be modeled with linear equations, even in the absence of boundary layer separation.

With respect to the effect of airfoil geometry and angle of attack, experimental evidence also points to the need for a nonlinear equation, even for small disturbances. It is not possible to explain the observed sensitivity of the transonic flutter boundaries to wing thickness and angle of attack, as shown

in Figs. 2 and 3, based on linear theories. Linearized aerodynamics implies that the effects of thickness, camber, and angle-of-attack should be of second order, because the superposition principle can be used to "remove" these effects from the first-order unsteady problem; i.e., it suffices to consider an oscillating flat plate, as in the Theodorsen theory. Figs. 2 and 3 show that this assumption is not correct in the transonic region, and that the effects of thickness and angle of attack are in fact of first order.

Furthermore, if thickness is a second-order effect, one would expect that the thinner wings in Fig. 2 should be less affected. However, the wind tunnel data show exactly the opposite to be true. Also, the airfoil shape becomes of importance, and there is often a significant difference between the flutter boundary of a wing with a supercritical airfoil, as compared to conventional wings of similar thickness. But the most intriguing aspect of transonic flutter is the appearance of a *transonic dip* in the flutter boundary, as shown in Figs. 2 and 3, revealing a much higher and
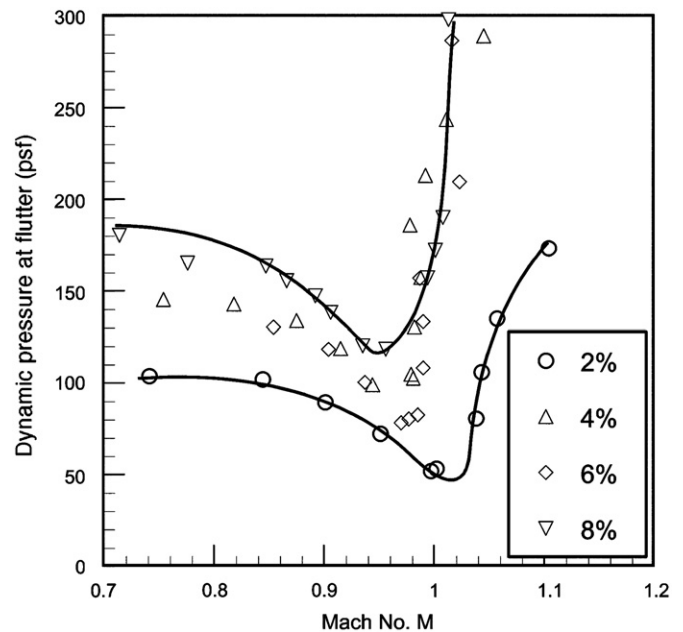
Fig. 2. Effect of wing thickness on the flutter boundary and transonic dip of the swept NACA 65A-series wings of different airfoil thickness tested by Doggett et al. [37] (fixed mass and stiffness properties).
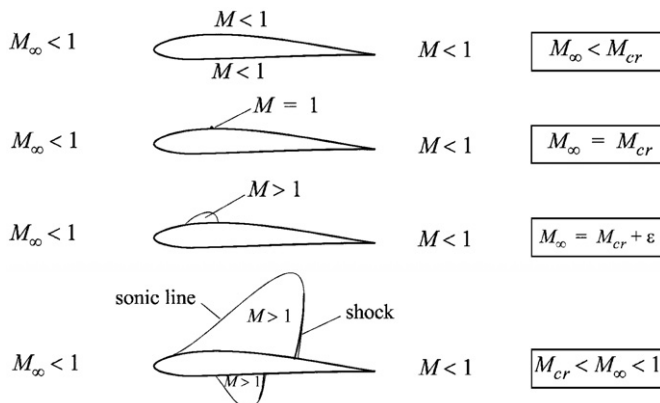
Fig. 1. Flow patterns about airfoils and wings in sub-transonic (subsonic) and transonic flows without boundary layer separation.
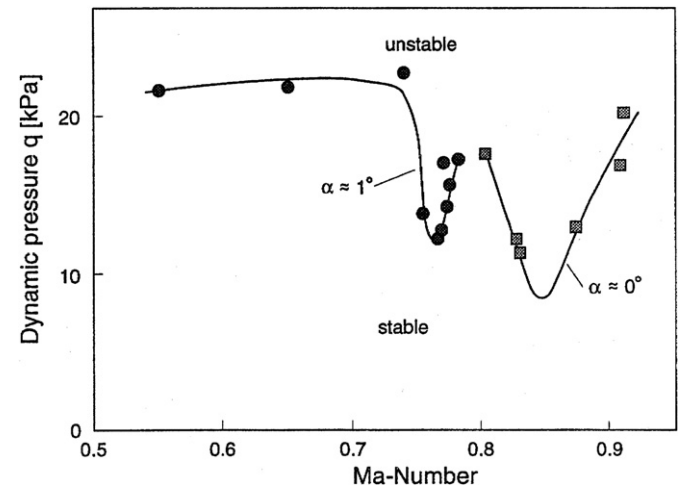
Fig. 3. Effect of angle of attack on the experimental flutter boundary and transonic dip of the NRL7301 2D aeroelastic model tested by Schewe et al. [38].

very different sensitivity to Mach number than suggested by the linearized aerodynamic theories. For some wings, a change of only 0.02 in the Mach number in the dip region can result in as much as a 50% change in the critical dynamic pressure at flutter.

The second and perhaps more fundamental reason why nonlinear governing equations are required to model transonic flows is of a mathematical nature and is based on the theory of partial differential equations. First, even in the steady limit, the governing equation(s) must be able to change type, from locally elliptic in the subsonic regions, to locally hyperbolic in the supersonic regions. The spatial extent of the local supersonic or subsonic region is not known in advance but must be determined as part of the solution, again requiring a nonlinear equation to describe the physics. Second, a nonlinear equation is also necessary to model moving shock waves and to obtain the correct time-varying Rankine–Hugoniot shock jump conditions.

2.3. Nonuniformities

Two types of nonuniformities appear in steady and unsteady transonic flow problems: nonuniformities with respect to a parameter, such as the Mach number, and nonuniformities with respect to the coordinates (space and time). By nonuniformities we mean that the solution may not be uniformly valid in space and/or time, or may break down or blow up for certain values of a parameter. The theoretical, computational, and experimental difficulties caused by these nonuniformities are best illustrated through examples.

Both parametric and coordinate-type nonuniformities can occur if an invalid linearization of the governing equations and boundary conditions is used. In the strongly nonlinear region near the transonic dip, no uniformly valid linearization of the unsteady aerodynamic problem is possible. It can be shown that the corresponding perturbation problem is singular in the terminology of the mathematical theory of perturbation analysis and that a regular perturbation expansion will fail. The singularity is of the cumulative or secular type [7,39,40], in the sense that the nonlinear terms neglected in the linearization never become large, but their cumulative effects over large distances or large time intervals grow and eventually become of order one, thus destroying the uniform validity of the linearized solution. That this might happen for finite amplitude wing motion is not surprising; what is surprising is that the nonuniformities persist down to the limit of infinitesimal motion. The only difference is that the time scale over which this happens increases as the amplitudes decrease. But if one waits long enough, the linear solution gradually drifts away from the nonlinear solution, until the error becomes of order one. The consequences of the temporal and spatial nonuniformities are more severe in the aeroelastic stability problem, for the obvious reason that we are interested in the *global stability* of the fluid–structure system, and local or short-time stability is not sufficient and is hence only of secondary interest.

2.4. Limitations of linear theory near Mach 1

Classical linear theory of potential flow has a singularity at Mach one, predicting infinite aerodynamic loads. But this singularity is artificial and somewhat misplaced, because the linear theory breaks down as soon as the critical Mach number is exceeded and well before Mach 1 is reached. The breakdown is of a mathematical rather than a physical nature; that is, the magnitudes of certain terms in the perturbation expansion have been estimated incorrectly. The reason for this failure can be traced back to the *linear* governing equation, which only permits

pressure disturbances to travel away from the wing as linear acoustic waves at a constant speed, the speed of sound a_∞ in the free stream. If the wing is traveling with a relative speed U_∞ with respect to the air, upstream propagating wave fronts will accumulate and stay near the wing if the Mach number $M_\infty = U_\infty / a_\infty$ is close to one, resulting in a large disturbance that violates the small-disturbance assumption. The result is a blow-up of the solution at $M_\infty = 1$, which introduces the well-known $1/\sqrt{1 - M_\infty^2}$ Prandtl–Glauert singularity in the aerodynamic coefficients.

To remove these infinities, we must remove the artificial restriction of a constant wave speed, and allow the local speed of sound to vary as a nonlinear function of the local disturbance, thus permitting the waves to radiate away from the wing. Elementary wave theory tells us that a nonlinear governing equation is required, even in the limit of small disturbances. Thus, linear potential theory, or *any linear theory* for that matter cannot describe the physics involved and cannot lead to a uniformly valid solution. This does not necessarily mean that linear theories are useless in practical engineering applications involving transonic flows, only that such theories must by their very nature be "local". That is, their domain of validity in space and time is restricted, often so severely as to render them of limited use in aeroelastic stability calculations.

3. Mathematical models for unsteady transonic flow

3.1. Modeling hierarchy

The modeling of unsteady transonic flow has been shown in an approximate hierarchal order in Fig. 4, based on the physical fidelity of the approximations involved. Not all approximations have been included, only the more useful ones in aeroelastic applications. We will discuss the various models in order of increased complexity, starting with classical linear aerodynamics.

3.2. Linear potential equation

Consider a thin planar wing, as shown in Fig. 5. By scaling the wing profile, one can consider a family of wings of the same basic shape

$$F_{u,l}(x,y) = \delta f_{u,l}(x,y) \tag{1}$$

where δ is a nondimensional thickness or scaling parameter and $f_{u,l}(x,y)$ represents the basic rigid or "jig" wing shape, i.e., the
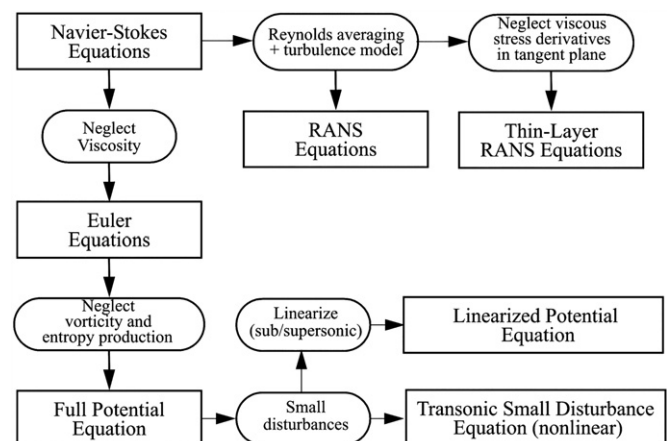

Fig. 4. Unsteady aerodynamics modeling hierarchy in computational fluid dynamics and aeroelasticity.
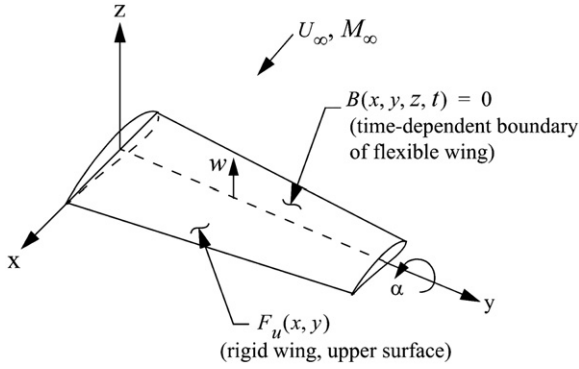
Fig. 5. Wing coordinate system and surface definition.

Fig. 6. Kutta–Joukowski condition at the trailing edge.

ordinate z of a point on the wing surface, as a function of x and y. Here, the subscripts u and l are used to denote the upper and lower surfaces of the wing, and the shape function for the rigid wing is given (approximately) by

$$f_{u,l}(x,y) \cong z_c(x,y) \pm z_t(x,y) \tag{2}$$

where $z_c(x,y)$ and $z_t(x,y)$ are the camber and thickness distributions, respectively. Although the trim angle of attack $\alpha_0(y)$ of the wing can be included in the definition of $f_{u,l}(x,y)$, it is convenient in the unsteady case to consider α_0 as part of the total angle of attack.

At Mach numbers outside the transonic region, the unsteady aerodynamics problem can be linearized for small-amplitude disturbances. In this case, a regular perturbation expansion for the velocity potential exists. By considering a limit process expansion of the form

$$\Phi = U_\infty \{x + \varepsilon_1(\delta)\varphi_1(x,y,z,t) + \varepsilon_2(\delta)\varphi_2(x,y,z,t) + \cdots\} \tag{3}$$

associated with the limit $\delta \to 0$, while keeping x, y, z, t, and M_∞ fixed, the classical first- and second-order aerodynamic theories are obtained. The orders of the terms can be determined from the boundary condition at the wing surface, and one can show that $\varepsilon_1 = \delta$ and $\varepsilon_1 = \delta^2$, and that φ_1 satisfies the classical equation of linearized unsteady aerodynamics:

$$(1-M_\infty^2)\frac{\partial^2 \varphi_1}{\partial x^2} + \frac{\partial^2 \varphi_1}{\partial y^2} + \frac{\partial^2 \varphi_1}{\partial z^2} - \frac{M_\infty}{a_\infty}\frac{\partial^2 \varphi_1}{\partial x \partial t} - \frac{1}{a_\infty^2}\frac{\partial^2 \varphi_1}{\partial t^2} = 0 \tag{4}$$

subject to the linearized boundary condition

$$\frac{\partial \varphi}{\partial z} = \frac{\partial f_a}{\partial t} + U_\infty \frac{\partial f_a}{\partial x} \equiv w_a(x,t) \quad \text{on } z=0, 0 \le x \le c \tag{5}$$

where

$$f_a \equiv z_a = z_c(x,y) - x\alpha(y,t) \tag{6}$$

represents the boundary of the so-called antisymmetric problem; that is, the skeleton of the wing with the thickness removed and the shape f_a determined by the camber and the instantaneous local angle of attack α. For subsonic flow, one can show that the lifting problem does not have a unique solution, because potential theory (Laplace's equation) admits an arbitrary circulation about the airfoil or wing. Uniqueness is restored by imposing the *Kutta–Joukowski condition* of zero pressure jump from the upper to the lower surface at the wing trailing edge (TE):

$$\Delta p_{TE} = 0 \tag{7}$$

This condition can be stated in various ways and physically means that the flow must leave the sharp trailing edge smoothly, with no singularities in the perturbation pressure or fluid velocity, as shown in Fig. 6.
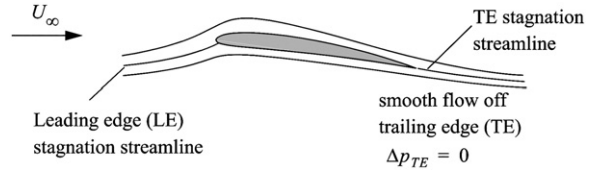
The second-order correction φ_2 satisfies a similar linear equation, but with nonhomogeneous terms that depend on the first-order solution φ_1; see, for example, Kevorkian and Cole [40]. In the steady case, the first-order solution yields the familiar Prandtl–Glauert similarity rules of linearized compressible flow. The mathematical basis for classical linear unsteady aerodynamics, including Theodorsen's theory, the Possio equation, the kernel function (integral equation) method, doublet and vortex lattice methods, etc., is based on the validity of the regular perturbation expansion, Eq. (3).

Near Mach one, the linearized solution of the unsteady aerodynamics problem breaks down, because the linear governing equation is incapable of modeling wave propagation correctly near sonic speeds. A nonphysical singularity at Mach 1 occurs, resulting in the well-known blowup of the aerodynamic lift and moment coefficients and giving rise to the myth of a "sonic wall". The superposition principle also breaks down, and no uniformly valid linearization of the aeroelastic problem is possible.

The classical linearization due to Landahl [34] is based on the observation that for sufficiently high reduced frequencies, such that

$$k \gg |1-M_L| \tag{8}$$

everywhere in the flow, where M_L is the local Mach number, the unsteady linear terms in the governing equation will dominate. The nonlinear transonic terms can then be neglected and the Mach number set equal to 1 to this level of approximation, resulting in the linear equation

$$\frac{\partial^2 \varphi_1}{\partial y^2} + \frac{\partial^2 \varphi_1}{\partial z^2} - \frac{1}{a_\infty}\frac{\partial^2 \varphi_1}{\partial x \partial t} - \frac{1}{a_\infty^2}\frac{\partial^2 \varphi_1}{\partial t^2} = 0 \tag{9}$$

From what has already been said, it should be clear that the linearization cannot be uniformly valid, even for high reduced frequencies satisfying Eq. (8). In most practical transonic flutter problems involving aircraft wings and control surfaces, this frequency condition is not satisfied, because local Mach numbers as high as 1.5 (and higher) occur, whereas the reduced frequency at which transonic flutter is encountered is typically of the order of $k \sim O(0.1)$.

3.3. Transonic small disturbance equation

As pointed out by Cole [30], for the description of many (but not all) features of steady transonic flow relevant to airplane aerodynamics, the assumption of an inviscid perfect gas subjected to small disturbances is adequate. From the viewpoint of numerical calculations, most of the essential difficulties are contained in these equations and the qualitative features are reproduced faithfully, at least for thin wings operating near cruise design conditions. Unsteady transonic flows were not considered by Cole in this context, neither were aeroelastic stability problems such as flutter and divergence. Experience over the past 30 years or so clearly shows that inviscid small disturbance theories have definite limitations in such applications. However, as a starting point for introducing the key concepts and features of transonic flows to the engineer who wants to take the next step from linear

aerodynamics, the transonic small disturbance theory is indispensable.

For example, the theory provides the simplest foundation for isolating the effects of thickness, angle of attack, and wing shape, which in the linear theory are second-order effects. It is again convenient to make use of asymptotic expansions based on certain limit processes, and to consider a family of "similar" wings of the same airfoil shape, Fig. 5, by scaling the wing profile through the thickness scaling parameter δ in Eq. (1). For small angles of attack and small elastic deformations, the equation for the wing surface can be approximated by

$$B(x,y,z,t) = z - \delta \left\{ f_{u,l}(x,y) + \frac{[w(y,t) - x\alpha(y,t)]}{\delta} \right\} = 0 \tag{10}$$

where it has been assumed that the y-axis is the elastic axis of the wing. Extensions to the general case where camber bending occurs is straightforward; see [41].

If a limit process expansion based on the limits $\delta \to 0$ and $M_\infty \to 1$ is carried out in the original physical coordinates of the wing, we will simply recover the classical linear potential equation. Cole has shown how suitable expansions for a class of steady transonic flow problems can be obtained using the method of strained coordinates [13]. The unsteady case has been considered by Bendiksen [41], allowing for coordinate straining on the time scale as well:

$$\tilde{y} = \lambda(\delta)y; \quad \tilde{z} = \lambda(\delta)z; \quad \tilde{t} = \tau(\delta)t \tag{11}$$

where $\tilde{y}, \tilde{z}$, and $\tilde{t}$ are fixed in the limit $\delta \to 0$. The coordinate straining accounts for the fact that the propagation of disturbances extends farther and farther in the transverse y and z directions than in the upstream direction, as $M_\infty \to 1$. To obtain an expansion valid in some neighborhood of Mach 1, we let $M_\infty \to 1$ at a certain rate,

$$M_\infty^2 = 1 - K\nu(\delta), \quad \nu(\delta) \to 0 \quad \text{as } M_\infty \to 1 \tag{12}$$

The constant K, which defines the rate at which $M_\infty \to 1$ as $\delta \to 0$, is the classical form of the so-called transonic similarity parameter and is held fixed in the limit $\delta \to 0$.

The expansion for the velocity potential is now assumed of the form

$$\Phi = U_\infty(x + \varepsilon(\delta)\varphi(x,\tilde{y},\tilde{z},\tilde{t};K) + \cdots) \tag{13}$$

The first-order perturbation potential φ in Eq. (13) involves both the first and second order perturbations in the classical regular expansion, Eq. (3), but not any third-order terms [40]. Since the entropy changes at shocks are of third order in the perturbation pressure, the same leading-order term would be obtained for the Euler equations. To determine the relationships between the scaling parameters, we consider the boundary condition of tangent flow at the wing surface, which can be written in the form

$$\frac{DB}{Dt} \equiv \frac{\partial B}{\partial t} + \mathbf{u} \cdot \nabla B = 0 \tag{14}$$

where $B(x,y,z,t) = 0$ defines the instantaneous locus of the fluid–structure boundary, Fig. 5 and Eq. (10). Using Eqs. (10) and (13), the leading-order terms of Eq. (14) become [41]

$$\varepsilon\lambda \frac{\partial \varphi}{\partial \tilde{z}} = \delta\left(\frac{\partial f}{\partial x} - \frac{\alpha}{\delta}\right) - \frac{\delta}{U_\infty}\left(\frac{\tau}{\delta}\frac{\partial w}{\partial \tilde{t}} - \frac{\tau}{\delta}\frac{\partial \alpha}{\partial \tilde{t}}x\right) + \cdots \tag{15}$$

To balance the terms in the quasistatic or steady limit, we need

$$\varepsilon\lambda = \delta, \quad \alpha/\delta \sim O(1) \tag{16}$$

The ordering between ε, ν, and λ must also be chosen such that the resulting equation for the perturbation potential φ can properly describe a transonic flow-field; that is, a flow with

both subsonic and supersonic regions, including shock waves. As we have already pointed out, this requires a nonlinear equation. The appropriate equation can be obtained by substituting Eq. (13) into the full potential equation, Eq. (29), and expanding term by term. The most general equation is obtained by balancing all terms of dominant orders, which in the steady case is the classical nonlinear von Kármán–Guderley equation

$$\left[K - (\gamma+1)\frac{\partial\varphi}{\partial x}\right]\frac{\partial^2\varphi}{\partial x^2} + \frac{\partial^2\varphi}{\partial\tilde{y}^2} + \frac{\partial^2\varphi}{\partial\tilde{z}^2} = 0 \tag{17}$$

and corresponds to a so-called *distinguished limit*, where a definite order between the scaling parameters is obtained:

$$\varepsilon = \nu = \delta^{2/3}; \quad \lambda = \delta^{1/3}; \quad K = \frac{1-M_\infty^2}{\delta^{2/3}} \tag{18}$$

In the unsteady case, the most general form is obtained by retaining certain time derivative terms that are, strictly speaking, of higher order (see the discussion in Ref. [41]):

$$\left[\chi - \frac{\partial\varphi}{\partial x} - \left(\frac{\gamma-1}{\gamma+1}\right)\frac{\tau}{U_\infty}\frac{\partial\varphi}{\partial\tilde{t}}\right]\frac{\partial^2\varphi}{\partial x^2} + \frac{\partial^2\varphi}{\partial\tilde{y}^2} + \frac{\partial^2\varphi}{\partial\tilde{z}^2} - \frac{2}{U_\infty}\frac{\partial^2\varphi}{\partial x\partial\tilde{t}} - \frac{\tau}{U_\infty^2}\frac{\partial^2\varphi}{\partial\tilde{t}^2} = 0 \tag{19}$$

which is based on the following ordering of ε, ν, λ, τ:

$$\varepsilon = \nu = \tau = \frac{\delta^{2/3}}{[(\gamma+1)M_\infty^2]^{1/3}}$$
$$\lambda = [(\gamma+1)M_\infty^2\delta]^{1/3} \tag{20}$$

where

$$\chi = \frac{1-M_\infty^2}{[(\gamma+1)M_\infty^2\delta]^{2/3}} \tag{21}$$

is a new transonic similarity parameters, replacing K. This is also the same parameter as obtained by Spreiter [5,6], by multiplying together different similarity parameters. Spreiter was guided by the observation that the new transonic similarity parameter χ gives a better fit to the experimental data when the Mach number differs from one. The classical von Kármán parameter K was obtained by arguing that in transonic flows, $M_\infty \cong 1$, and the Mach number may therefore be set equal to unity, to the order of approximation considered in the von Kármán–Guderley equation. In the asymptotic expansion procedure outlined by Bendiksen [41], on the other hand, this new similarity parameter χ arises naturally in the distinguished limit.

If one neglects the terms scaled by τ, the classical form of the Transonic Small Disturbance (TSD) equation is obtained[1]:

$$\left[\chi - \frac{\partial\varphi}{\partial x}\right]\frac{\partial^2\varphi}{\partial x^2} + \frac{\partial^2\varphi}{\partial\tilde{y}^2} + \frac{\partial^2\varphi}{\partial\tilde{z}^2} - \frac{2}{U_\infty}\frac{\partial^2\varphi}{\partial x\partial\tilde{t}} = 0 \tag{22}$$

The equivalent 2D version was the basis for the early transonic flutter codes, such as LTRAN2, for example. This equation can be shown to be valid only for relatively low reduced frequencies, and is associated with the quasisteady limit where $k \sim \varepsilon \to 0^+$. To obtain an equation that has a chance of modeling nonlinear transonic flow over an extended time period, without nonuniformities occurring on the time scale, the second derivative term with respect to time must be retained. Although it is formally a second-order term, it can have a first-order cumulative effect on the unsteady flow solution over a finite time interval, because without this term the wave propagation speed is incorrect.

---

[1] The exact form of this equation depends on the choice of the transonic similarity parameter K or χ.

Similarly, the time derivative in the coefficient of $\partial^2\varphi/\partial x^2$ should be retained. This is a higher-order term as well, but its cumulative effect on the solution may become of first order over long time intervals. First, we note that when the local Mach number is equal to unity, the coefficient of the $\partial^2\varphi/\partial x^2$ term in the steady equation vanishes. The unsteady term in question makes the coefficient nonzero and of order ε, and we obtain a singular perturbation problem. The presence of this term redefines the region where the equivalent quasistatic equation with "frozen coefficients" changes type, from locally elliptic (subsonic flow) to locally hyperbolic (supersonic flow); hence the term will affect the instantaneous location of the moving shocks. Second, this term as well as the $\partial\varphi/\partial x$ term becomes periodic if the wing executes harmonic motion at or near the flutter boundary. Even away from the flutter boundary, both terms represent parametric excitation, which could bring about instabilities in the flutter solution through nonlinear parametric resonances. Furthermore, because χ is small in regions where the local Mach number is close to one, the $\partial\varphi/\partial x$ and $\partial\varphi/\partial\tilde{t}$ terms – albeit small – will affect the instantaneous locus of $M=1$, where the flow either changes from subsonic to supersonic (sonic line), or from supersonic back to subsonic (shocks). Consequently, the terms could have a noticeable effect on the unsteady shock motion, which plays an important role in the flutter problem [42–44]. This author believes that it is the presence of these nonlinear parametric excitation terms in the leading order $\partial^2\varphi/\partial x^2$ coefficient of the governing equation that triggers the phenomenon of "delayed flutter", as will be discussed later. Mathematically, the original small-disturbance solution suffers from a nonuniformity on the time scale, which gradually causes the linearized solution to break down and to drift away from the actual nonlinear solution.

Fig. 7 shows the fundamental difference between the supersonic regions in transonic flows and linearized supersonic flow. In linear supersonic flow, Fig. 7(a), the characteristics (Mach waves) are straight lines with a constant slope, and only one set of characteristics is allowed on the upper or lower airfoil surface, in order to satisfy the radiation condition; i.e., disturbances must propagate away from the wing in the far field. In the transonic case, Fig. 7(b), both families of characteristics are present in the supersonic pocket(s), one set representing an expansion wave and the other a compression wave. Also note that the slope of the characteristic continually changes as one moves away from the airfoil surface. In the simplest case of the steady TSD equation (e.g., the von Kármán–Guderley equation (17), the local characteristic surfaces (Mach cones) are given by

$$\frac{(dx)^2}{((\gamma+1)(\partial\varphi/\partial x))-K} = (d\tilde{y})^2 + (d\tilde{z})^2 \tag{23}$$

in the stretched similarity coordinates. For the two-dimensional case shown in Fig. 7(b) and (c), the local slopes of the characteristics become

$$\frac{d\tilde{y}}{dx} = \pm \frac{1}{\sqrt{((\gamma+1)(\partial\varphi/\partial x))-K}} \tag{24}$$

corresponding to the two families of characteristics shown in the figures. The slopes are real as long as

$$(\gamma+1)\frac{\partial\varphi}{\partial x} - K > 0 \tag{25}$$

which corresponds to a locally supersonic flow. The sonic line corresponds to locally sonic flow,

$$(\gamma+1)\frac{\partial\varphi}{\partial x} = K \Rightarrow M = 1 \tag{26}$$

From Eq. (24) it follows that the characteristics become vertical at the sonic line. In the *unsteady* case, it follows from Eq. (19) that the sonic line corresponds to

$$\chi - \frac{\partial\varphi}{\partial x} - \left(\frac{\gamma-1}{\gamma+1}\right)\frac{\tau}{U_\infty}\frac{\partial\varphi}{\partial\tilde{t}} = 0 \tag{27}$$

and now depends on time (as do the characteristics). Thus, the local Mach angle at a given point in the supersonic pocket is constantly changing. Of course, if the supersonic pocket vanishes during a part of the oscillation cycle, so do the characteristics.

Transonic expansion procedures for nonplanar flows generally require the use of matched asymptotic expansions, involving an inner and an outer solution valid in different domains (e.g., close to the body and the far field, respectively), and then matched to each other in an intermediate "overlap" domain. Transonic slender body theory falls into this category; see Cole and Messiter [8]. Other practical problems of this type include the sonic limit $M_\infty \to 1$ from below, and perturbations of shock-free flows; see Cole [45].

A sonic flow ($M_\infty = 1$), Fig. 7(c), is somewhat special. In this case, the supersonic region extends to infinity, as do the sonic line and the trailing-edge shock. A limit Mach wave (characteristic) emerges, which is asymptotic to the sonic line at infinity and divides the flowfield into two regions: an upstream region that can influence the upstream flow, and a downstream region that cannot. That is, the flow field behind the limit Mach wave cannot influence the flow in front of the limit Mach wave, and is in this respect similar to a supersonic flow-field. As a consequence, the far field must change, from a dominant vortex (circulatory) term fixed by the lift on the wing, modified by nonlinear terms, to a more source-like far field without circulatory terms [30].

In view of these observations, it is not surprising that the perturbation of a sonic flow is nontrivial from a mathematical standpoint and leads to nonuniformities in the solutions. As long as $M_\infty < 1$, the far field is subsonic and the dominant term is a vortex term given by the lift. At Mach 1, this far field disappears and is replaced by a similarity form corresponding to $K=0$ (or $\chi=0$) [45]. If one tries to model the flow as a small perturbation about the perfectly sonic flow, a nonuniformity at
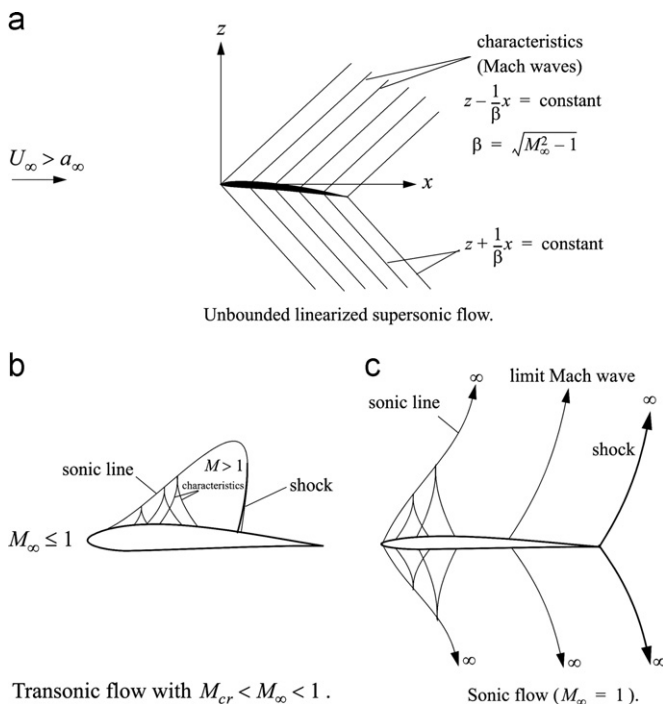
Fig. 7. Comparison of nature of supersonic regions in transonic flow with unbounded linearized supersonic flow (2D case).

infinity will appear. Near to the wing or body, on the other hand, the solution is valid and from it one can deduce the important *law of stabilization* or *Mach number freeze*,

$$\frac{dM}{dM_\infty}\bigg|_{M_\infty = 1} = 0 \tag{28}$$

which has interesting implications in aeroelastic problems.

3.4. Full potential equation

Within the usual framework of the dynamics of a perfect inviscid gas, a velocity potential exists to second order in a small parameter representative of the flow deflection. The exact equation for this potential is simply the continuity equation, which after some manipulations to eliminate the density ρ in favor of the speed of sound a (and making use of the unsteady Bernoulli equation) can be put in the form

$$a^2 \nabla^2 \Phi - \mathbf{u} \cdot \nabla(u^2/2) - \frac{\partial}{\partial t}(u^2) - \frac{\partial^2 \Phi}{\partial t^2} = 0 \tag{29}$$

where

$$\mathbf{u} = \nabla\Phi, \quad u^2 = \mathbf{u} \cdot \mathbf{u} = \nabla\Phi \cdot \nabla\Phi \tag{30}$$

The local speed of sound can be obtained from the unsteady Bernoulli equation:

$$a^2 = a_\infty^2 + \frac{\gamma-1}{2}\left[U_\infty^2 - u^2 - 2\frac{\partial\Phi}{\partial t}\right] \tag{31}$$

The local pressure is obtained from the isentropic relation in the form

$$p = p_\infty \left\{\frac{\rho}{\rho_\infty}\right\}^\gamma = p_\infty \left\{\frac{a^2}{a_\infty^2}\right\}^{\gamma/(\gamma-1)} = p_\infty \left[1 + \frac{\gamma-1}{2a_\infty^2}\left(U_\infty^2 - u^2 - 2\frac{\partial\Phi}{\partial t}\right)\right]^{\gamma/(\gamma-1)} \tag{32}$$

For computational work, the conservation-law (divergence) form of the equation is usually preferable,

$$\frac{\partial\rho}{\partial t} + \frac{\partial}{\partial x_j}\left(\rho\frac{\partial\Phi}{\partial x_j}\right) = 0 \tag{33}$$

and the isentropic relations (32) can then be used to express the density ρ in terms of the velocity potential and the undisturbed flow properties.

If one needs to go beyond linear potential methods because shock strengths and/or wing amplitudes exceed the small-disturbance limitations, the full potential equation does not buy much, at least not in the important transonic region. The reason is that the equation is exact only up through second order in the perturbation parameter. Entropy production at the shocks enters at the 3rd order; hence extension to higher than 2nd order is not possible in a potential flow model. Furthermore, because only "isentropic shocks" can be accommodated, the shocks are too strong and too far aft on the wing chord. Both errors can have a significant effect on flutter stability predictions.

Outside the transonic region, the nonlinear full potential equation may provide some insights into the effects of airfoil thickness, camber, etc., on the flutter boundaries, at a computational cost somewhat less than the Euler equations. It is also useful as a starting point for deriving aerodynamic and aeroelastic similarity rules.

3.5. Euler equations

In one neglects the viscous stresses, the stress tensor becomes diagonal ($\sigma_{ij} = -p\delta_{ij}$) and the momentum equations reduce to the Euler equations

$$\frac{D\mathbf{u}}{Dt} = \frac{1}{\rho}\nabla p + \mathbf{f} \tag{34}$$

where $\mathbf{u}$ is the fluid velocity with components u_i, ρ is the density, p is the pressure, and $\mathbf{f}$ is the body force per unit mass. The conservation laws for mass and energy yield two additional equations. The equation of state can be used to eliminate the pressure from the governing equations, which is often convenient in numerical computations.

For inviscid flows, the boundary condition on the fluid–structure boundary is the tangent flow condition

$$\frac{\partial B}{\partial t} + \mathbf{u} \cdot \nabla B = 0 \tag{35}$$

where $B(x,y,z,t) = 0$ is the equation for the moving fluid–structure boundary, Fig. 5. In aeroelastic applications, where the exact position and velocity of the structural boundary is not known á priori (explicitly) but must be calculated as part of the time-dependent aeroelastic solution, an accurate and consistent enforcement of the tangent flow condition is a formidable problem. In the far field, radiation conditions are imposed to allow only outward propagating waves. At the (sharp) trailing edge of wing, the Kutta–Joukowski condition of zero pressure jump must be imposed, if the edge is subsonic.

The Euler equations represent a good flow model for many transonic flutter calculations, provided viscous effects are not dominant and boundary layer separation does not occur. In practice, this means that the equations can be expected to give reasonable results for smooth flows representative of transonic wings operating at or near design conditions. Because entropy and vorticity production at shocks are captured in a time-accurate manner, the shock locations and nonlinear shock dynamics are modeled much better than in potential flow models, which can only admit nonphysical isentropic shocks.

It is appropriate to mention that both the Euler equations and the full potential equation can have nonunique steady solutions at transonic Mach numbers. Early evidence of nonunique solutions in transonic flow calculations was reported by Steinhoff and Jameson [46]. They found that certain airfoils would admit multiple steady solutions to the discretized two-dimensional full potential equation, for a narrow range of transonic Mach numbers and angles of attack. Later, Jameson found similar nonunique steady solutions to the two-dimensional Euler equations, for certain airfoils operating at transonic Mach numbers [47]. In these cases, the individual solutions would differ in the location(s) and/or the number of shocks on the airfoil surface, and the aerodynamic problem exhibited hysteresis as the solution could be made to jump from one branch to another by changing the angle of attack. An unsteady but not aeroelastic case was studied by Caughey [48]; see also the paper by Hafez [49].

Bendiksen [50] has shown that *if the airfoil is flexible and is allowed to move* as part of an aeroelastic system, the possible paths that can lead to bifurcations to nonunique solutions are much broader and less special. This is because most aeroelastic problems are non-selfadjoint, containing circulatory forces whose work done on the wing depends on the path taken, not just on the end-points. As a result, sudden bifurcations to nonunique or anomalous solutions can occur along the dynamical path of the system, without warning. When this happens, a unique flutter or divergence boundary may not exist, at least not in the classical

sense. Such bifurcations had been observed in earlier Euler-based flutter calculations by Kousen and Bendiksen [51,52].

3.6. Navier–Stokes equations

At the top of the hierarchy of unsteady flow models suitable for engineering applications, one finds the Navier–Stokes equations. From an engineering standpoint at the continuum level, the equations provide a physics-based model of steady and unsteady fluid flows, subject to certain assumptions. The assumptions, in addition to the continuum hypothesis, have to do with the physical nature of the stresses within a moving fluid, and the dependence of the stress tensor on the velocity gradients. The validity of these assumptions in any given flow problem must ultimately be settled by experiment.

From a historical perspective, the equations credited to Navier and Stokes are limited to the momentum equations for a viscous fluid,[2]

$$\frac{D\mathbf{u}}{Dt} = \frac{1}{\rho}\nabla\cdot[\sigma] + \mathbf{f} \tag{36}$$

where $[\sigma]$ is the Cartesian stress tensor. The stresses are related to the velocity gradients through a constitutive law known as Stokes's hypothesis:

$$\sigma_{ij} = -p\delta_{ij} + 2\mu\left(e_{ij} - \frac{1}{3}\Delta\delta_{ij}\right) \tag{37}$$

where μ is the viscosity and

$$e_{ij} = \frac{1}{2}(u_{i,j} + u_{j,i}); \; \Delta = e_{kk} \tag{38}$$

are the strain rates and the volumetric expansion rate, respectively. In a modern CFD conservation-law form, the conservation of mass and energy are typically included and the Navier–Stokes equations written as

$$\frac{\partial\mathbf{W}}{\partial t} + \frac{\partial\mathbf{F}_j}{\partial x_j} = 0 \tag{39}$$

where

$$\mathbf{W} = \begin{bmatrix} \rho \\ \rho u_1 \\ \rho u_2 \\ \rho u_3 \\ \rho e \end{bmatrix} \quad \mathbf{F}_j = \begin{bmatrix} \rho u_j \\ \rho u_1 u_j - \sigma_{1j} \\ \rho u_2 u_j - \sigma_{2j} \\ \rho u_3 u_j - \sigma_{3j} \\ \rho e u_j - \sigma_{ij}u_i + q_j \end{bmatrix} \tag{40}$$

$$q_j = -k\frac{\partial T}{\partial x_j} = -\frac{\gamma}{\gamma-1}\frac{\mu}{Pr}\frac{\partial}{\partial x_j}\left(\frac{p}{\rho}\right) \tag{41}$$

$$Pr = \frac{c_p\mu}{k} \tag{42}$$

Here, q_j are the components of the heat flux vector, k is the coefficient of heat conductivity, T is the absolute temperature, c_p is the specific heat at constant pressure, and Pr is the Prandtl number. The variation of the coefficient of viscosity μ is usually calculated using Sutherland's law. The equation of state for a perfect gas can be used to express the pressure in terms of the density and the intrinsic internal energy e (total minus kinetic),

---

[2] According to Prandtl and Titjens [53], the equations were first obtained by Navier (1827) and Poisson (1831), based on certain assumptions regarding intermolecular forces. Saint Venant (1843) and Stokes (1845) later found the same equations making assumptions on the continuum level, assuming that the fluid stresses are linear functions of the deformation velocities (Newton's law of viscosity) and that the mean normal stress is independent of the velocity of dilatation. One can only wonder why only the first and the last researcher got their names on the equations, etc.

as follows:

$$p = \rho(\gamma-1)\left(e - \frac{1}{2}u_iu_i\right) \tag{43}$$

The equations must be supplemented by appropriate initial and boundary conditions on the fluid velocity field u_i and the heat flux components q_j. At a solid (fluid–structure) boundary, the no-slip condition $u_i = 0$ is applied. Adiabatic wall conditions are usually assumed in aerodynamic and aeroelastic calculations, although several other conditions can obviously be applied as well.

From a theoretical standpoint, however, there is no assurance that the resulting initial-boundary value problem will be well-posed, in the sense of Hadamard. By well-posed we mean that the solution exists and is unique and depends in a continuous manner on the initial and boundary data; see, for example, the discussion in Courant and Hilbert, vol. II [54]. Although the incompressible 2D Navier–Stokes equations can be shown to have "well-behaved" solutions that remain "smooth" for all time, no such proof is known for the 3D equations, even in incompressible flow. All that can be proven is that smooth solutions to the 3D equations exist for a short time and depend continuously on the initial-boundary data; after that time singularities and blow-ups (infinities) may occur in the vorticity amplitudes and/or the kinetic energy of the fluid. The possible implications of all of this on the verification and validations of unsteady Navier–Stokes codes in aeroelastic applications remain largely unknown.

The challenge associated with solving the Navier–Stokes equations in practical aeroelastic problems can be described in many ways, e.g., as the "curse of dimensionality" or the "curse of length scales", etc., but from the viewpoint of the engineer the best explanation is simply *the abundance of excess dynamics*. Flows over full-scale transport and fighter aircraft wings are turbulent over most of the chord, because the Reynolds numbers (*Re*) at typical operating conditions are quite high (10^7–10^8). Turbulent flows contain eddies or vortices of varying length scales, and the range of length scales that must be resolved in an accurate direct numerical simulation increases dramatically with increasing Reynolds numbers. Using arguments based on dimensional analysis, Jameson [26] estimates that the "computational complexity" associated with the full simulation of turbulent three-dimensional flows down to the smallest length and time scales would scale proportional to the cube of the Reynolds number. Even with revolutionary developments in computational algorithms and computer hardware, direct numerical simulations based on the full Navier–Stokes equations will not likely become practical for realistic flutter calculations over the next decade at least, perhaps much longer. This leaves us with the Reynolds averaged or Favre averaged equations and appropriate turbulence models. Presently, thin layer Navier–Stokes codes are typically used in computational aeroelasticity. For recent surveys of some of the challenges in using these codes in applications involving novel fluid–structure interactions, see Bartels [55] and Schuster [56]. Although Large Eddy Simulation (LES) together with hybrid methods (LES/RANS) have by now become well established in many engineering applications [57], they have not as yet become widely used tools in practical aeroelastic calculations.

3.7. Computational considerations

Unsteady transonic flow calculations are much more difficult than subsonic or supersonic flow calculations, for several reasons. First, the governing partial differential equations are nonlinear and moving shocks must be modeled correctly. Second, the flow-field is of a mixed type, with embedded supersonic regions if the free-stream Mach number is less than one (subsonic far field), and embedded subsonic regions if the free-stream Mach number is

greater than one (supersonic far field). Third, the extent of the embedded supersonic or subsonic regions are *time-varying*, as are the moving shocks, and must be determined in a time-accurate manner as part of the solution. In some cases, the embedded supersonic region shrinks down to zero and vanishes together with the shock over part of the flutter cycle.

From a computational standpoint, we may define the transonic region for a given flow problem by the inequality $M_{cr} \leq M_\infty \leq M_{cr}^{sup}$. Here, M_{cr} is the critical Mach number as usually defined; that is, the lowest value of the free-stream Mach number M_∞ at which the flow first becomes sonic at some point in the flowfield. In steady potential flow, the maximum principle can be used to show that this point must occur on the solid boundary, e.g., somewhere on the wing surface. Note that even in the steady case, M_{cr} depends on the thickness and shape as well as on the angle of attack and elastic deformation of the wing. In the unsteady or flutter case, the critical Mach number also depends on the flutter amplitudes and on the flutter mode shape.

The supersonic critical Mach number M_{cr}^{sup} is defined in a similar manner, but its determination is more elusive and *a priori* estimates of its value in any given example are more difficult. It is the highest free-stream Mach number at which the *lowest* Mach number in the flowfield reaches one from above. Thus, embedded subsonic regions in an otherwise supersonic flow are only possible for Mach numbers in the range $1 < M_\infty < M_{cr}^{sup}$. For thin planar wings characteristic of supersonic aircraft, the supersonic critical Mach number M_{cr}^{sup} in *steady* flow may be very close to one. In unsteady flows, however, M_{cr}^{sup} may be as high as 1.2, even for thin wings. In the nonlinear Euler-based transonic flutter calculations for a flat panel by Davis and Bendiksen [58], for example, embedded subsonic regions were observed next to the panel surface at Mach numbers in the 1–1.2 region. The embedded subsonic pockets would grow and shrink periodically in response to the panel flutter mode, typically vanishing over part of the flutter cycle. Experimental results obtained by Bryson [59] for a two-dimensional wedge section with a leading-edge half-angle of $10°$ show an embedded subsonic region between the leading edge shock and the sonic line for Mach numbers as high as 1.32.

In the case of thin planar wings for which the transonic small disturbance theory holds, the transonic region for the steady problem is often defined in terms of the transonic similarity parameter as the Mach number region for which the similarity parameter falls in the range (Liepmann and Roshko [60])

$$-1 \leq \frac{M_\infty^2 - 1}{[(\gamma + 1)M_\infty^2 \delta]^{2/3}} \leq 1 \tag{44}$$

In practical *unsteady* aerodynamics and flutter problems involving aircraft wings, however, the transonic region is considerably broader and extends to absolute values of the transonic similarity parameter well beyond unity.

In a modern computational fluid dynamics (CFD) approach, the aerodynamic model is typically expressed in a weak or integral form of the conservation laws,

$$\frac{\partial}{\partial t} \int_\Omega \mathbf{W} \, dV + \int_{\partial\Omega} \mathbf{F} \cdot \mathbf{n} \, dS = 0 \tag{45}$$

where Ω is an element volume with boundary $\partial\Omega$ moving with velocity $\mathbf{U}$, $\mathbf{n} = n_i \mathbf{e}_i$ is the outward unit normal to $\partial\Omega$, $\mathbf{e}_i$ are the unit vectors in the x_i directions, and

$$\mathbf{W} = \begin{bmatrix} \rho \\ \rho u_1 \\ \rho u_2 \\ \rho u_3 \\ \rho e \end{bmatrix} \quad \mathbf{F}_j = \begin{bmatrix} \rho(u_j - U_j) \\ \rho u_1(u_j - U_j) - \sigma_{1j} \\ \rho u_2(u_j - U_j) - \sigma_{2j} \\ \rho u_3(u_j - U_j) - \sigma_{3j} \\ \rho e(u_j - U_j) - \sigma_{ij}u_i + q_j \end{bmatrix} \tag{46}$$

Here, e is the total energy per unit mass, u_j and U_j are the Cartesian components of $\mathbf{u}$ and $\mathbf{U}$, respectively, σ_{ij} are the components of the Cartesian stress tensor, and $\mathbf{F} = \mathbf{F}_j \mathbf{e}_j$.

It is not the purpose of this review to evaluate the various discretization and integration methods that have been developed for the Euler and Navier–Stokes equations, except to say that both finite volume and finite element methods exist for both structured and unstructured meshes; see Refs. [61–65]. In the author's opinion, the finite element method offers a systematic spatial discretization for arbitrary unstructured meshes, and has the additional advantage that it is readily understood by the flutter engineer or aeroelastician who nowadays routinely uses finite elements to solve structural dynamics problems associated with aircraft.

In the inviscid (Euler) flow model, $\sigma_{ij} = -p\delta_{ij}$, and the equation of state can be used to eliminate the pressure p. In a Galerkin finite element discretization of the Euler equations, the vector $\mathbf{W}$ of unknown is approximated as

$$\mathbf{W}(x_1, x_2, x_3, t) = \sum_j \mathbf{W}_j(t)\varphi_j(x_1, x_2, x_3, t) \tag{47}$$

where $\mathbf{W}_j$ are the nodal values of $\mathbf{W}$ and φ_j are shape (interpolation) functions. Tetrahedral elements are often used with linear interpolation functions. The finite element discretization is carried out by substituting Eq. (47) into the Galerkin form of Eq. (45) and applying the divergence theorem. The integrals are evaluated numerically, using Gaussian integration. The space-discretized nodal equations for the fluid domain then become [29]

$$\frac{d}{dt} \sum_j \mathbf{m}_{ij} \mathbf{W}_j + \mathbf{Q}_i - \mathbf{D}_i = 0 \tag{48}$$

where $i = 1, 2, ..., N$ (all nodes), and the summation on j extends over all nodes in the "superelement" or control volume associated with node i, i.e., the union of all elements that meet at node i. Here, $\mathbf{m}_{ij}$ is the consistent mass matrix, $\mathbf{Q}_i$ is the flux vector, and $\mathbf{D}_i$ is a vector of dissipative fluxes of a suitable type, to capture shocks and stabilize the scheme. For example, the Jameson–Mavriplis type dissipation operators [66,67], as modified in Refs. [68,69], have been found to be very well suited for aeroelastic calculations.

A finite element discretization of the structural domain leads to a similar set of equations, in term of suitable generalized Lagrangian displacement coordinates $\mathbf{q}_j$:

$$\frac{d}{dt} \sum_j \mathbf{m}_{ij} \dot{\mathbf{q}}_j + \mathbf{Q}_i^E + \mathbf{Q}_i^D - \mathbf{Q}_i^F = 0 \tag{49}$$

where the sum (assembly) must be carried out over all elements that meet at node i. Here, $\mathbf{Q}_i^E$ are the elastic forces, $\mathbf{Q}_i^D$ are the structural damping forces, and $\mathbf{Q}_i^F$ are the consistent generalized fluid forces associated with the ith node.

The formal mathematical similarity between the nodal (or element) equations for the fluid and structural domains, Eqs. (48) and (49), were exploited in Ref. [63] to formulate a new approach to computational aeroelasticity and fluid–structure interaction problems in general. This approach has been further developed in a number of papers [58,64,29,70,71] and has been shown to lead to a consistent and accurate modeling of a wide class of aeroelastic problems. For a recent review of alternate and more classical approaches, see [33].

4. Similarity laws for transonic flow

Similarity laws (sometimes referred to as similarity rules) are useful in explaining the effect of thickness and angle of attack, for example, on the stability boundaries of wings of a given airfoil type. In particular, through the use of similarity laws the number

of nondimensional parameters that must be considered (as obtained from dimensional analysis) can often be reduced to a much smaller number of *similarity parameters* for the problem. It is then possible to plot data for different airfoil thicknesses, etc., on a single curve.

4.1. Inviscid flow

The classical aerodynamic similarity laws for steady inviscid transonic flow were derived by von Kármán [1], Cole [2,4], Cole and Messiter [8], Guderley and Yoshihara [3], Spreiter [5,6], etc. More recently, Bendiksen showed how similarity laws for unsteady transonic flow could be derived for the quasi-steady limit $k \to 0^+$ [41]. These laws were then used to establish similarity parameters and similarity rules for transonic flutter and divergence. However, it was noted that the quasisteady rules did not fix the time scale or reduced frequency in an unambiguous way.

The effects of Mach number on subsonic flutter boundaries are typically not substantial, until the transonic region is entered. Theodorsen and Garrick [72] proposed a semi-empirical formula in which the flutter and divergence speeds scale proportional to $(1 - M_\infty^2)^{1/4}$. Calculations by Garrick [73] based on Possion's linear subsonic theory indicated that this rule is a reasonable approximation for wings of high mass ratios and low values of ω_h/ω_α, in the quasistatic limit $k \to 0$. For wings of low mass ratios, the compressibility corrections were found to be of the order of a few percent. However, since the rule is based on linearized subsonic aerodynamics, it is not applicable in the transonic region. For transport aircraft wings, this means that the rule is not valid beyond Mach numbers of about 0.7–0.75.

The similarity parameters for unsteady transonic flow are clear from the asymptotic expansion results in Section 3.3, Eqs. (11), (20), and (21):

$$\chi = \frac{1 - M_\infty^2}{[(\gamma + 1)M_\infty^2\delta]^{2/3}}; \quad \tilde{A} = [(\gamma + 1)M_\infty^2\delta]^{1/3}A$$

$$\tilde{\alpha} = \alpha/\delta, \quad \tilde{w} = w/\delta; \quad \tilde{t} = \frac{\delta^{2/3}t}{[(\gamma + 1)M_\infty^2]^{1/3}} \tag{50}$$

where γ is the ratio of specific heats and A is the aspect ratio of the wing. The similarity rules for the aerodynamic coefficients can then be stated in the form

$$C_p = \frac{\delta^{2/3}}{[(\gamma + 1)M_\infty^2]^{1/3}} \tilde{C}_p(\chi, \tilde{A}, \tilde{\alpha}, x/c, y/l) \tag{51}$$

$$C_L = \frac{\delta^{2/3}}{[(\gamma + 1)M_\infty^2]^{1/3}} \tilde{C}_L(\chi, \tilde{A}, \tilde{\alpha}) \tag{52}$$

$$C_M = \frac{\delta^{2/3}}{[(\gamma + 1)M_\infty^2]^{1/3}} \tilde{C}_M(\chi, \tilde{A}, \tilde{\alpha}) \tag{53}$$

$$C_D = \frac{\delta^{5/3}}{[(\gamma + 1)M_\infty^2]^{1/3}} \tilde{C}_D(\chi, \tilde{A}, \tilde{\alpha}) \tag{54}$$

where the functions $\tilde{C}_p, \tilde{C}_L, \tilde{C}_M$, and $\tilde{C}_D$ are "similarity functions" for the pressure coefficient, lift coefficient, etc., and are functions of the three similarity parameters χ, $\tilde{A}$, and $\tilde{\alpha}$ in the problem. The appearance of the ratio of specific heats γ in these relations allows comparisons of similar flows around wings tested using different gases, e.g., Freon (or other heavy gases) as compared to air.

Similarity here means that there is a certain correspondence between the local features of the flow between any two cases with the same values for the similarity parameters. For example, similar flows would have the same pressure distributions, lift, moment, drag, etc., after they have been scaled as specified by the similarity rules. Also, the location and strength of the shock(s) would have the same correspondence. Note that these rules differ fundamentally from the Prandtl–Glauert rule for linear flows, in that we cannot have similarity between flows at different Mach numbers for the *same* airfoil or wing. We can only set up this correspondence between different airfoils or wings with different thickness ratios, aspect ratios, and Mach numbers. The similarity parameters in Eq. (50) indicate that in order to have similar flows as the Mach number approaches one from below, the airfoil thickness and the angle of attack must be reduced and the aspect ratio must be increased.

Fig. 8 shows the result of applying the steady aerodynamic similarity rules, Eqs. (50)–(54), to steady transonic flows about the NACA 00xx family of airfoils at zero angle of attack, using the fully nonlinear Euler equations. Fig. 8(a) shows the pressure coefficient C_p vs. chord position on the upper surface of the NACA 0012 airfoil at $M = 0.85$, and the NACA 0006 airfoil at $M = 0.9006$. These cases correspond to the same value of the transonic similarity parameter,

$$\chi = \frac{1 - M_\infty^2}{[(\gamma + 1)M_\infty^2\delta]^{2/3}} = 0.7903 \tag{55}$$

assuming $\gamma = 1.4$. Fig. 8(b) shows the same pressure coefficients after applying the similarity rule given by Eq. (51). The agreement is surprisingly good, especially in the region upstream of the shock, where the flow is isentropic and irrotational. Also, the position of the shock agrees in the two calculations, to within
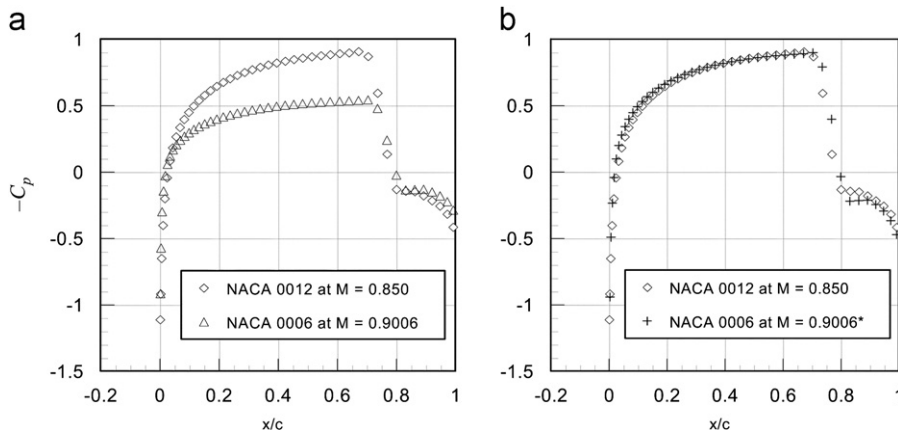

Fig. 8. (a) Comparison of pressure coefficients on upper surfaces of NACA 0012 and NACA 0006 airfoils in steady transonic flow at $M = 0.85$ and 0.9006, respectively, corresponding to the same value of similarity parameter ($\chi = 0.7903$) and (b) ∗ after applying transonic similarity rule, Eq. (51).

one grid point on the mesh used (144×24 C-mesh). Downstream of the shock, where the flow is no longer irrotational, a slight difference is noted. The similarity rule adjustment gives a slightly stronger shock, and hence a slightly higher pressure in the region behind the shock, as would be expected of a rule based on potential flow.

The relatively good agreement can be understood by recalling that, to second order in the perturbation parameter δ, the corresponding transonic flows calculated using the Euler equations satisfy similarity rules whose dominant terms are given by Eqs. (51)–(54). Entropy production at shocks is of 3rd order and thus would not affect the similarity laws to this order.

For aeroelastic similarity, it was shown in [74] that the transonic flutter similarity parameter

$$\psi = \frac{\overline{U}^2}{\pi\mu[(\gamma+1)M_\infty^2\delta]^{1/3}} = \frac{\hat{q}}{[(\gamma+1)M_\infty^2\delta]^{1/3}} \tag{56}$$

must also be kept fixed, where $\hat{q}$ is a nondimensional dynamic pressure:

$$\hat{q} = \frac{1}{2}\rho_\infty U_\infty^2 / \frac{1}{2}m\omega_\alpha^2 = \frac{1}{\pi}\left(\frac{U_\infty}{b\omega_\alpha\sqrt{\mu}}\right)^2 \tag{57}$$

To keep the reduced frequency $k=\omega b/U_\infty$ fixed, the reduced airspeed $\overline{U}=U_\infty/b\omega_\alpha$ must be held constant. In the inviscid case, there are three primary similarity parameters: χ, ψ, and $\overline{U}$. In viscous flows, the Reynolds number and the Prandtl number provide a fourth and fifth similarity parameter. In addition, we must include the dynamical similarity parameters for the wing itself, which in the simplest case of a typical section model consist of the four parameters a, x_α, r_α, and ω_h/ω_α. Finally, consideration must also be given to the amplitude scaling, as reflected through the similarity parameters $\tilde{\alpha}$ and $\tilde{w}$.

4.2. Viscous flow

The presence of a boundary layer will, of course, change the "effective" thickness ratio of the wing and therefore the magnitudes of the transonic coordinate stretching in the asymptotic expansion procedure discussed in Section 3.3. In fact the limit process expansion based on the limits $\delta\rightarrow0$ and $M_\infty\rightarrow1$, while keeping χ and $x,\tilde{y},\tilde{z}$ fixed, must be reinterpreted. Physically, the limit $\delta\rightarrow0$ should leave us with a flat or slightly cambered plate (the wing) of zero material thickness, but with a nonzero effective thickness equal to the displacement thickness δ^* of the boundary layer. This is essentially the same argument as advanced by Liepmann and Roshko [60] in estimating the effect of the boundary layer on the external transonic flow-field. Assuming a laminar boundary layer and denoting the length of the plate by l (or the first l units of a semi-infinite plate), they approximated the effective thickness ratio due to the boundary layer for Mach numbers near one as

$$\frac{\delta^*}{l} \cong 1.7208\sqrt{\frac{\nu}{lU}} \approx \frac{1}{\sqrt{Re}} \tag{58}$$

where we have followed Liepmann and Roshko and replaced the factor 1.7208 by unity for simplicity in the final relations. Replacing δ by δ^*/l in Eqs. (50) and (51) yields the following approximate similarity parameter and similarity law for the boundary layer effect

$$\chi^* = \frac{(1-M_\infty^2)Re^{1/3}}{[(\gamma+1)M_\infty^2]^{2/3}} \tag{59}$$

$$C_p = \frac{1}{[(\gamma+1)M_\infty^2Re]^{1/3}}\tilde{C}_p(\chi^*,\tilde{A}^*,\tilde{\alpha}^*,x/c,y/l) \tag{60}$$

where superscripts ($*$) indicate that the corresponding similarity parameter is based on δ^*/l.

In applying the transonic similarity laws, the boundary layer displacement thickness should be added to the physical thickness of the wing. Most (but not all) airfoils have a location of maximum thickness in the range $0.3c$–$0.4c$, and the boundary layer displacement thickness should be evaluated at that point. For example, for the NACA 64A010 airfoil, $t_{max}/c = 0.10$ at $x=0.4c$, one would make the following substitution in the formulas:

$$\delta\rightarrow\delta+2\delta^*/c = 0.10+\frac{2(0.4)(1.7208)}{\sqrt{0.4Re}} = 0.10+\frac{2.177}{\sqrt{Re}} \tag{61}$$

where Re is the Reynolds number based on airfoil chord and we have reinstated the numerical factor 1.7208 in the displacement thickness formula, Eq. (58). For example, if $Re=10^7$, the effective thickness ratio becomes $0.10+0.0007=0.1007$, which is a negligible increase. For $Re=10^6$, the effective thickness becomes 0.1022. Of course, most full-scale aircraft wings will not have laminar flow at 30% or 40% chord, hence the effective thickness estimates should be based on a turbulent boundary layer. Assuming transition at or close to the nose of the airfoil, the effective thickness ratio now becomes

$$\delta_e = \delta+\frac{2(0.4)(0.046)}{\sqrt[5]{0.4Re}} = \delta+\frac{0.0442}{\sqrt[5]{Re}} \tag{62}$$

for maximum thickness at $0.4c$. For $Re=10^7$, we now obtain $\delta_e=0.1018$. For $Re=10^6$, $\delta_e=0.1028$. Thus, the effect of the boundary layer displacement thickness on the transonic similarity laws is seen to be small, except for a flat plate or a wing of a very small thickness. If the thickness is reduced to 3%, for example, the effective thicknesses in the last example become $\delta_e=0.0318$ and 0.0328, respectively, and do result in observable shifts in the transonic flutter boundaries. In the case of a flat plate of zero thickness, we recover Eqs. (59) and (60).

A different approach to incorporating the effect of viscosity into the transonic similarity rules is to apply the same type of limit process expansion procedure to the Navier–Stokes equations as used to derive the inviscid TSD equation. This leads to the so-called viscous transonic (small disturbance) equation, wherein heat conduction and longitudinal viscosity are taken into account. Cole appears to have been first to derive an equation of this type in discussing the flow through a shock wave [2]. Sichel later used this approach to study various transonic problems within the framework of small disturbances [75,76], and obtained a new viscous transonic similarity parameter for two-dimensional steady transonic flow. Since the flow is still irrotational to the TSD order of approximation, the viscous TSD equation simply adds a term to the corresponding inviscid equation,

$$\chi_v\frac{\partial^3\varphi}{\partial x^3} + \left(\chi-\frac{\partial\varphi}{\partial x}\right)\frac{\partial^2\varphi}{\partial x^2} + \frac{\partial^2\varphi}{\partial\tilde{y}^2} = 0 \tag{63}$$

where χ_v is a viscous similarity parameter given by

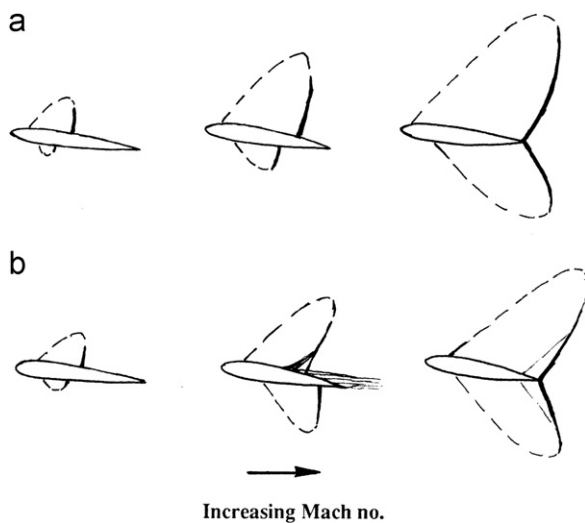$$\chi_v = \frac{1}{Re_l[(\gamma+1)M_\infty^2\delta]^{2/3}}\left(1+\frac{\gamma-1}{Pr_l}\right) \tag{64}$$

and Re_l and Pr_l are the longitudinal Reynolds number and Prandtl number, respectively, based on the longitudinal (compressive) viscosity μ_l. Sichel has made extensive use of similarity solutions of Eq. (63) in the study of viscous transonic flows over a wavy wall and the influence of Reynolds number and Mach number on the supersonic pockets and shocks. Applications of the viscous TSD similarity principles in practical aircraft applications have not yet (to this author's knowledge) appeared in the published literature. Note that the inclusion of viscosity simply adds a similarity parameter χ_v, without affecting the transonic similarity parameter χ.

The effects of shock-boundary layer interactions are not included in these corrections. In the presence of viscosity, the motion of the shocks for moderately to high angles of attack is changed significantly. Wind tunnel observations reveal that, for small positive angles of attack at Mach numbers slightly above M_{cr}, the aft motion of the upper shock with increases in angle of attack α is similar to what occurs in inviscid flow. But when the shock strength becomes sufficient to separate the boundary layer, the upper shock reverses direction and moves *forward* with further increases in α or Mach number. The lower shock, which is often not sufficiently strong to cause separation, continues its aft movement until it is *aft* of the upper shock—a situation that would not occur in inviscid flow over the same airfoil at positive angles of attack. This "shock-reversal" phenomenon is shown in Figs. 9 and 10. The effect of shock-boundary layer interactions should therefore be greatest in the post-dip region. With further increases in Mach number, the shocks eventually reach the trailing edge, as in the inviscid case.

If trailing-edge separation occurs, the steep rise of the flutter boundary in the post-dip region may not occur. Finally, additional "nonclassical" types of flutter may be triggered by viscous effects. These include stall flutter and buzz-type instabilities (aileron buzz). Interactions between the shock and the boundary layer can also lead to buzz-like shock oscillations on the airfoil surface, even in the absence of airfoil or wing motion, as observed in the calculations of Edwards [77] and more recently by Raveh and Dowell [78].

The presence of the boundary layer increases the effective thickness of the wing, which according to transonic similarity principles should shift the flutter boundary and the transonic dip to a slightly lower Mach number. Shock-boundary layer interactions, on the other hand, slow down the rearward movement of the steady shocks with increasing Mach number and angle of attack, and this should have the opposite effect and shift the dip towards higher Mach numbers. For thin wings, the net result should still be a small shift towards lower Mach numbers, but for moderately thick wings that may experience partial separation before the bottom of the transonic dip, the shift could be in either direction.

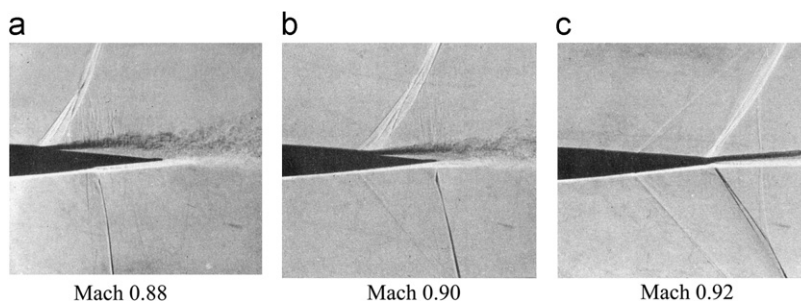### 4.3. Shock-foot singularity

In the inviscid case, the shock foot must be normal to the surface in order to satisfy the inviscid boundary condition of tangent flow. However, since the corresponding boundary value problem changes from hyperbolic in front of the shock to elliptic behind the shock, a singularity in the solution must be expected. An analysis of this singularity for the 2D airfoil case was first carried out by Gad [79] and Oswatitsch and Zierep [80], and later verified in a more rigorous manner by Cole and Cook [15]. The singularity is logarithmic, and downstream of the shock

$$C_p \sim \kappa^2 (x - x_s) \ln (x - x_s) \qquad (65)$$

resulting in an infinite curvature of the shock foot and an infinite acceleration of the flow immediately behind the shock foot on a convex airfoil surface. Here, x_s is the chordwise location of the shock and κ^2 is a constant that depends on the shock strength and the local surface curvature [15]. In a real (viscous) flow, shock-boundary layer interaction tends to smear out and weaken the singularity; however, early experiments by Ackeret et al. [10] do show a rapid expansion behind the shock. The singularity also has an indirect effect on boundary layer separation, in that it weakens the shock strength near the airfoil surface. Consequently, a stronger shock can be tolerated before boundary layer separation occurs.

In a more recent note by Zierep [82], he concludes that the nature of the singularity depends on the governing equations. If the Euler equations are used, for example, the problem becomes overdetermined (ill-posed) and the required boundary condition of tangent flow immediately behind the shock cannot be satisfied, and he concludes that "inviscid separation" must therefore occur. In the TSD result, Eq. (65), this problem does not arise and the tangent flow boundary condition can be satisfied behind the shock. Zierep reconciles these differences by pointing out that the TSD equation is not valid near a strong shock.

Fig. 11 shows a sketch of the viscous flow region at the foot of the shock, adapted from Ramm [17]. Because of interactions with the boundary layer, the shock foot in no longer normal to the airfoil surface and a lambda-shock typically develops, consisting of a series of oblique shocks and a final relatively weak

Fig. 9. Qualitative sketch of the behavior of shocks with increasing Mach number in (a) inviscid flow and (b) viscous flow, illustrating the phenomenon of "shock reversal" in viscous flow.

Fig. 10. Rearward motion of upper surface shock with increasing Mach number (RAE 102 airfoil, $\alpha = 2°$, $t/c = 0.10$). Adapted from Pearcy [81].

normal shock. The sonic line penetrates the boundary layer and eventually becomes essentially parallel to the local airfoil surface.
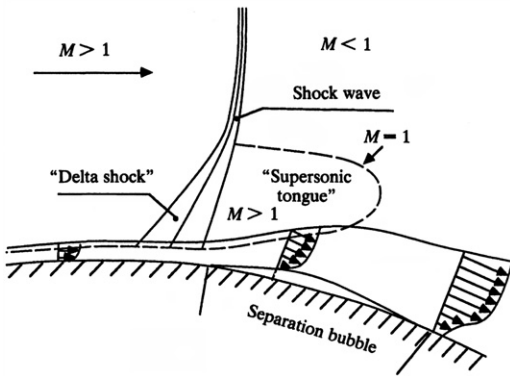

Fig. 11. Shock-boundary layer interaction [17].

5. Theory vs. experiment

5.1. Single-degree-of-freedom pitching oscillations

Fig. 12 shows representative comparisons of unsteady Euler calculations with experimental data for an NACA 0012 airfoil oscillating in pitch. The calculations are based on the Galerkin finite element method outlined in Section 3.7; see also Davis [83] and Davis and Bendiksen [68]. The experimental data is taken from the AGARD CT1 data set, based on wind tunnel tests performed by Landon [84]. The overall agreement between experiment and calculation is very good, despite the fact that the dynamic angle of attack varies over a considerable range, from close to zero to more than 5°. Note the presence of an intermittent shock near the leading edge in Fig. 12(b). This case is near the lower edge of the transonic range and is a reminder that, even thought the steady flow about the NACA 0012 airfoil at Mach 0.6 and $\alpha_m = 2.89°$ is subcritical, the superimposed pitching oscillation triggers the formation of an intermittent
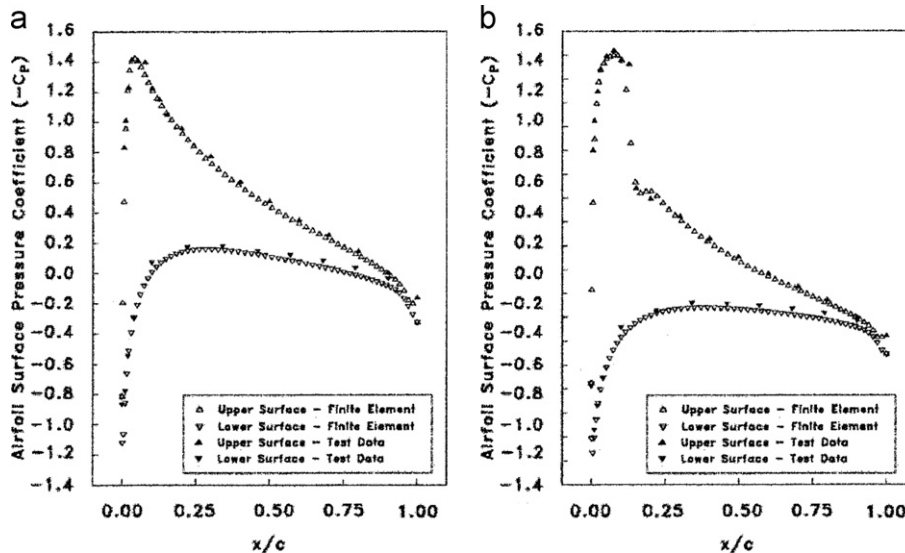

Fig. 12. Comparison of finite element Euler calculations [83] with experimental data for an NACA 0012 airfoil pitching about a quarter chord axis: (a) at $\alpha = 3.84°$ on up-stroke (α increasing); (b) at $\alpha = 4.82°$ on down-stroke (α decreasing). (AGARD CT1 test case [84]: $M_\infty = 0.6$; $k = 0.0808$; $Re = 4.8 \times 10^6$; mean angle of attack $\alpha_m = 2.89°$; pitching amplitude $\alpha_0 = 2.41°$). Note Tijdeman Type B shock near leading edge.
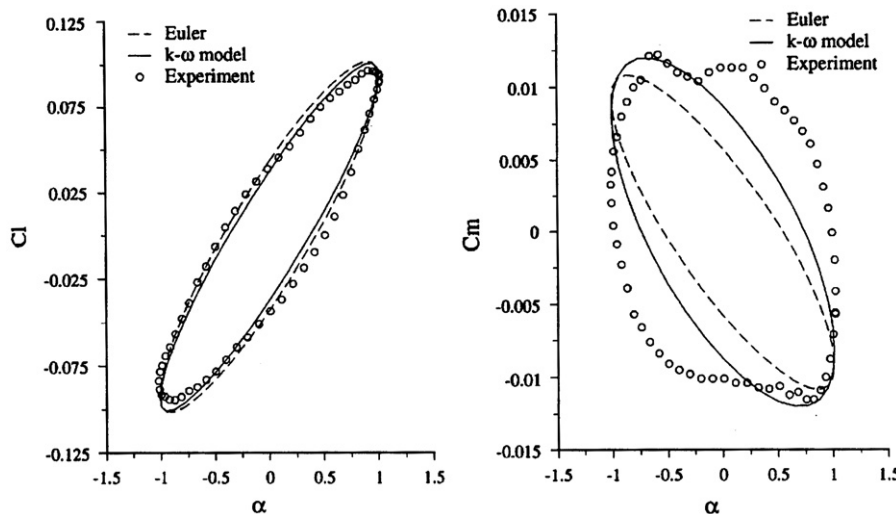

Fig. 13. Comparisons of Euler and Navier–Stokes calculations with experimental data. Adapted from Liu and Ji [85]. Experimental data from Davis [86] (AGARD CT6 test case: NACA 64A010 airfoil pitching about a quarter chord axis; $M_\infty = 0.796$; $k = 0.202$; $Re = 12.56 \times 10^6$; mean angle of attack $\alpha_m = -0.21°$; pitching amplitude $\alpha_0 = 1.01°$).

supersonic pocket terminated by a shock on the upper surface near the leading edge.

Results for pitching oscillations of an NACA 64A010 airfoil are shown in Figs. 13 and 14, comparing predictions from Euler and Navier–Stokes calculations [85] with experimental data [86]. The differences between the Euler and Navier–Stokes results for the unsteady lift coefficient are seen to be surprisingly small and both agree reasonably well with experiment. The Navier–Stokes results are in slightly better agreement from a phase relation standpoint. Pitching moment agreement is relatively poor, however, the moment amplitudes show reasonable agreement with experiment. The fact that the Navier–Stokes calculations also fail to capture the "bulge" in the moment coefficient phase plot suggests that the turbulence model is simply unable to capture the nonuniform changes of the pitching moment as the angle of

attack passes through zero in the pitching cycle. The source of these nonuniformities, which are apparent both on the up- as well as the down-stroke, remains to be explained and requires further study. It should also be noted that the experimental data do not exhibit the expected symmetry required if the flow on the upper and lower airfoil surfaces were identical and only shifted in temporal phase by 180°. This slight but noticeable asymmetry could be due to imperfections or other airfoil shape differences between the two surfaces, or nonuniformities in the temporal behavior of the unsteady flow on the upper and lower surfaces.

Other researchers using a variety of Navier–Stokes codes and turbulence models have obtained essentially the same lack of agreement for the moment coefficient. Thus, at the present time at least, the "unsteady bulge" phenomenon revealed in the experimental moment coefficient, Fig. 13, cannot be predicted
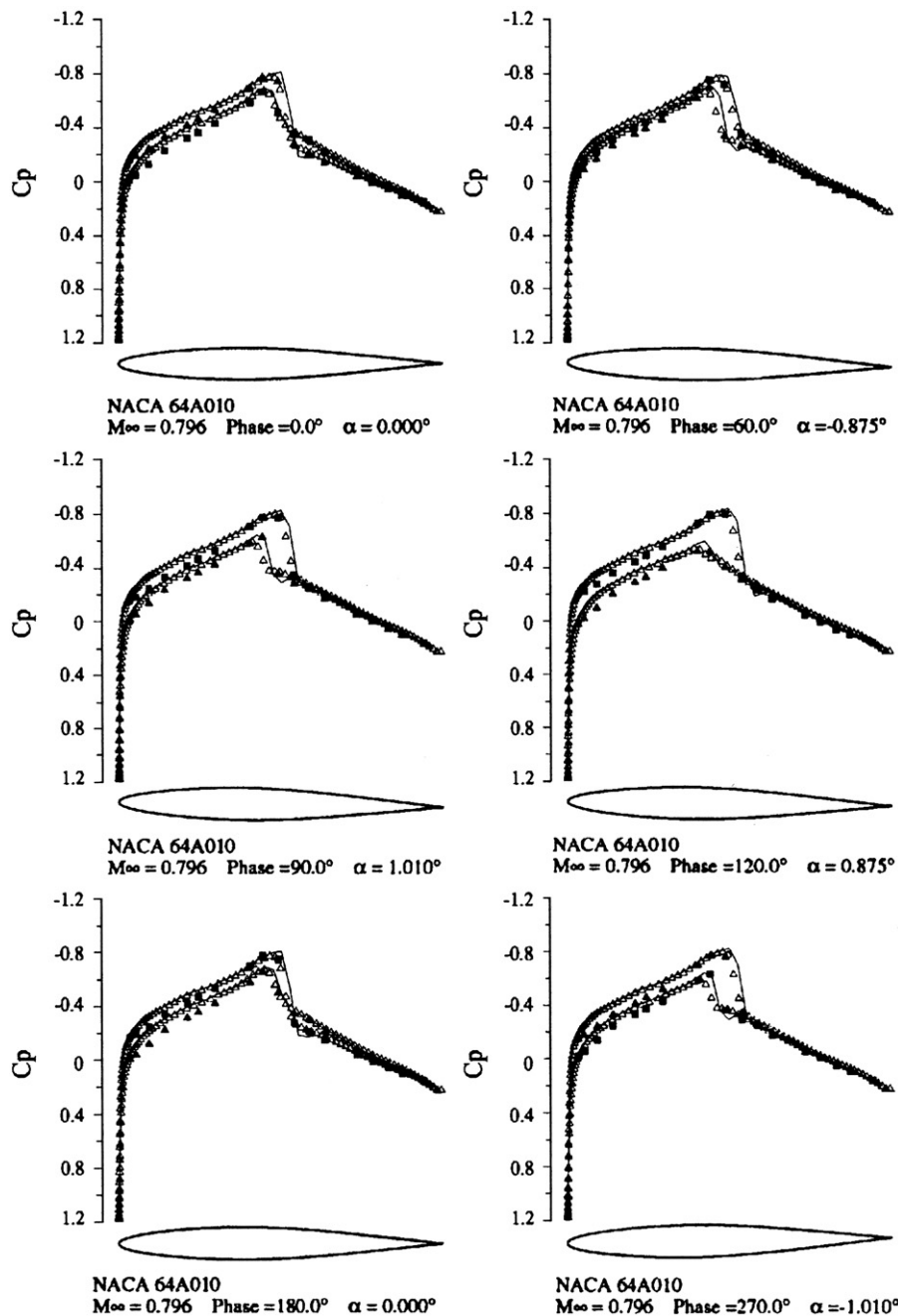

Fig. 14. Time snapshots of the unsteady pressure coefficient corresponding to case shown in Fig. 13 [85]: k–ω model (Δ); Euler (solid line); experiment upper surface (solid square); and experiment lower surface (solid triangle).
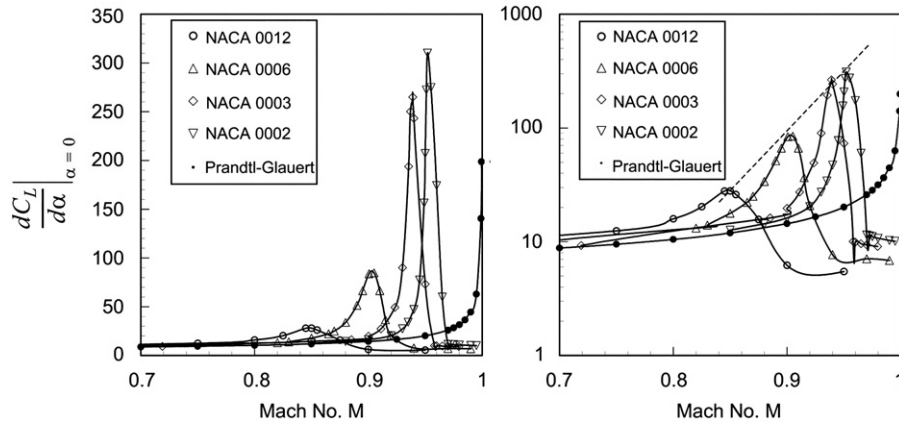
Fig. 15. Nonuniform (almost singular) behavior of the lift curve slopes of the NACA 00XX series of airfoils in transonic flow, and comparison with the Prandtl–Glauert rule (Euler calculations; linear and log scale).
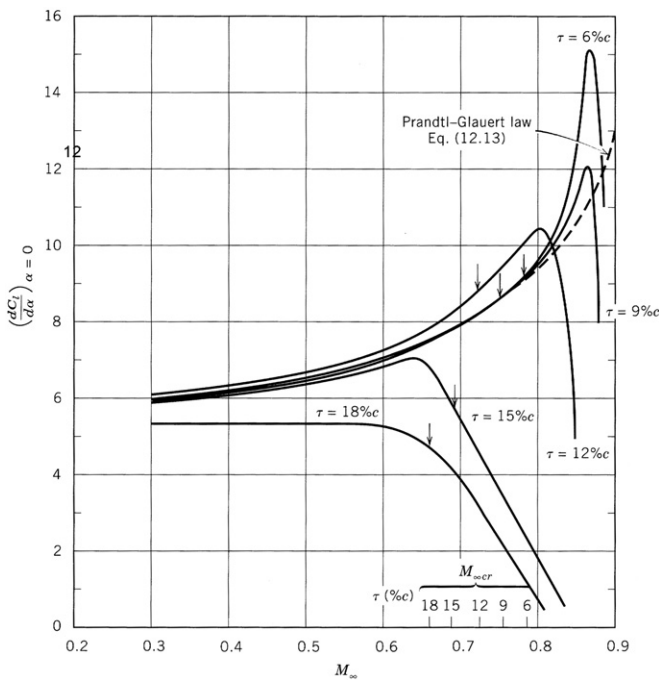

Fig. 16. Measured lift curve slope vs. Mach number for symmetric airfoils of different thickness ratios, at $\alpha=0$, and comparison with the Prandtl–Glauert rule for C_{L_α} at $M_\infty=0.3$. (From Ref. [88], adapted from Ref. [89]; original wind tunnel data from Göthert [90].)

Fig. 17. Predicted vs. observed location of Mach number at which C_{L_α} peaks, as a function of airfoil thickness [89,125].

using existing turbulence models and thin-layer Navier–Stokes codes.

5.2. Lift curve slope nonuniformity

The transonic similarity laws predict that the lift curve slope should scale as $1/\delta^{1/3}$, and a singularity results in the limit $\delta_2 \to 0$ (infinite C_{L_α}) [87]. The blowup occurs at Mach one, in the limit of a wing of zero thickness, and is in this respect similar to the classical Prandtl–Glauert singularity, but its strength is different. The moment coefficient derivative with respect to angle of attack has the same singularity; nevertheless, the lift and moment coefficients remain continuous and finite at Mach one in the nonlinear theory, in contrast to linear theory. Thus, the nonlinear transonic theory has succeeded in removing the Prandtl–Glauert $1/\sqrt{1-M_\infty^2}$ singularity from the aerodynamic coefficients, but the singularity in the lift and moment curve slopes is still there for
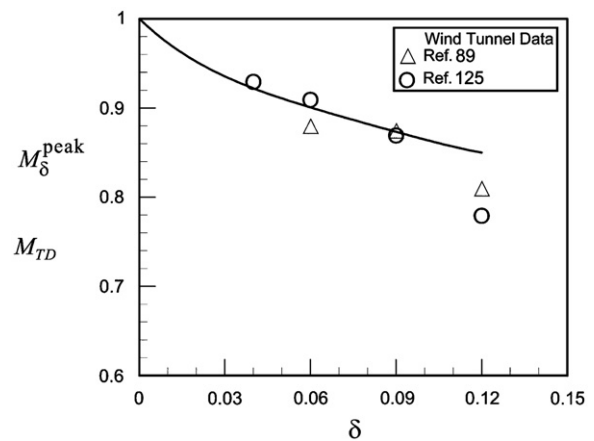
wings of zero thickness, albeit of a different strength. Of course, wings of zero thickness do not exist, and the singularity may seem more of a curiosity than a real engineering concern. In a real (viscous) flow, any non-infinitesimal angle of attack of a wing of infinitesimal thickness would cause leading edge separation, which would in all likelihood kill the singularity.

According to the transonic theory, the effect of a finite wing thickness ($\delta > 0$) is to replace the singularity by a sharp peak and move it to a slightly lower Mach number, away from Mach one. The sharpness of the peak should *increase* as δ *decreases*, becoming a singularity in the limit $\delta \to 0$, at least in the inviscid transonic small disturbance theory.

Fig. 15 shows representative results for the calculated lift curve slope evaluated at $\alpha=0$, as a function of airfoil thickness and Mach number. The peaks and subsequent rapid fall-offs bear a remarkable qualitative resemblance to the experimentally measured behavior of symmetric 2D sections shown in Fig. 16. The effect of viscosity appears to reduce the peaks and move them to slightly lower Mach numbers, because of the increase in the effective airfoil thickness caused by the boundary layer. What is surprising and of significance in an aeroelastic context, however, is that the locations of the C_{L_α} peaks scale with the locations of the bottoms of the transonic dips of the corresponding typical section aeroelastic models [87]. Furthermore, the corresponding Mach numbers follow the transonic scaling rules for airfoil thickness, up to a thickness of about 9%; see Fig. 17. The deviations observed for the 12% thick sections are most likely due to boundary layer

separation, as the deviation is in the expected direction (effective δ is increased).

In Ref. [87], the author concluded that the transonic dip is closely linked to the almost singular behavior of the lift curve slope, because the Mach number M_{TD} at the bottom of the primary transonic dip coincides with the Mach number M_δ^{peak} at which the lift curve slope peaks and exhibits almost singular behavior for small δ. From Fig. 15, it would appear that the peak values of $\log C_{L_\alpha}$ scale roughly linearly with Mach number, which suggests a scaling law of the form

$$\log C_{L_\alpha}^{max} = aM_\infty + b \tag{66}$$

where a and b are constants. Although this scaling does not suggest a blowup of the lift curve slope in the limit of zero airfoil thickness, the calculations cannot readily be extended down to $\delta \approx 0$ with CFD methods alone, because this limit is singular in several respects. In particular, the contribution from the singularity at the leading edge as the leading edge radius approaches zero cannot be captured with sufficient accuracy by standard CFD methods to decide the scaling question.

The highly nonlinear behavior of C_{L_α} vs. M_∞ at transonic Mach numbers is well-known (see Fig. 16, for example) and has been discussed at length in the aerodynamics literature [88,89]. However, the abrupt break of the lift curve slope vs. Mach number after reaching its peak has always been explained in terms of shock-boundary layer interactions. Because the almost-singular behavior and abrupt drop-off are also present in nonlinear inviscid transonic flow, it would appear that the part-span shocks by themselves must play a fundamental role in bringing about this behavior. The rapid drop-off of the lift curve slope is believed to be the main reason for the rapid rise in the flutter boundary immediately past the transonic dip. For thin airfoils the sharpness of the C_{L_α} peak is significantly greater and the subsequent drop-off is larger in the inviscid case. This suggests that Euler-based flutter calculations should be conservative in the sense that they should predict a lower minimum and sharper transonic dip than would be predicted using Navier–Stokes codes.

Of course, unsteady effects come into play as well, altering the "effective" lift curve slope. However, calculations indicate that for the relatively low reduced frequencies ($k < 0.1$) at which flutter is encountered in many transonic wind tunnel tests, the transonic dip flutter boundary would be expected to scale at least approximately inversely proportional to the effective lift curve slope. Fig. 18 shows results of unsteady Euler calculations for pure pitching oscillations about midchord for the NACA 0012 and NACA 0006 airfoils, as a function of reduced frequency and Mach number. Note that the nonuniformities with respect to Mach number remain in the unsteady lift amplitudes, although the peaks shift to slightly lower Mach numbers and weaken as the reduced frequency is increased. The unsteady moment coefficient shows a similar "peaky (almost singular)" behavior, which has a profound influence on the stability of SDOF pitching motions and the possibility of SDOF torsional flutter at transonic Mach numbers. This subject will be discussed in more detail in Section 7.1.

At transonic Mach numbers away from the C_{L_α} peaks, the lift and moment coefficients closely follow the transonic scaling laws, as shown in Fig. 19(a). But for Mach numbers close to the C_{L_α}
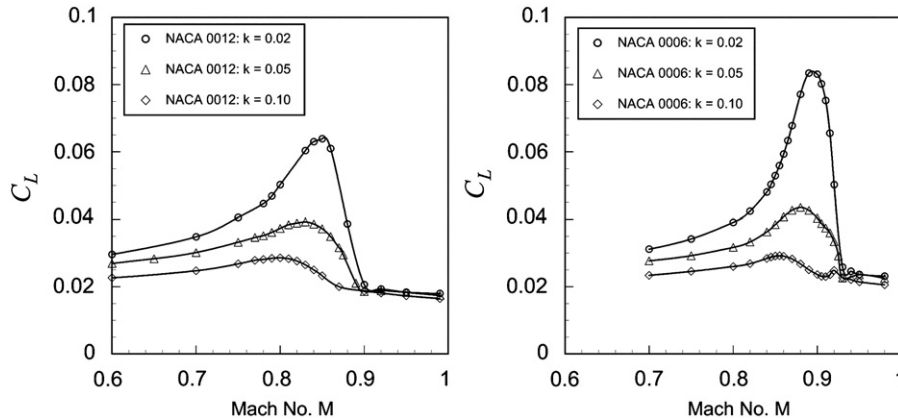

Fig. 18. Theoretical unsteady lift amplitude during pitching oscillations of NACA 0012 and NACA 0006 airfoils about midchord as a function of Mach number and reduced frequency $k = \omega b/U$ ($\alpha_m = 0$; $\alpha_0 = 0.2°$). Euler calculations. Note insensitivity to reduced frequency at high transonic Mach numbers.
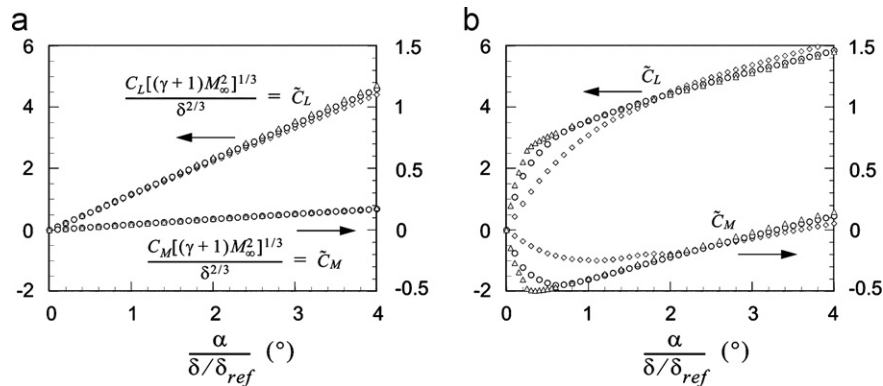

Fig. 19. (a) Illustrating the validity of the similarity laws for lift and moment coefficients of the NACA 00XX airfoils in the upper transonic region: NACA 0012 (diamonds), NACA 0006 (circles), and NACA 0003 (triangles) at $M_\infty = 0.90$, 0.9349, and 0.9581, respectively, corresponding to the same value of the aerodynamic similarity parameter ($\chi = 0.5014$); (b) same as (a), but near bottom of the transonic dip, at $M_\infty = 0.85$, 0.9006, and 0.9354, respectively, corresponding to the same value of the similarity parameter ($\chi = 0.7903$). Note highly nonlinear lift curve slopes and the breakdown of the scaling laws at *low* angles of attack (Euler calculations; $\delta_{ref} = 0.06$, corresponding to NACA 0006).

peaks, the slope of the similarity lift coefficient $\tilde{C}_L$ vs. $\tilde{\alpha}$ starts to *increase* with decreasing section thickness, Fig. 19(b), beyond what would be predicted by the similarity rules, and a strong nonlinearity develops in the lift and moment coefficients. The increase in lift curve slope for thin airfoils near zero angle of attack was observed in Ref. [41], but no explanation was given, although it was noted that the increase could not be predicted by the first-order transonic scaling laws. This is a rather curious anomaly, because one would expect the transonic scaling laws to get better and better as the wing thickness decreases, not the other way around, as is apparent in Fig. 19(b).

Because the C_{L_α} peaks appear to fix the location of the primary transonic dip, at least for two-dimensional typical sections, an attempt to understand this anomalous behavior was undertaken in Ref. [91]. After a re-examination of the limit process expansion procedure used in deriving the transonic scaling laws, it was realized that the limit $\delta \to 0$; α/δ fixed, is not the only limit of relevance in the case of flutter of thin wings. Because the shock motion is sensitive to the local airfoil curvature, there may be a particular span location (for a given family of airfoils) that will cause the largest shock displacement for a given small change in angle of attack. This hypothesis assumes that the peak in the lift curve slope occurs at a specific Mach number, which scales according to the transonic similarity laws, because the shocks are at a chordwise position where the lift increment per unit span ΔL_s produced by the shock displacements Δx_s from a small angle of attack increment $\Delta \alpha$ reaches its maximum, for a given family of airfoils. A close examination of the pressure distributions and shock displacements vs. $\Delta \alpha$ for different airfoils has convinced this author that the peak in the lift curve slope *is* produced by the shocks, and coincides with the maximum of the lift contribution from the shocks. For the NACA 00XX family of airfoils, this maximum occurs when the shocks are roughly at $0.75c$, where the shock excursion amplitude for a given $\Delta \alpha$ is at its maximum. The effect of viscosity should move the peaks to slightly lower Mach numbers and reduce their heights.

5.3. Effect of wing thickness

If one compares two wings with airfoils of the same family, but with different thickness ratios δ_1 and δ_2, then for similar flows the Mach numbers must satisfy the relation

$$\frac{(1-M_2^2)/M_2^{4/3}}{(1-M_1^2)/M_1^{4/3}} = \left\{\frac{\delta_2}{\delta_1}\right\}^{2/3} \tag{67}$$

where it has been assumed that the test medium (γ) is the same in the two tests. If $\delta_2 < \delta_1$, then it follows that $M_2 > M_1$. Thus a thinner wing is similar to a thicker wing of the same family operating at a lower Mach number. As the wing thickness is increased, transonic phenomena such as the transonic dip are shifted to lower Mach numbers, as shown in Fig. 20. Aeroelastically similar flutter points must also have the same value for the aeroelastic similarity parameter, $\psi_2 = \psi_1$, from which one concludes that

$$\frac{U_2/b\omega_\alpha\sqrt{\mu_2}}{U_1/b\omega_\alpha\sqrt{\mu_1}} = \left\{\frac{M_2^2\delta_2}{M_1^2\delta_1}\right\}^{1/6} \quad \left(\frac{q_2}{q_1}\right)_F = \left\{\frac{M_2^2\delta_2}{M_1^2\delta_1}\right\}^{1/3} \tag{68}$$

where the Mach numbers M_1, M_2 are related by Eq. (67). In the sonic limit, $M_2 \approx M_1 \to 1$ $(q_2/q_1)_F \to (\delta_2/\delta_1)^{1/3}$, suggesting that $q_2 \to 0$ if $\delta_2 \to 0$. That is, the flutter dynamic pressure at the bottom of the transonic dip should drop to zero as the wing thickness approaches zero and the Mach number approaches one. The reason for this is that the transonic scaling laws predict that the lift curve slope should scale proportional to $1/\delta^{1/3}$, indicating a singularity in the limit $\delta_2 \to 0$ (infinite C_{L_α}).
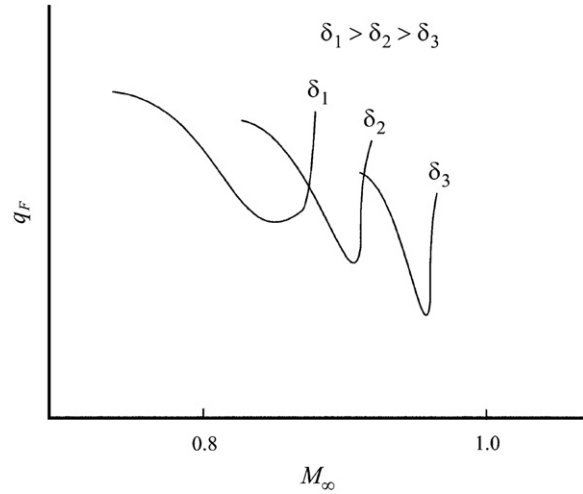

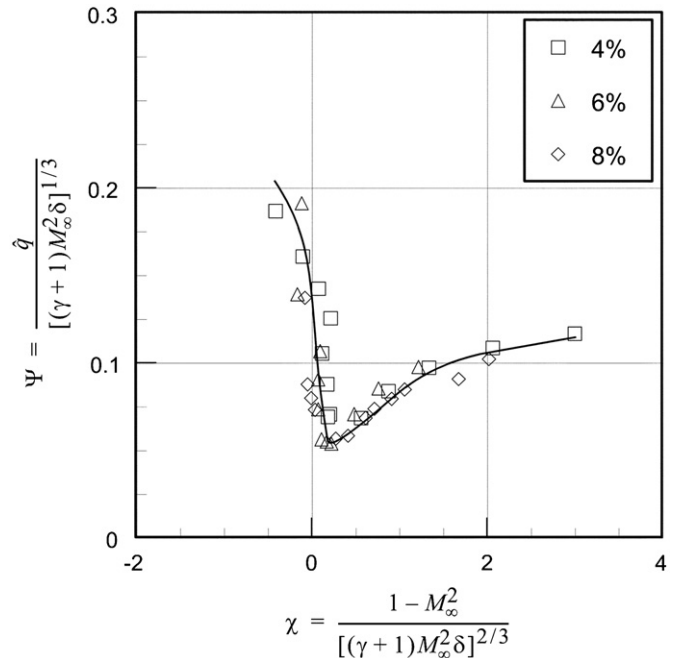**Fig. 20.** Qualitative sketch of the effect of wing thickness on the transonic flutter boundaries.

Fig. 21. Same data as in Fig. 2, after applying the transonic similarity rule for flutter.

Fig. 21 shows the wind tunnel test data in Fig. 2, corrected for wing thickness by plotting the data as the flutter similarity parameter ψ vs. the aerodynamic similarity parameter χ. The effect of angle of attack is in some (but not all) respects similar to the effect of thickness, because increasing α_∞ will increase the disturbances caused by wing as seen from the far field. By the similarity rules, the transonic dip should shift towards lower Mach numbers and up slightly as the angle of attack is increased. This is in agreement with the experimental data shown in Fig. 3.

5.4. Effect of test medium

The advantages of using a heavy gas in flutter testing are well-known, and include higher Reynolds numbers and lower mass ratios (closer to the actual wing), making it easier to design aeroelastically scaled models. Freon-12 has a significantly lower

speed of sound than air, resulting in velocities at a given Mach number less than half of the corresponding velocities in air. Consequently, for a given model, the reduced frequencies at flutter will be higher by more than a factor of two, whereas the critical mass ratio at flutter will be lower by an even higher factor. The flutter boundary, however, if plotted as a surface in 3-space, with each axis representing one of the primary similarity parameters, will not change as a result of the change in the speed of sound, because the speed of sound only enters the aerodynamic theory through the Mach number. However, the *flutter points* (on the flutter surface) obtained during testing in Freon-12 will be different than the corresponding flutter points in air.

Freon-12 has a value of γ which is significantly below that of air (1.13 vs. 1.4), which should lead to an observable shift in the flutter boundaries in the transonic region, where the aerodynamic nonlinearities are strongest. This is a *nonlinear* effect, as the linearized equations for unsteady aerodynamics do not depend on γ. For transonic similarity, the Mach number M_2 with Freon-12 as the test medium must be such that the similarity parameter χ is invariant ($\chi_2 = \chi_1$ point by point), which requires that

$$\frac{(1-M_2^2)/M_2^{4/3}}{(1-M_1^2)/M_1^{4/3}} = \left\{\frac{\gamma_2+1}{\gamma_1+1}\right\}^{2/3} = 0.9235 \qquad (69)$$

For similarity, the Mach number in the transonic region must therefore be increased slightly when testing in Freon-12, as compared to air, and the flutter boundary moves to the right by a small amount. Simultaneously, the boundary moves down, to satisfy the flutter similarity rule $\psi_2 = \psi_1$ for each point. The flutter dynamic pressures at the dynamically similar Mach numbers M_2 and M_1 given by Eq. (69) are related by

$$\frac{q_{F_{F-12}}}{q_{F_{air}}} = \left[\frac{(\gamma_2+1)M_2^2}{(\gamma_1+1)M_1^2}\right]^{1/3} \qquad (70)$$

valid in the transonic region. Thus the dynamic pressure at flutter should be lower in Freon-12 than in air, if dynamically similar points are compared. If the slope $\partial q_F/\partial M$ is positive or close to zero, the corresponding boundary in Freon-12 should also be lower at the same Mach number. In the transonic dip, however, this slope is negative over some region of Mach numbers, and here a higher flutter dynamic pressure may occur when testing in Freon-12 as compared to air.

According to the transonic similarity rules, the change in γ introduced by testing in R-12 can be compensated for by changing the thickness of the wing. If $(\gamma+1)\delta$ is kept constant, then there should be no change in the (inviscid) flutter boundary. For example, the 14% thick supercritical benchmark wing tested in R-12 should have the same flutter boundary as a dynamically identical wing of 12.42% tested in air, if the effects of viscosity are neglected.

The predictions of Eqs. (69) and (70) have been compared to flutter data from the NASA Benchmark Supercritical Wing, which was tested both in air and in Freon-12, see Fig. 22. The predicted shift is in good agreement with the experimental flutter data obtained in Freon-12.

6. Applications to transonic flutter calculations

6.1. Nonlinear computational aeroelasticity

Transonic flutter prediction remains one the most challenging problems in aeroelasticity, both from a theoretical and a computational standpoint. Linear flutter analysis methods have been quite successful in predicting the flutter behavior of wings at subsonic Mach numbers, below the transonic region, and this fact may be largely responsible for the continued dependence on doublet lattice flutter codes in aircraft design. But linear codes are inadequate for predicting the flutter behavior of wings at Mach numbers close to one, and the transonic aileron reversal and wing divergence speeds obtained by these codes are unreliable and of limited practical use to the designer.

The advances in Computational Aeroelasticity (CA) over the past 30 years have to a large extent been paced by the required developments in computational fluid dynamics (CFD). On the structural side, the development of the finite element (FE) method started earlier, gaining momentum with the introduction of digital computers in the 1950s. Finite element methods have by now reached an advanced state and large-scale commercial codes are available that can be used by engineers who are not necessarily experts on FE techniques. The CFD field is also sufficiently advanced that the central problems in computational aeroelasticity have shifted from the numerical solution of the unsteady flow and to the equally challenging problem of coupling CFD codes to FE codes, to produce accurate and reliable aeroelastic codes. However, many CFD codes are still hampered by a proliferation of esoteric schemes and a lack of any generally accepted standardization, which make their use in aeroelastic codes difficult and requiring expert knowledge beyond that normally possessed by flutter engineers.

6.2. Modeling requirements

A central question that has been addressed in numerous publications is the CFD code "selection issue", that is, potential vs. Euler vs. Navier–Stokes, etc. In the author's opinion, this question must ultimately be settled by experiments, specifically designed to give reliable error bounds on the unsteady aerodynamic forces and all aeroelastic variables affecting stability. The NASA Benchmark Models Program [92] and the DLR flutter tests on a 2D wing section [93–95] represented important first steps, but additional experimental research is clearly needed. For discussions of the CFD modeling issues in computational aeroelasticity, see the reviews of Försching [96], Edwards and Malone [27], and Edwards
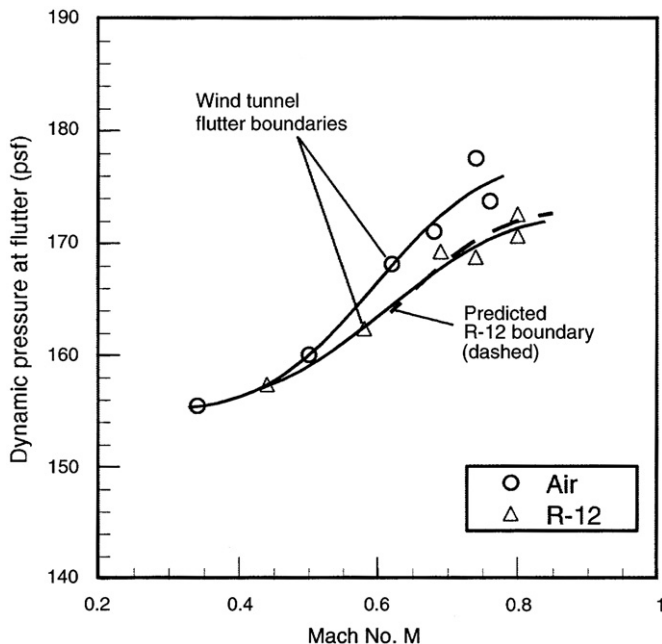
Fig. 22. Flutter boundary in Freon-12 as compared to air for Supercritical Benchmark Wing [87]. Also shown is the predicted shift of the flutter boundary (dashed line), based on the transonic similarity rules.

[28]. For a discussion of an alternative approach to computational aeroelasticity and computational aerodynamics, see Dowell and Hall [36]. The path-breaking research by Tijdeman on oscillating airfoils in transonic flow is still very relevant to anyone working in transonic aeroelasticity [97].

It might seem that the unsteady aerodynamic modeling requirements could be determined independently of any aeroelastic application, by direct comparison of theoretical or computational results with experimental data. There are two problems with this approach. First, different aeroelastic problems place different accuracy and fidelity requirements on the aerodynamic model. Second, the available experimental data on unsteady flows are seldom sufficiently complete and of a quality required to make uncontested conclusions, as should be clear from the examples discussed in this paper. The most reliable unsteady aerodynamic data available are from two-dimensional tests of typical section rigid models, as compiled in the AGARD volume, of which the NACA 64A010 transonic wind tunnel tests by Davis [86] are probably the most extensive; see also the more recent experiments by Schewe et al. [93–95].

As the number and complexity of unsteady aerodynamic codes used in aeroelastic applications continue to increase, it is impossible for the average aeroelastician to keep up with, or even be aware of, the latest developments in computational fluid dynamics. From a practical standpoint, it would be highly desirable to have a reliable yet simple classification scheme for aeroelastic problems and the modeling fidelity required for reliable aeroelastic stability calculations. If such a classification were possible, the flutter engineer could avoid some of the costly and time-consuming redundant validations of CFD-based aeroelastic codes during production calculations or in support of wind tunnel and flight testing. Unfortunately, there exists at present no reliable selection scheme based on physical and aeroelastic considerations, nor is there any plausible evidence that such a simple solution is likely to appear in the near future. All that can be offered are some broad guiding principles, based on a rough classification of the flow field, as follows:

Attached or essentially attached flows: At or close to design (cruise) conditions of a well-designed transport aircraft, one would expect essentially attached flows to dominate, at least on the wings. If a separation bubble exists, it should be small and not affect the global flow to a significant degree, nor the unsteady aerodynamic loads on the wing or lifting surface. The unsteady Euler equations may be expected to give qualitatively and quantitatively correct solutions, to within acceptable engineering tolerances. Outside the transonic region, linear potential methods may be used for sufficiently small flow perturbation amplitudes.

Flows with small to moderate localized unsteady separation: Examples include shock-boundary layer interactions, and trailing-edge separation at off-design conditions or during maneuvers. Reynolds-Averaged, Thin-Layer Navier–Stokes codes should give acceptable results, although experimental data suggest that the reliability and fidelity of the results are problem-dependent and sensitive to the turbulence model used.

Globally unsteady separated flows and vortex-dominated flows: Examples include high-angle-of-attack, high-g maneuvers of fighter aircraft, interactions between leading-edge vortex and separation bubble of highly swept wings, or wings with leading edge strakes (or severe cranks), and vortex instabilities or interactions at high angles-of-attack. These problems are on the borderline and in some cases somewhat outside the domain of validity of current RANS codes, depending on the complexity of the flow. Vortex-dominated unsteady transonic flows over highly swept delta or cranked delta wings representative of future supersonic transport designs have been difficult to predict (or even understand) based on calculations using current production RANS codes; see for example the data from the US High Speed Civil Transport (HSCT) program [98] and the recent review of unsteady aerodynamics of nonslender delta wings [99]. For these flows, LES and LES/RANS approaches [57,100] may be needed.
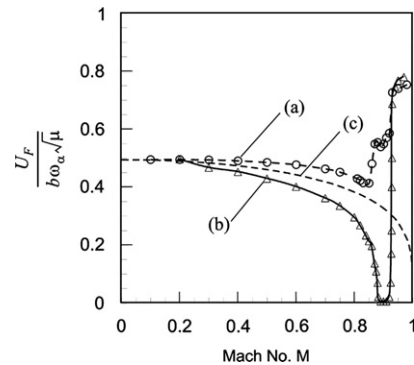

Fig. 24. (a) Flutter boundary for NACA 0006 model, corresponding to fixed mass ratio $\mu=20$; (b) corresponding boundary if $U_\infty = a_\infty M_\infty$ and μ is decreased until flutter occurs; (c) Theodorsen–Garrick rule for subsonic flutter. (Parts (a, b) from nonlinear Euler-based calculations; $g=0$).
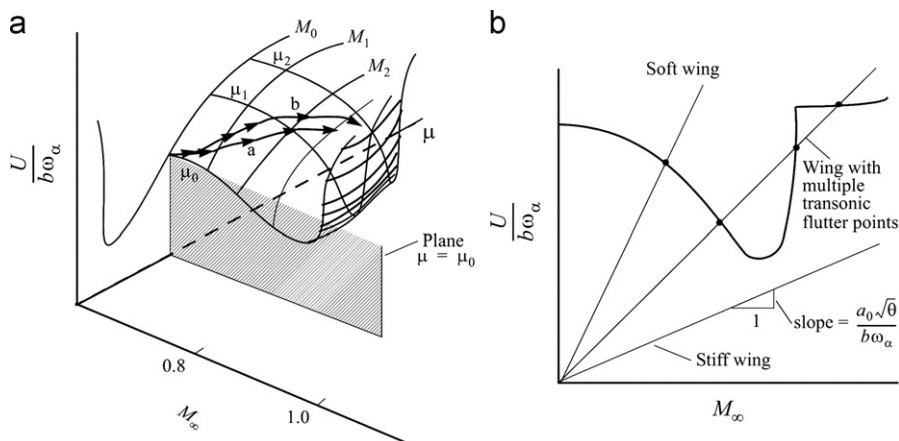
Fig. 23. (a) Flutter boundary as a surface in a 3D space of primary similarity parameters, with all other model parameters fixed. The observed flutter boundaries in wind tunnel tests are represented by curves or paths (a,b, etc.) on this surface, and may differ from test to test if the temperature changes. (b) illustrates how intersections between the flutter surface and planes representing testing at constant temperature and mass ratio depend on the stiffness of the wing.
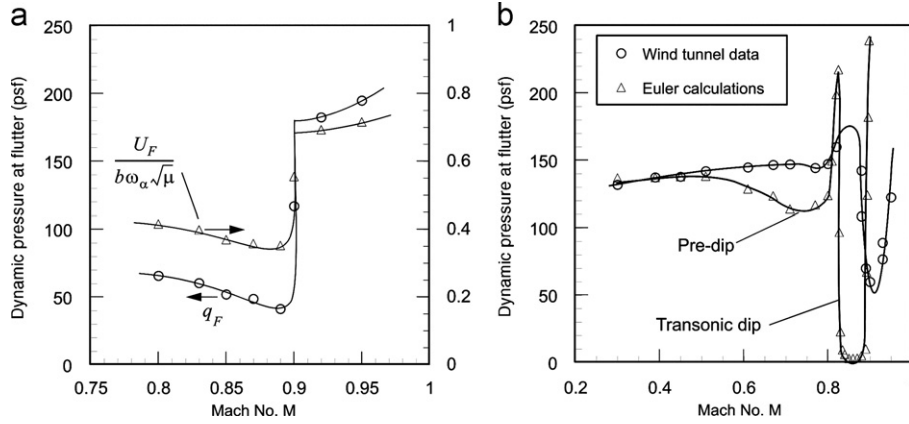
Fig. 25. (a) Transonic flutter boundary for NACA 0012 model, corresponding to fixed mass ratio $\mu=75$ and zero structural damping ($r_\alpha^2=0.25$ in these calculations, not 1.024 as shown in Table 1); (b) critical dynamic pressure at flutter for NACA 0012 Benchmark Model, as observed in wind tunnel test, and compared to typical section calculations (nonlinear Euler-based calculations; $U_\infty=a_\infty M_\infty$ and μ is decreased until flutter occurs; $g=0.0024$).

The above grouping is neither unique nor original and corresponds in a broad sense to the 3 different flow regimes (I–III) identified in the previous reviews of Edwards and Malone [27] and Försching [96].

6.3. The transonic flutter boundary

The most interesting aspect of transonic flutter is the appearance of a transonic dip in the flutter boundary. Neither the location nor the shape of the dip can be correctly predicted by linearized aerodynamic theories. Recent calculations show that in some cases two closely spaced transonic dips may occur, separated by a narrow stability cusp in the boundary. The multiple dips appear to be caused by a complex interaction between the "almost singular" behavior of the lift curve slope of thin wings at transonic Mach numbers, and the aft movement of the aerodynamic center with increasing Mach number. The location of the peak in the lift curve slope can be predicted using transonic similarity rules, and generally coincides with the bottom of the primary transonic dip, although there is a shift toward lower Mach numbers because of reduced frequency effects; see Fig. 18 and the accompanying discussion. The rapid drop-off of the lift curve slope after the peak is believed to be the main reason for the rapid rise in the flutter boundary immediately past the transonic dip.

The transonic flutter boundary can be represented as a surface in a three-dimensional parameter space, Fig. 23(a), with the three primary similarity parameters M_∞, μ, and $\overline{U}=U/b\omega_\alpha$ as coordinate axes.[3] It is not possible to get a complete understanding of the transonic flutter behavior of a wing from classical two-parameter plots of the linear flutter speed, or dynamic pressure, vs. Mach number. To understand why, one must first recognize that a 2D plot of $\overline{U}_F$ vs. M_∞ (for a fixed mass ratio μ_0) represents the projection of the actual 3D flutter curve "a" or "b" in Fig. 23(a) on the plane $\mu=\mu_0$, parallel to the $\overline{U}_F-M_\infty$ coordinate plane.[4] There is a corresponding projection, for each Mach number, of the 3D flutter curve onto a plane parallel to the $U_F/b\omega_\alpha-\mu$ coordinate plane and passing though the Mach number being considered. Because the actual path traced out on the flutter surface depends not only on the properties of the aeroelastic model, but also on the properties of the wind tunnel and the test procedure used, the two-parameter projections on the

similarity planes are not unique for a given aeroelastic model. Furthermore, the location and sharpness of the transonic dip depend on the path traced out on the flutter surface, and on the angle at which the "transonic valley" is entered. This can lead to confusion when attempting to interpret transonic flutter data based on two-parameter plots, especially if multiple transonic dips occur.

In computational flutter calculations, the mass ratio μ is usually kept fixed and the flutter boundary is plotted as $\overline{U}$ or $\overline{U}/\sqrt{\mu}$ vs. M_∞. In wind tunnel flutter tests, on the other hand, both the Mach number M_∞ and the density typically change from point to point, with μ often varying over an order of magnitude or more in a given test. The reduced velocity is fixed by the relation

$$\overline{U}=\frac{U_\infty}{b\omega_\alpha}=\left(\frac{a_0\sqrt{\theta}}{b\omega_\alpha}\right)M_\infty \tag{71}$$

where a_0 is the speed of sound at SLSD conditions and $\theta=T/T_0$ is the absolute temperature ratio. If the temperature is constant, then $\overline{U}$ is directly proportional to the free-stream Mach number M_∞. Thus, flutter testing at constant temperature will produce a flutter boundary that represents the intersection of the flutter surface, Fig. 23(a), with the plane given by Eq. (71), i.e., a plane passing through the μ-axis, with a slope $a_0\sqrt{\theta}/b\omega_\alpha$ with respect to the $M_\infty-\mu$ plane; see Fig. 23(b). But if the temperature is not constant during the test, or between different testing days, the slope of U vs. M_∞ will change, which will alter the reduced frequency and mass ratio at which flutter is encountered, and hence also the flutter boundary $\overline{U}_F$ or q_F vs. M_∞. Because the sensitivity to temperature depends on the local slope, $\partial\overline{U}/\partial\mu$, different aeroelastic models will generally show different sensitivity to changes in temperature. Note that, whereas the 2D boundary is affected, the 3D flutter surface is unaffected by temperature changes.

It is therefore important to distinguish between flutter boundaries at constant mass ratio (altitude), and boundaries obtained in a variable-density wind tunnel. As shown in Figs. 24 and 25, the two cases may yield completely different boundaries in the transonic region, even for the same aeroelastic model. The first example is an NACA 0006 typical section model that has been used in several previous studies [29,52,87]. The second model is an NACA 0012 airfoil with typical section parameters identical to the NACA 0012 Benchmark model tested at the NASA Langley Research Center [92] (Table 1).

These two simple examples demonstrate that two-parameter transonic flutter boundary plots must be interpreted with caution. The reason for the drastic differences between the boundaries in

---

[3] Using the transonic similarity parameters χ, ψ, and $\overline{U}$ would give the most general boundary, allowing for changes in wing thickness, aspect ratio, and test medium (different models and tests).

[4] At very low mass ratios a unique flutter surface may not exist, because period-tripling bifurcations to a new flutter mode may occur; see Section 7.6.

parts (a) and (b) of Figs. 24 and 25 is that the boundaries represent different paths on the flutter surface (cf. paths (a) and (b) in Fig. 23(a)); thus their projection on the 2D similarity planes will differ. In the transonic region, the flutter surface typically contains one or more sharp valleys (transonic dips), and in this region the projected two-parameter boundaries become very path-dependent. It should be noted that whenever Eq. (71) is enforced, the reduced frequency at flutter drops as the Mach number increases, which also affects the shape of the boundary.

7. Understanding nonlinear transonic flutter phenomena

7.1. Single-degree-of-freedom flutter

A compelling reason for arguing that transonic flutter is not classical bending–torsion flutter in the Theodorsen–Garrick sense is the existence of a single-degree-of-freedom (SDOF) torsional flutter instability near the bottom of the transonic dip. This SDOF instability is very different from the linear subsonic SDOF torsional flutter known in the classical literature [101,102], which requires very low reduced frequencies and a torsional axis forward of the quarter chord.

Surprisingly, even though the SDOF torsional flutter may be possible at a given Mach number and reduced frequency, it can usually only be observed indirectly, through its interaction with the bending–torsion flutter mode. The reason for this is that only the least stable aeroelastic mode is typically observable in a wind tunnel test, or in a time-marching flutter simulation, and in most cases this is the bending–torsion flutter mode. But at sufficiently high mass ratios, the SDOF instability near the bottom of transonic dip does emerge; see Fig. 26. Wind tunnel data from the DLR tests of the NLR 7301 wing also reveal the presence of a SDOF torsional flutter instability near the bottom of the transonic dip [93,94]; see Fig. 27.

Experimental evidence of a SDOF torsional flutter instability at the transonic dip was obtained some 60 years ago in wind tunnel tests by Bratt and Chinneck [103] and Bratt et al. [104] of a series of airfoils permitted only a single degree of freedom in pitch, Fig. 28. Note the extremely sharp drop in the damping in pitch around Mach 0.85, reaching a bottom in negative damping

(flutter) around Mach 0.87, followed by an equally sharp rise to positive damping as the Mach number is increased past about 0.88. Lambourne discusses this case in Ref. [105], noting that it was suggested that the instability can probably be associated with shock-induced separation, "…although as far as is known, no physical explanation for the instability has been advanced."

In fact, it would be very difficult to explain the extreme behavior of the damping curve based on flow separation alone. If flow separation triggers the rapid loss of damping at Mach 0.85, how can the same mechanism be responsible for the dramatic rise in damping as the Mach number is increased by a mere 0.03? Note that the location of the negative damping peak coincides with the expected location of the transonic dip of a 10% thick airfoil (Fig. 17), suggesting that the instability is triggered by aerodynamic nonlinearities, not separation. Additional SDOF pitching instability results from Bratt et al. [104], are consistent with this assessment.

Although this SDOF torsional flutter data have been discussed briefly in subsequent papers [105,106], no further analysis of the flutter mechanism appears to have been published. It is interesting to note that, at about the same time, Whitehead [107] showed that for cascaded airfoils in turbomachinery rotors, SDOF torsional instabilities are predicted for both incompressible and subsonic flows, outside the transonic region. Platzer and Chalkey [108] and Verdon and McCune [109] later showed similar SDOF torsional instabilities in supersonic cascade flows, representative of large fan rotors. However, coupled-bending torsion flutter can also
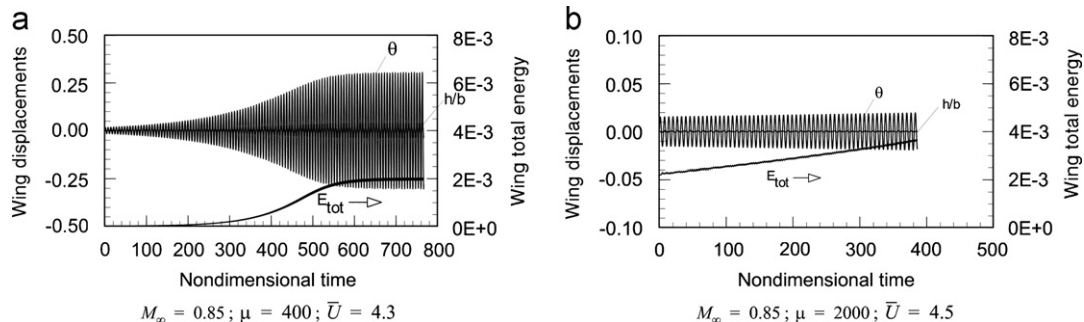
Table 1
Aeroelastic models.

Model	a	x_a	r_α^2	ω_h/ω_α	μ[a]
NACA 0006	−0.20	+0.20	0.25	0.20	20
NACA 0012	0.0	0.0	1.024	0.6462	75

[a] For cases where mass ratio is kept constant.
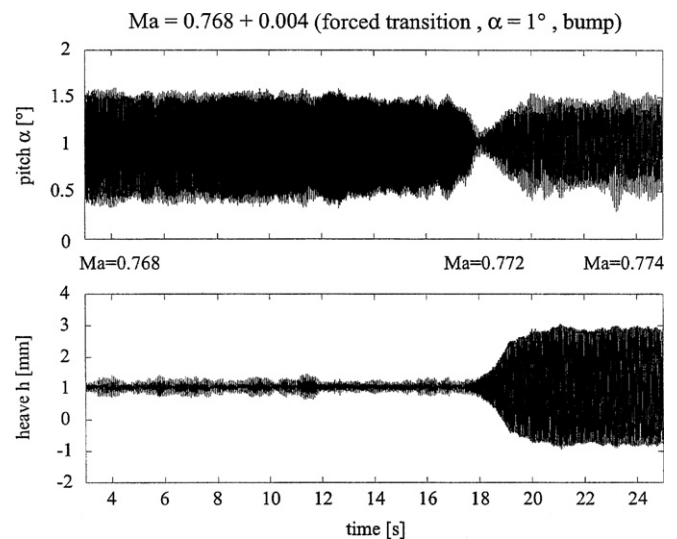
Fig. 27. Transition from SDOF torsional flutter to coupled bending–torsion flutter, as observed in wind tunnel tests of NLR 7301 model at DLR [93,94].

Fig. 26. Emergence of SDOF torsional flutter at the bottom of the transonic dip of the NACA 0012 Benchmark Model: (a) at intermediate mass ratio and (b) at high mass ratio (g=0.0024).

occur; see Bendiksen and Friedmann [110] and Bendiksen [111]. In transonic rotors with in-passage shocks, almost pure bending mode flutter is also possible [112].

Fig. 29 shows plots of the calculated net aerodynamic work ΔW_A done by the unsteady aerodynamic forces during one pitching cycle of the 10% thick RAE 102 airfoil tested by Bratt and Chinneck [103], for different mean angles of attack and reduced frequencies. The pitching axis is as in the experiments at 0.455c, and the calculations are based on the unsteady Euler equations. Note that a positive ΔW_A indicates an instability in pitch, and corresponds to negative damping in Fig. 28. Although viscosity is neglected in these calculations, the rapid changes in ΔW_A in the Mach number range 0.75–0.90 bear a strong qualitative resemblance to the experimentally observed behavior of the aerodynamic damping, Fig. 28, after accounting for the opposite signs. The theoretical region of SDOF torsional flutter is slightly wider, extending down to about Mach 0.78 for the 3° angle-of-attack case shown in Fig. 28, but the region becomes narrower and more like the experimental curve as the mean angle of attack is lowered, Fig. 29(a). Note that the calculations agree with experiment in that both show the disappearance of the SDOF flutter instability around Mach 0.9. Also, the increase in aerodynamic damping immediately before the torsional flutter
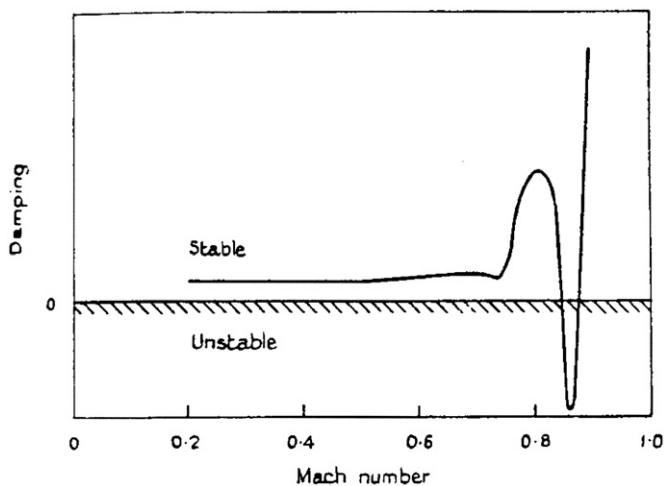
region, as observed experimentally (Fig. 28), is also predicted by the Euler calculations.

Fig. 30 shows similar calculations for NACA 0006 and NACA 0012 airfoils oscillating in pitch about a midchord axis. Again a SDOF torsional instability is indicated for a narrow band of transonic Mach numbers at and near the transonic dips. Also note the shift in the unstable region to lower Mach numbers as the airfoil thickness is increased from 6% to 12%, in agreement with the transonic similarity principles.

7.2. Multiple (nested) limit cycles

Transonic limit cycle flutter, or LCO (limit cycle oscillations) as it is sometimes called, has been observed in a number of aircraft in flight, in wind tunnel tests of several different aeroelastic models, as well as in time-marching and other nonlinear transonic flutter calculations. The physical mechanism behind the observed LCOs has been the subject of numerous investigations over the years, and several potential mechanisms have been proposed.

7.2.1. NLR 7301 unswept wing section

Wind tunnel flutter tests at DLR in Göttingen [93,94] of a "two-dimensional" wing section with an NLR 7301 supercritical airfoil, Fig. 31, have demonstrated that limit cycle flutter can and does occur even in the absence of noticeable flow separation or structural nonlinearities. Near the transonic dip, a complex and highly nonlinear flutter behavior was observed even at small amplitudes, and the flutter mode undergoes rapid changes in response to small changes in Mach number. For example, a transition from bending–torsion flutter to single-degree-of-freedom torsional flutter (and vice versa) could be triggered through a small change in Mach number or angle of attack, Fig. 27. This sensitivity to Mach number is to be expected from the nonlinear theory of transonic flutter [87], and is strongly influenced by the part-chord shocks on the wing surface.

An intriguing result of the NLR 7301 wing flutter tests was the discovery of multiple or "nested" LCOs with different amplitudes, coexisting at the same Mach number and angle of attack, Fig. 31. It was observed that transition from the "lower" to the "upper" LCO, and vice versa, could be accomplished by applying relatively small force perturbations in the plunge direction, either in-phase or out-of-phase with the plunge velocity at the elastic axis (at quarter chord), providing short bursts of negative or positive structural damping.

Fig. 28. Aerodynamic damping of a 10% thick airfoil pitching about an axis 0.455c from leading edge. Mean angle of attack 3°; amplitude 1°; $k=\omega b/U_\infty$ varies between 0.08 and 0.02. Adapted from Lambourne [105] (data from Bratt and Chinneck [103]).
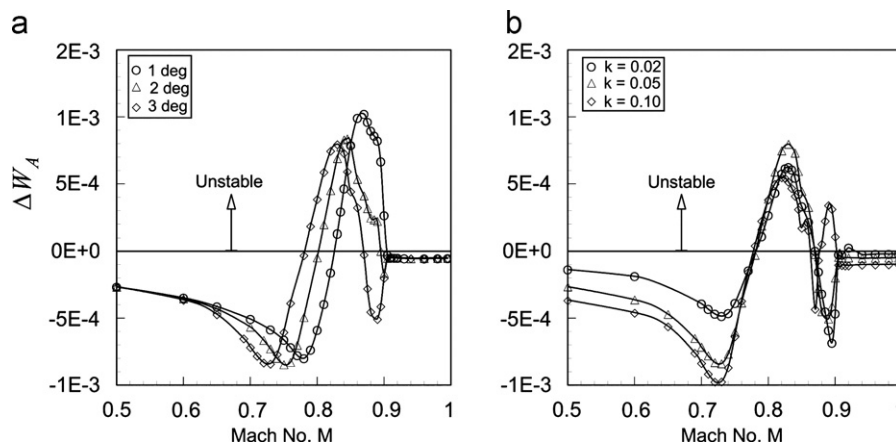

Fig. 29. Aerodynamic work ΔW_A per cycle of a 10% thick RAE 102 airfoil oscillating in pitch with an amplitude of 1° about an axis at 0.455c: (a) as a function of angle-of-attack with $k=0.05$ and (b) as a function of reduced frequency at an angle of attack of $\alpha_\infty=3°$.

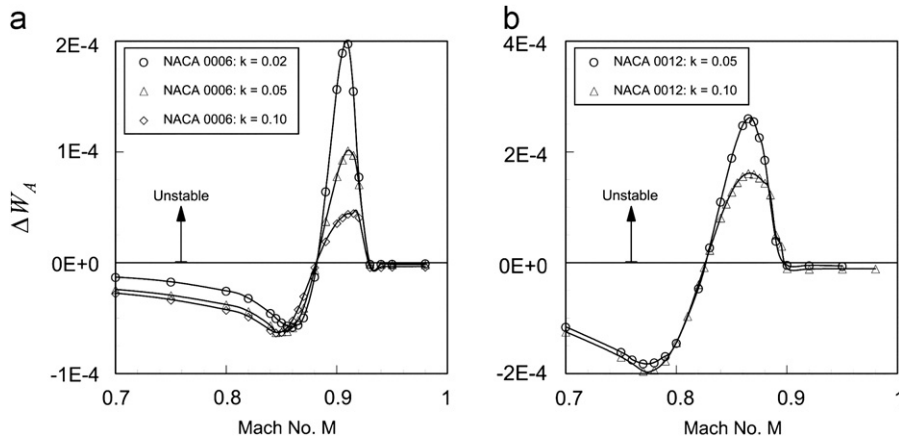**Fig. 30.** Aerodynamic work ΔW_A per cycle of (a) NACA 0006 and (b) NACA 0012 airfoils oscillating in pitch about an axis at midchord with amplitudes of 0.2° and 0.4°, respectively. The mean angle of attack is zero.
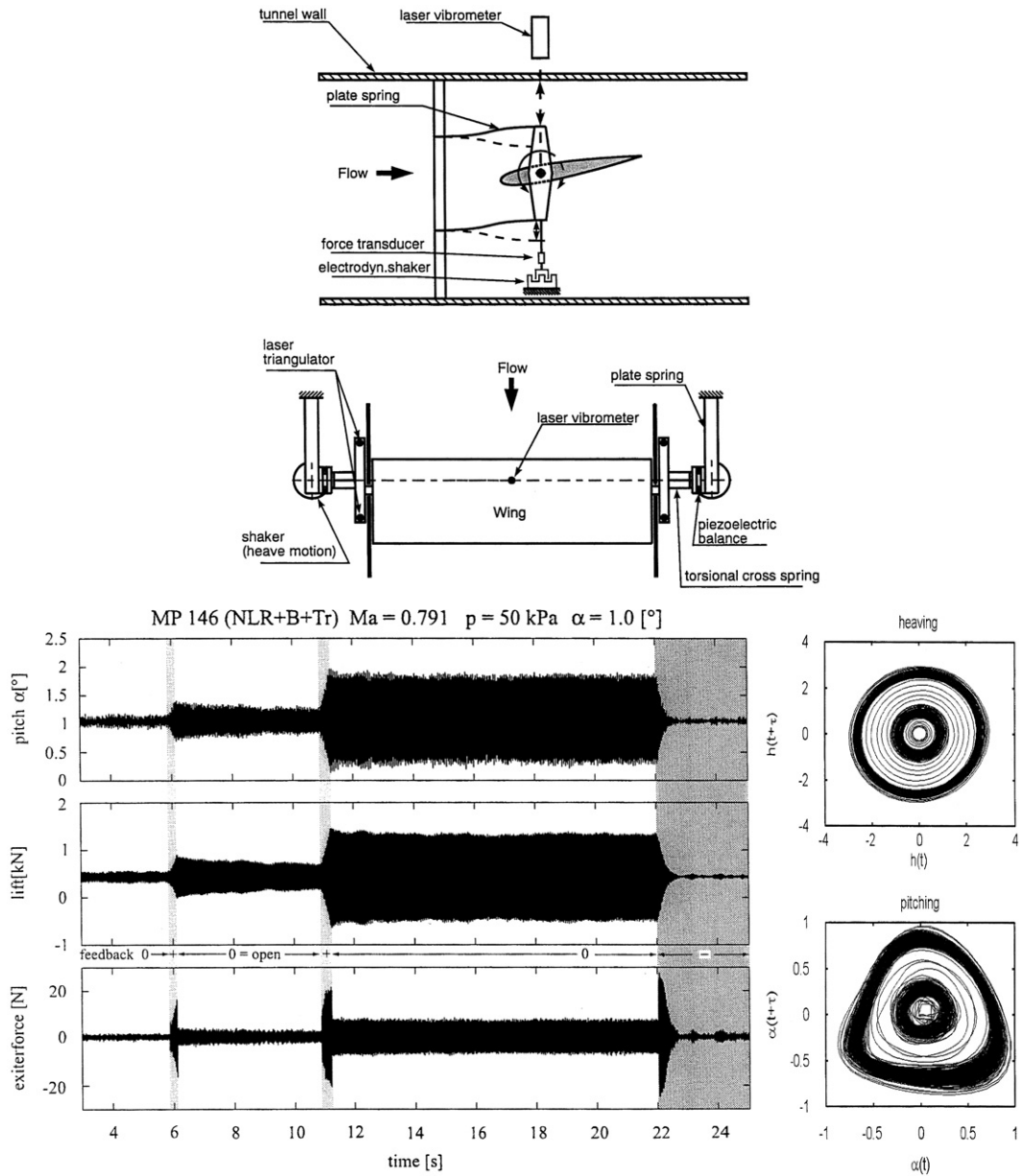

Fig. 31. NLR 7301 wing model test setup in the transonic wind tunnel at DLR (top); multiple (nested) limit cycles observed during flutter tests (bottom). Adapted from Ref. [114].

Fig. 32 shows representative results of Direct Eulerian–Lagrangian calculations for the NLR 7301 wing, revealing the presence of nested or multiple LCOs at a fixed Mach number. Additional calculations show that the multiple LCOs exist over a range of neighboring transonic Mach numbers and angles of attack. The fundamental physical mechanism behind the multiple limit cycles cannot be attributed to viscous effects (e.g., trailing edge separation), because the nested LCOs here appear in Euler-based calculations. A physical explanation for the observed nested limit cycles was offered in Ref. [113], in terms of the influence of the part-chord shocks and the stabilizing effect of a transition from Tijdeman Type A to B shock motion. For a highly nonsymmetrical wing section such as the NLR 7301, Type A to B shock transitions occur at different amplitudes on the upper and lower wing surfaces. Thus, two nested LCOs would be expected. By examining unsteady pressure coefficient data from a number of time-marching simulations, it was concluded that the lower LCO was caused by a transition from Type A to B shock motion on the lower wing surface, whereas the upper LCO was caused by a Type A to B transition on the upper surface (Fig. 33). Although the effects of trailing edge flow separation and/or structural nonlinearities are important in determining the final amplitude of the outer LCO, the computational results suggest that neither is essential in order to explain the existence of the observed nested LCOs.

Recent results from time-marching flutter calculations [115] suggest that the shocks also influence the stability of the inner limit cycle, making it very sensitive to initial conditions and control parameters and introducing a nonuniformity on the time scale that eventually destroys the stability of the LCO. Amplitude instabilities will eventually surface and the LCO either decays to zero and vanishes, or the amplitude grows until the inner LCO "morphs" into the outer LCO. This scenario may provide an explanation for why the prediction of the small-amplitude LCOs observed during wind tunnel tests of this wing has been so difficult; see, for example Refs. [116–118]. Unless the computational code is capable of modeling the energy exchange between the fluid and the structure with sufficient spatial and temporal accuracy, the weakly attracting inner LCO will simply not be detected, resulting in an LCO amplitude prediction that is off by an order of magnitude or more.

7.2.2. Swept transport wing

In linear subsonic flow, swept wings of moderate to high aspect ratio are susceptible to bending–torsion flutter, wherein energy is extracted from the airstream at a sufficient rate to produce rapidly growing flutter amplitudes. The effect of aft sweep is predicted to be stabilizing, in agreement with wind tunnel tests by Barmby et al. [119], although the benefit is usually less than what would be predicted based on classical sweep-back theory. In the transonic region, however, moving shocks on the wing surface tend to limit the energy flow to the wing and limit
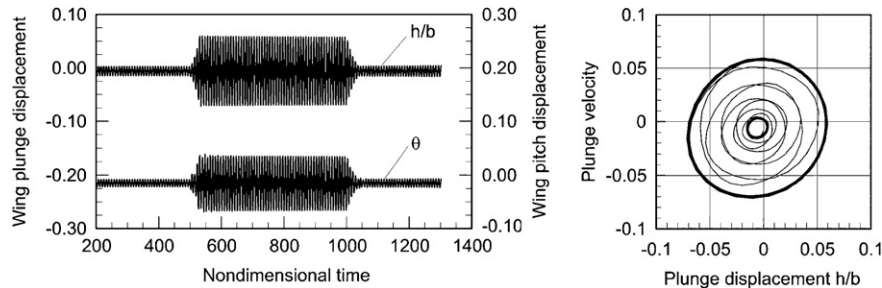
Fig. 32. Multiple (nested) LCOs for NLR 7301 wing, as predicted using the Direct Eulerian–Lagrangian scheme. Transition from lower to upper LCO is accomplished in the same manner as in the DLR experiments, by applying negative structural damping forces over a brief time interval with $g_h = -0.2$. A short application of positive damping forces with $g_h = 0.2$ brings the LCO amplitudes down to the small limit cycle again [115].

Fig. 33. (a) Qualitative explanation of multiple LCOs for NLR 7301 wing model and (b) possible nesting configurations of multiple LCOs [115].

cycle flutter becomes a real possibility. Although less common than for low aspect ratio wings, limit cycle flutter has been observed in wind tunnel tests by Dietz et al. [120], of a clean swept wing representative of current transport aircraft.
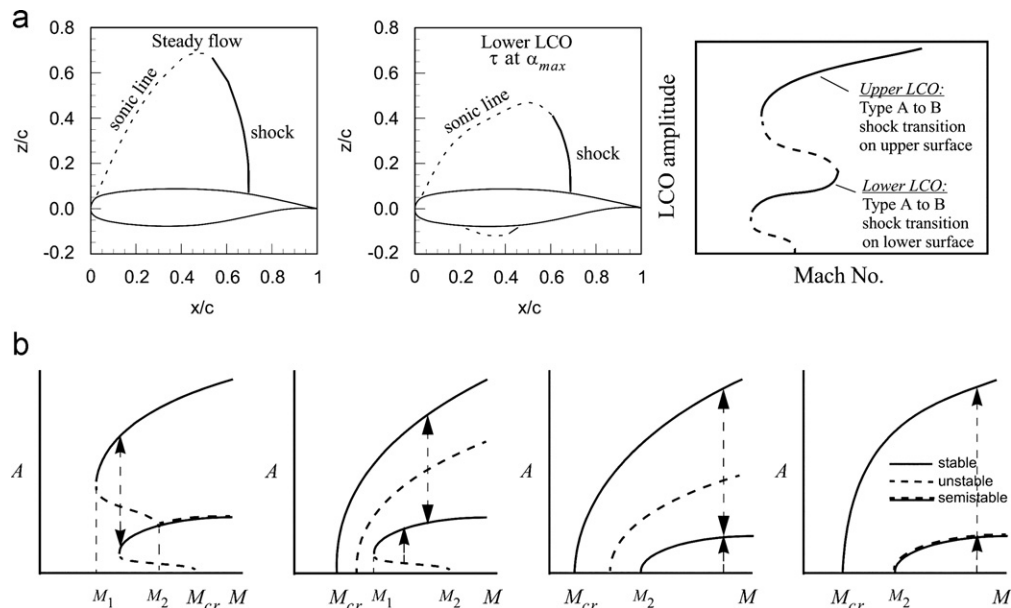
The G-Wing, Fig. 34, is closely similar in planform to the wind tunnel model studied in Ref. [120], except that the two small trailing-edge kinks have been ignored, and the airfoil section is the 10% thick ONERA "D" airfoil rather than the supercritical airfoil of the Göttingen wing. Although previous calculations by the author [121,122] made use of both a linear and a nonlinear structural model, it was concluded that the linear model gave entirely unsatisfactory results and failed to predict the observed LCO at anywhere near the correct dynamic pressure. Because the effective structural washout is not only a function of the sweep angle but also of the wing deflections, and hence also the wing loading, this coupling results in an inherently nonlinear aero-elastic problem, and neither the aerodynamic nor the structural nonlinearities can be ignored—even in a first approximation.

In Refs. [121,122], the author suggested that the experimental results in Ref. [120] could be explained through the effect that the structural washout (Fig. 35) from wing sweep has on the Type A to B shock transition. As the wing bends, the washout reduces the angle of attack of streamwise chord sections, unloading the outboard region of the wing, reducing the shock strengths and shifting the upper surface part-chord shocks in the upstream direction. The weaker and more forward shocks lead to an earlier

transition (at lower amplitudes) from Type A to B shock motion, resulting in a limit cycle flutter mode that persists over a relatively wide range of dynamic pressures and air densities (altitudes).

For swept wings of high aspect ratio, the influence of the wing deformations are further amplified through the structural wash-out mechanism, and the effect on flutter can be profound and in some cases lead to counterintuitive stability behaviors. In the case of the G-Wing, a complex LCO-type flutter behavior was observed involving two coexisting or nested limit cycles over a range of transonic Mach numbers between roughly 0.84 and 0.96 (Fig. 36). At some Mach numbers and density altitudes, both LCOs are stable; at other flight conditions one or both LCOs were found to be weakly unstable. A strikingly nonlinear and unexpected behavior was observed with respect to changes in dynamic pressure or altitude, Fig. 37, suggesting the possibility of "high-altitude flutter" [122]. As shown in Fig. 37, at Mach 0.95 the wing is stable below a density altitude of roughly 15,000 ft, yet encounters strong LCO-type flutter at altitudes well into the stratosphere. To the author's knowledge, no definite experimental verification of high-altitude flutter has ever been published in the open literature, although he is aware of anecdotal evidence of encounters with this phenomenon during flight tests.

The counterintuitive flutter behaviors shown in Figs. 36 and 37 arise because of strong interactions between the structural and aerodynamic nonlinearities, in which the embedded supersonic

G-Wing

$$A = 7.05$$
$$\Lambda_{LE} = 31.86°$$
$$\Lambda_{TE} = 21.02°$$
$$\lambda = 0.41$$

Computational Domain
No. of nodes: 43,344
No. of faces: 430,975
No. of cells: 208,926

No. of structural plate elements: 96
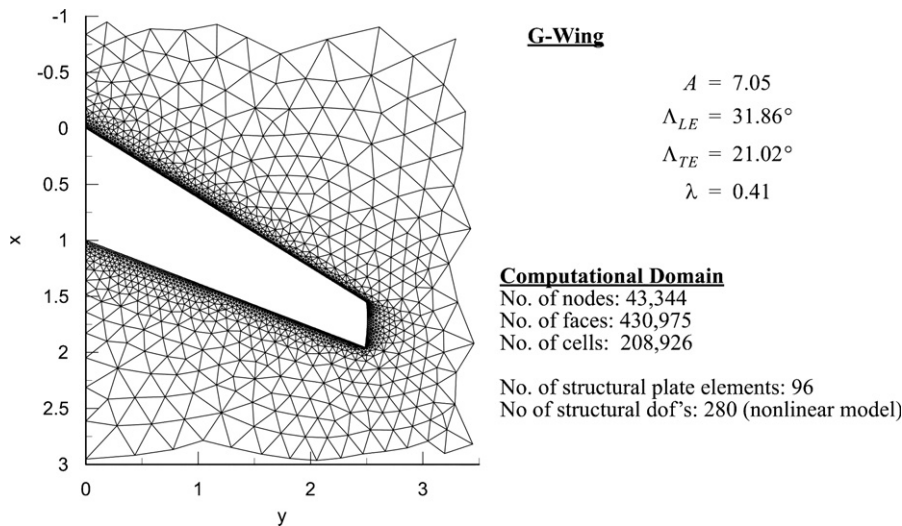No of structural dof's: 280 (nonlinear model)

Fig. 34. The G-Wing (generic transport wing) of similar planform to the wing studied experimentally in Ref. [120].
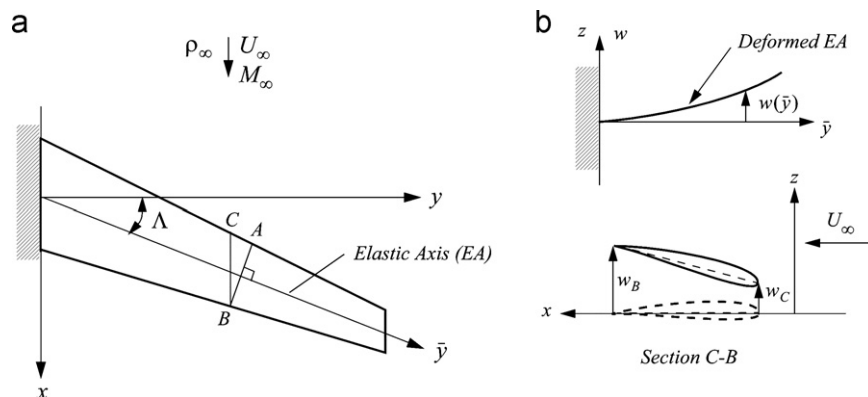

Fig. 35. (a) Chordwise segment A–B vs. streamwise segment C–B of a swept wing and (b) structural washout effect (reduction of angle of attack of streamwise segment C–B, because $w_C < w_B$).

pockets and the moving shocks on the wing surface play a crucial role. This conclusion is supported by the later calculations in Ref. [44], wherein detailed calculations of the energy transfer from the airstream to the wing were presented. It was concluded that the LCO behavior is strongly influenced by not only the shock amplitudes but also by the mean position of shocks on the upper and lower wing surfaces. If the shocks are too far forward, the shocks are stabilizing and no limit cycle flutter is observed. When the shocks are close to the midchord position over the important outboard region of the wing, the strongly nonlinear transonic flutter region is entered. This happens around Mach 0.84 for the G-Wing, and coincides with the start of the LCO flutter instability region, Fig. 36. Additional results (not shown) indicate that the LCO is the result of a delicate balance between the positive aerodynamic work done on the wing inboard of about 75% span, and the negative work done on the outer 25% of span [44].

A similar dependence on the chordwise location of the upper surface shock would also be expected in the viscous case, because the aerodynamic power and work per cycle depend primarily on the extent of the supersonic region on the upper surface, and on the local Mach number distribution in this region. If the steady or mean shock is in the dangerous $0.6c$–$0.8c$ region, boundary layer separation or other viscous interactions causing shock reversal (forward movement) would be expected to be stabilizing. However, if the shock is behind $0.8c$ but not yet at the trailing edge, shock reversal could be destabilizing, if it brings the shock back into the $0.6c$–$0.8c$ region. The increased rearward movement of the lower surface shock, Fig. 9, should be stabilizing.

From the results in Refs. [121,122], it appears that an inviscid analysis correctly identifies the low-amplitude LCO mode observed in wind tunnel tests of the Göttingen wing [120]. This suggests that viscous effects, such as shock-boundary layer interactions, may not play a fundamental role in causing the observed LCO-type flutter instability in this case, but rather enter the problem as another mechanism through which the energy flow from the fluid to the structure is further reduced or otherwise modified as the LCO amplitudes increase.

Somewhat surprisingly, calculations [115] indicate that the G-Wing also has nested LCOs over a range of transonic Mach numbers; see Figs. 38 and 39. The small-amplitude LCO is reached by starting the time-marching from the converged *static* aero-elastic solution, or from an adjacent LCO at a slightly lower or higher Mach number, as in a Mach number sweep at constant density. The outer LCO is reached by starting the solution from the steady solution around the corresponding *rigid* wing, which introduces relatively large unbalances in the unsteady aerody-namic forces on the wing during the first few time steps, simulating what might happen during a gust encounter.

Although no evidence of multiple LCOs was reported in the wind tunnel tests of the similar Göttingen wing, it should be noted that special initial conditions would be necessary to discover the outer LCO. Unless a sufficiently large initial disturbance is provided, the aeroelastic solution will converge to the lower-amplitude inner LCO. At higher transonic Mach numbers, in the 0.88–0.96 range, the outer LCO is weakly unstable; see Fig. 39. Note that at Mach 0.88, the inner LCO is still stable, but at Mach 0.90 both the inner and outer LCOs are unstable. Finally, at Mach 0.96, the inner and outer LCOs eventually merge.

A slight increase in Mach number, from 0.96 to 0.965, results in two *stable* nested LCOs reappearing; see Fig. 40(a). With a further slight increase in the Mach number to 0.97, both the inner and outer limit cycles "evaporate" and the wing amplitudes decay to zero, Fig. 40(b) and (c). Although the LCOs have disappeared, there remains a high sensitivity of the aeroelastic response to the strength of the initial condition. At Mach 0.99, a small LCO reappears (not shown). The stabilization of the flutter mode at high transonic Mach numbers is believed connected with the progressive rearward movement of the shocks, which close to Mach 1 are at or near the trailing edge. Once the shocks have reached the trailing edge, they more or less become stuck and do not move much during an LCO cycle, unless trailing-edge separation occurs. The lack of shock mobility greatly decreases the destabilizing effect of the shocks, as documented in an earlier study based on 2D typical section models [43]. At these high transonic Mach numbers (0.95–1.0), transition
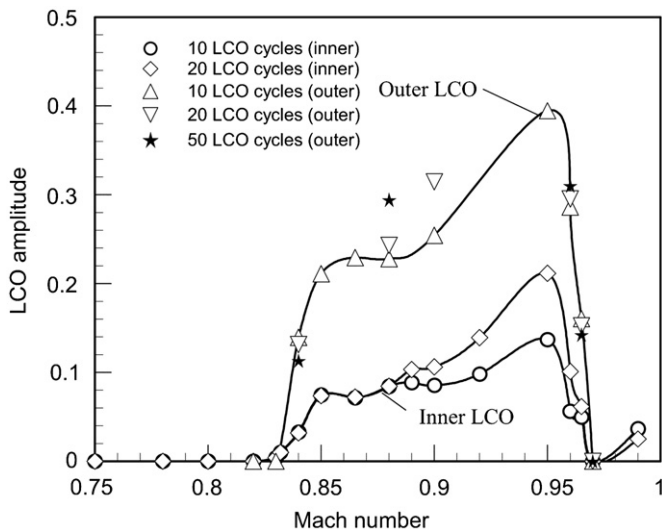
Fig. 36. Multiple limit cycle flutter branches in transonic region. LCOs are weakly unstable in the Mach number range 0.88–0.95, but can be stabilized by increasing the air density (lower density altitude).

Fig. 37. Limit cycle flutter amplitude (wing tip trailing edge) vs. altitude at a constant Mach number of (a) 0.865 and (b) 0.95. The LCO amplitudes shown correspond to the inner LCO, reached through a small perturbation from the equilibrium state. Above about 35,000 ft, both LCOs are weakly unstable at Mach 0.95 and eventually morph into each other.

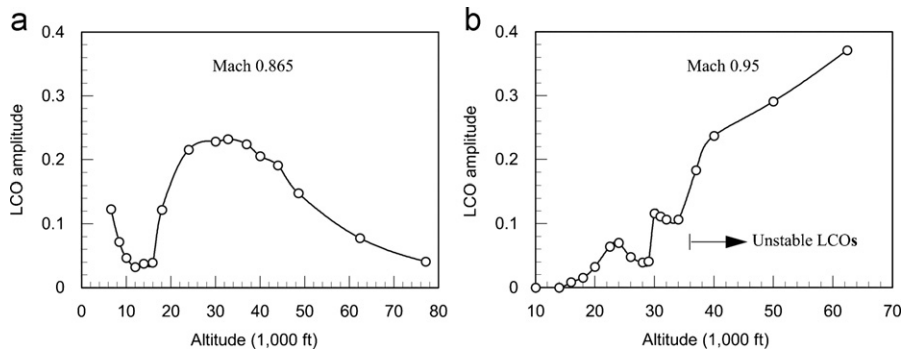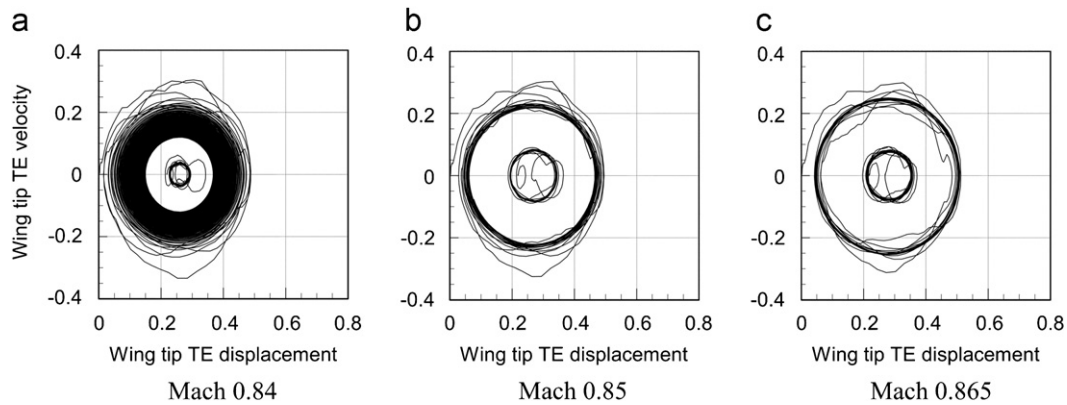**Fig. 38.** Nested LCOs of different amplitudes of the G-Wing at low transonic Mach numbers at a density altitude of 10,000 m (32,800 ft). Both inner and outer LCOs are stable.
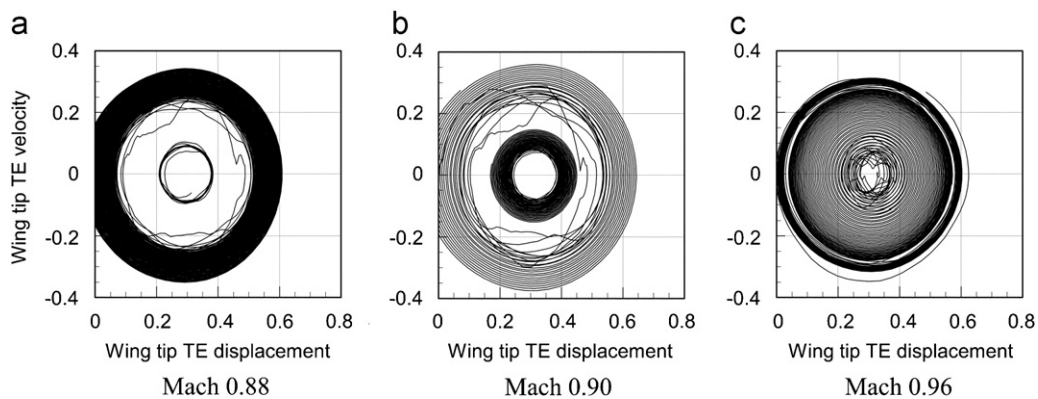

Fig. 39. Nested LCOs of different amplitudes of the G-Wing at intermediate to high transonic Mach numbers at a density altitude of 10,000 m (32,800 ft). All LCOs except the inner LCO at Mach 0.88 are weakly unstable.
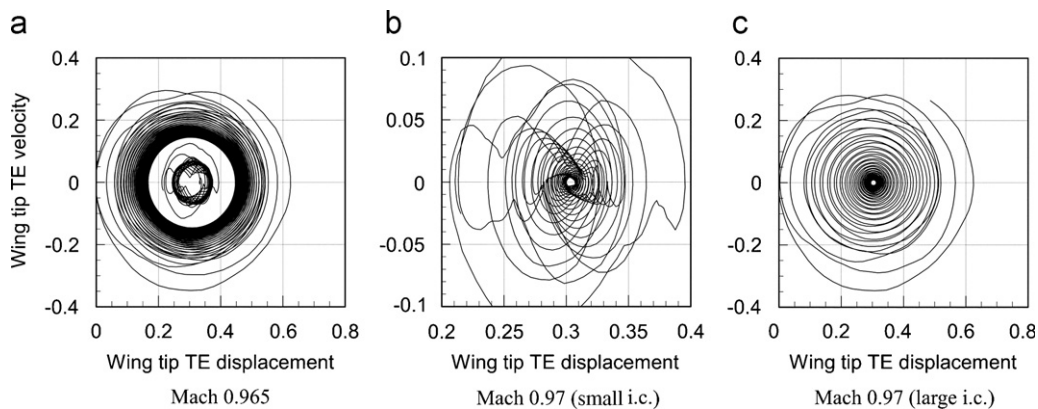

Fig. 40. Rapid transition of LCO behavior at upper end of transonic region and evaporation of LCOs at Mach 0.97.

from Type A to B shock motion does not occur, but the overall effect of the nonlinear transonic flow-field around the wing is typically strongly stabilizing, quenching the flutter or suppressing the limit cycle to very small amplitudes.

7.3. Transonic sweep-back theory

For high-aspect-ratio wings, classical sweep-back theory can be used to estimate the effect of sweep on the subsonic flutter boundary. The effect of aft sweep is predicted to be stabilizing, in agreement with wind tunnel tests by Barmby et al. [119], although the benefit is usually less than what would be predicted

based on classical sweep-back theory. Recent calculations [123] on two unswept versions of the G-Wing suggest that classical sweep-back theory is not applicable in the transonic region. This should not come as a surprise, as the classical theory is based on the superposition principle, which breaks down in the strongly nonlinear transonic region.

The effect of wing sweep was shown in Ref. [126] to be much more difficult to assess than in the linear subsonic case, for two reasons. First, the fundamental assumptions behind classical sub-sonic sweepback theory simply do not hold for transonic flows, because of the nonlinear nature of the flow-field. That is, decom-position of the relative flow velocity U_∞ into components $U_\infty \cos \Lambda$ and $U_\infty \sin \Lambda$ normal and parallel to the line of aerodynamic centers,

and then discarding the spanwise component in the calculations of lift and moment, will lead to incorrect results as soon as the Mach number exceeds the critical Mach number M_{cr}. In the transonic region of practical interest for transport aircraft with swept wings, wherein the far field velocity is less than or close to one (subsonic), $M_{cr} \leq M_\infty \leq 1$, classical sweepback theory should not be used in aerodynamic or aeroelastic calculations.

Second, because structural washout caused by time-varying wing deflections influences the instantaneous shock positions and shock dynamics, it also affects the transonic flutter behavior of the wing. For a flexible wing, the effective structural washout is not only a function of the sweep angle but also of the wing deflections, and hence also the wing loading at a particular operating point. As a result, the effect of wing sweep on the flutter of transonic wings cannot be studied without also considering the wing deformations caused by the mean aerodynamic loads, as a function of angle of attack and dynamic pressure at a given transonic Mach number. Aft sweep is shown to be *destabilizing* for some high-aspect-ratio wings, which is opposite to what classical sweepback theory predicts. This observation may provide additional insight into past flutter instabilities observed in wind tunnel and flight tests of highly swept wings.

7.4. Delayed flutter

The Hopf bifurcation theorem implies that small stable limit cycles do exist in the supercritical case, and that a linear flutter boundary also exists, because the motion amplitude can be made infinitesimally small by adjusting the speed (or Mach number, or mass ratio) such that the bifurcation point is approached from above. But this also implies that no nonuniformities can occur on the time scale, which is not generally true if nonlinear mode interactions occur or nonlinear parametric excitations are present, as in the underlying unsteady aerodynamics problem for transonic flutter. In both cases, the time invariance implicit in harmonic solutions of the linearized equations is destroyed, and a regular perturbation expansion will fail.

The appearance of nonuniformities on the time scale affects stability by destroying time invariance – a concept taken for granted in linear flutter analyses – and stable solutions may not necessarily be uniformly stable in the Liapunov sense. The practical consequences of all of this is that a linear flutter boundary may not exist, because the stability of a given aeroelastic mode may depend on time, and a stable mode may suddenly become unstable after a sufficiently long time, or vice versa. Limit cycles are similarly affected, and an apparently stable limit cycle may suddenly become unstable and abruptly decay to zero and vanish, or turn into explosive delayed flutter. Examples of these types of behaviors are shown in Fig. 41.

7.5. Anomalous mass ratio scaling

Near the transonic dip the flutter speed dependence on mass ratio does not approach the square-root scaling expected from linear subsonic theories. Calculations reveal two surprises: (1) a significant drop in the flutter dynamic pressure as the mass ratio becomes sufficiently large to allow the "naked" SDOF torsional flutter instability to emerge [87] and (2) a *period-tripling* bifurcation of the flutter mode at very low mass ratios ($\mu < 10$) [124].

The anomalous μ-scaling and the SDOF torsional instability are closely related to the "almost singular" (a.s.) behavior of the lift curve slope. The scaling could be relevant in wind tunnel tests, where the mass ratio often varies over a significant range in a single model test. Fig. 42 shows the dependence of the transonic flutter boundary on mass ratio μ, for the NACA 0012 Benchmark Model at

Weak divergence phenomenon (NACA 0012 model; $M_\infty = 0.80$; $\mu = 25$; $\bar{U} = 2.5$; $r_\alpha = 0.5$; $g = 0.0024$; $\dot{h}(0)/b = 0.005$).

Same case as a), but with a slightly larger initial condition, which results in explosive delayed flutter ($\dot{\alpha}(0) = 0.01$).

Initial flutter mode is stable, but not uniformly stable. Nonlinear interactions with weak divergence mode eventually trigger delayed flutter. (NACA 0012 model; $M_\infty = 0.80$; $\mu = 50$; $\bar{U} = 3.05$; $r_\alpha = 0.5$; $g = 0.0024$; $\dot{h}(0)/b = 0.03$).

Delayed flutter emerging from a limit cycle (NACA 0012 model; $M_\infty = 0.80$; $\mu = 75$; $\bar{U} = 3.6$; $g = 0.0$; $\dot{h}(0)/b = 0.03$).
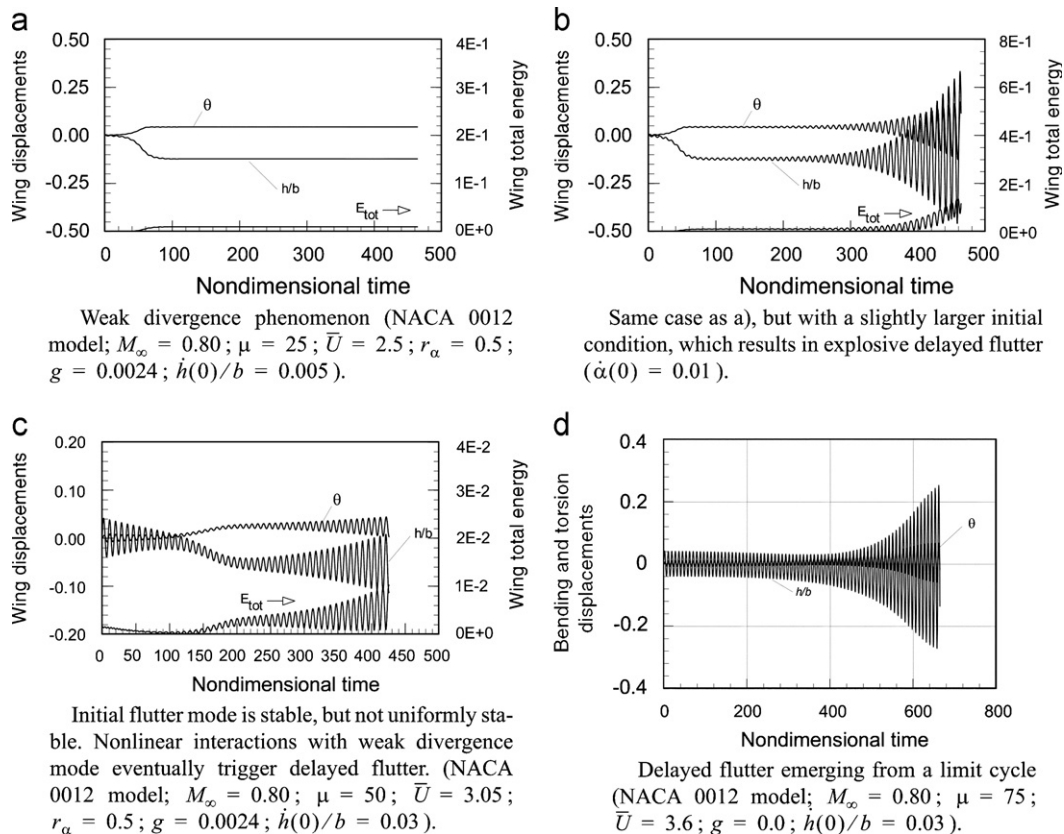
Fig. 41. Some of the aeroelastic consequences of temporal nonuniformities and nonlinear mode interactions.

the bottom of the transonic dip ($M_\infty = 0.85$). At high mass ratios a significant drop in the flutter dynamic pressure occurs as the SDOF torsional flutter instability emerges, replacing the bending–torsion instability. At very low mass ratios, a period-tripling bifurcation of the flutter mode is observed; see Section 7.6. As the mass ratio is increased through the range from 10 to 200, the flutter mode undergoes a continuous transition from a bending–torsion mode where bending dominates to a mode where torsion dominates. For mass ratios of roughly 400 and above, the pure SDOF torsional flutter instability can be observed, Fig. 26. As the SDOF torsional

flutter emerges, the reduced airspeed $\overline{U}_F$ at flutter approaches an asymptotic value close to $1/k_\alpha^c$, where k_α^c is the critical (maximum) reduced frequency at which SDOF torsional flutter is possible for this model at this Mach number and angle of attack. Simultaneously, the speed index and the dynamic pressure at flutter continue to drop with increasing μ, as shown in Fig. 42.

These phenomena are surprising and a clear warning that in the strongly nonlinear transonic region, our classical picture of flutter is in need of revision. There are two implications of these results that may be of practical consequence. First, because of the different mass ratio scaling in the transonic flutter problem, care must be exercised when constructing scaled wind tunnel flutter models, and also in the planning of transonic flutter tests. If the mass ratio of the model is too high or too low, the experimentally obtained transonic flutter boundary *cannot be scaled* to physically similar full-scale dynamic pressures, and the two-parameter flutter boundary may be misleading. Second, the presence of the SDOF torsional flutter at the bottom of the transonic dip – for sufficiently high mass ratios – may have implications for transonic flight at high altitudes. The implications are most serious for thin, heavy wings, typical of fighter aircraft and some UAVs.

Fig. 42. Flutter boundary vs. mass ratio for the NACA 0012 Benchmark model at $M_\infty = 0.85$ ($r_\alpha^2 = 0.25$ and $g = 0.0024$ in these calculations).

7.6. Period tripling flutter

As the mass ratio is lowered, the reduced frequency at which flutter occurs increases. Below a mass ratio of roughly 2–5, linear
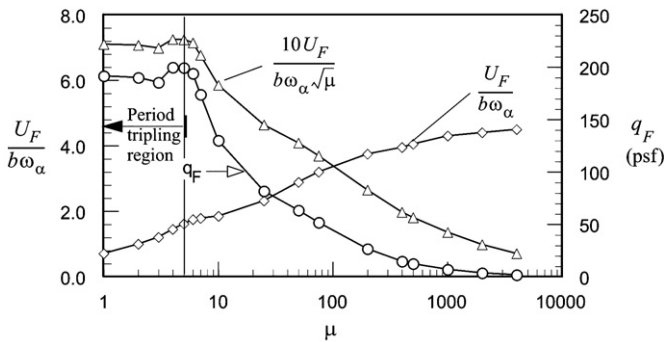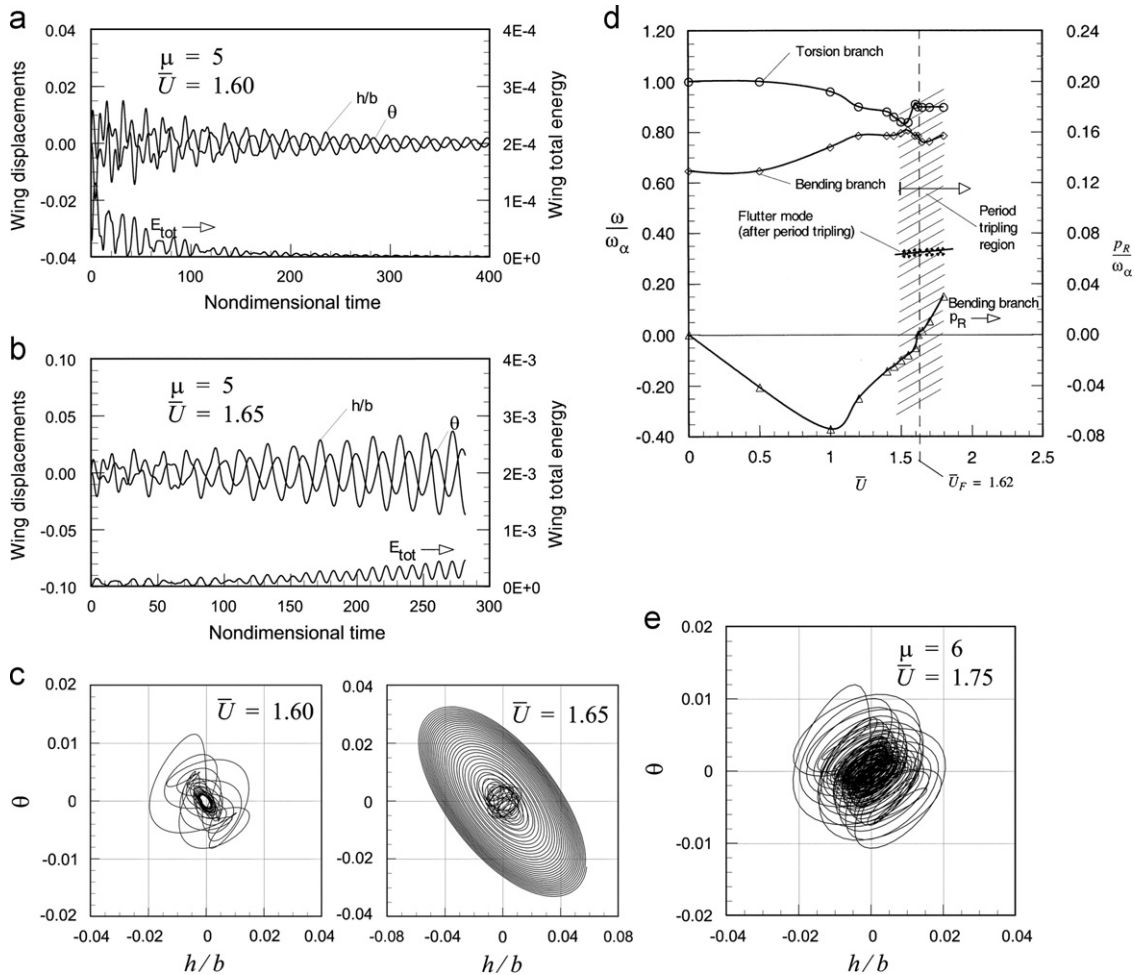

Fig. 43. Emergence of period tripling flutter at low mass ratio: (a) immediately below flutter boundary (note tripling has already occurred); (b) slightly above flutter boundary; (c) phase plots corresponding to (a)–(b); (d) frequency and damping plots for aeroelastic modes when period tripling occurs, for $M_\infty = 0.85$; $\mu = 5$, as determined from Euler-based time-marching solutions; and (e) phase plot suggesting almost-periodic or chaotic flutter (NACA 0012 Model; $g = 0.0024$).

theories predict that flutter should become impossible and that the flutter speed should approach infinity; see, for example the calculations by Ashley [42]. But in the case of the NACA 0012 Benchmark model, this does not happen; instead, the aerodynamic nonlinearities open up a new route to flutter through a period-tripling bifurcation that lowers the reduced frequency into the unstable range; see Fig. 43. This flutter occurs outside the first bending–first torsion frequency interval and cannot be understood within a linear flutter analysis framework [124].

During the period tripling shown in Fig. 43, the reduced frequency of the critical aeroelastic mode drops from 0.49 to 0.19, and at the same time the phase angle by which torsion lags bending increases from close to zero to about 120°. At slightly higher mass ratios, a complex quasi-periodic or possibly almost-periodic flutter mode emerges. The corresponding phase plot, Fig. 43(e), reveals trajectories that suggest chaotic or "almost periodic" motion.

8. Concluding remarks

The mathematical theory of unsteady transonic flow may seem too abstract for the typical aeroelastician or practicing flutter engineer. In an age where CFD codes have become so common-place and computers so powerful that anyone can run nonlinear transonic flutter calculations from a laptop computer, one might ask whether there is a need for a theory in the classical sense. Why not simulate everything, and then just interpret the results—as done in a wind tunnel test, for example? The problem with this approach is that one is likely to end up with a mountain of data, but not necessarily with a better physical understanding of transonic flutter.

Transonic flutter is rich in nonlinear dynamic phenomena that cannot simply be modeled with ideas based on linear aerodynamics. Superficially, the dynamics may appear similar to the nonlinear behaviors of classical mechanical systems. But there are important mathematical and physical differences. First, aeroelastic systems are essentially nonconservative involving circulatory forces and cannot be modeled simply as dissipative mechanical spring–mass–damper systems, with a damping that becomes negative as the flutter boundary is crossed. Second, in the transonic case entropy production at the moving shocks introduces a type of irreversibility that is not found in the corresponding mechanical system, and which results in entropy and vorticity waves being convected downstream, affecting the global aerodynamic solution and possibly also the stability of the fluid–structure system.

In transonic flutter, nonuniformities on the time scale affect stability by destroying time invariance, and stable solutions may not necessarily be uniformly stable. In some cases a linear flutter boundary may not exist, because the stability of a given aeroelastic mode may depend on time, and a stable mode may suddenly become unstable after a sufficiently long time, or vice versa. Limit cycles are similarly affected, and an apparently stable limit cycle may suddenly become unstable and abruptly decay to zero and vanish, or turn into explosive flutter. These phenomena can all be explained by the mathematical theory of unsteady transonic flow.

The existence of multiple LCOs and the possible morphing between semistable and stable LCOs brings up important code verification and validation issues. The logical separation of the verification step [127] (solving the equations right) and the validation step (solving the right equations) breaks down and becomes fuzzy, to say the least, and the two steps may become impossible to separate from a practical standpoint. The experimentalist is faced with similar difficulties in trying to understand the flutter test results and "validate" the data. In aeroelastic systems exhibiting multiple LCOs sensitive to initial conditions

and control parameters, this is a daunting problem that may require new experimental and computational techniques.

References

[1] von Kármán T. The similarity law of transonic flow. Journal of Mathematics and Physics 1947;26(3):182–90.
[2] Cole JD. Problems in transonic flow. PhD thesis. Pasadena, CA: California Institute of Technology; 1949.
[3] Guderley G, Yoshihara H. The flow over a wedge profile at Mach number 1. Journal of the Aeronautical Sciences 1950;17(11):723–35.
[4] Cole JD. Drag of a finite wedge at high subsonic speeds. Journal of Mathematics and Physics 1951;30(2):79–93.
[5] Spreiter JR. On the application of transonic similarity rules to wings of finite span. NACA Report 1153, 1953.
[6] Spreiter JR. On alternate forms for the basic equations of transonic flow theory. Journal of the Aeronautical Sciences 1954;21(1):70–2.
[7] Hayes WD. Pseudotransonic similitude and first-order wave structure. Journal of the Aeronautical Sciences 1954;21:721–30.
[8] Cole JD, Messiter AF. Expansion procedures and similarity laws for transonic flow. Zeitschrift für Angewandte Mathematik und Physik 1957;8:1–25.
[9] Liepmann HW, Askenas H, Cole JD. Experiments in transonic flow. USAF Technical Report 5667, Wright-Patterson Air Force Base, 1948.
[10] Ackeret J, Feldman F, Rott N. Investigation of compression shocks and boundary layers in gases moving at high speeds. NACA technical memorandum no. 113, 1947 (translated from ETH, Zurich, Report 10, 1946).
[11] Guderley KG. The theory of transonic flow. Reading, MA: Addison-Wesley; 1962.
[12] Ferrari C, Tricomi FG. Transonic aerodynamics. New York: Academic Press; 1968.
[13] Cole JD. Perturbation methods in applied mathematics. Waltham, Massachusetts: Blaisdell; 1968.
[14] Lagerstrom PA. Matched asymptotic expansions. New York: Springer-Verlag; 1988.
[15] Cole JD, Cook LP. Transonic aerodynamics. Amsterdam: Elsevier Science Publishers; 1986.
[16] Moulden TH. Fundamentals of transonic flow. New York: John Wiley & Sons; 1984.
[17] Ramm HJ. Fluid dynamics for the study of transonic flow. New York: Oxford University Press; 1990.
[18] Kuz'min AG. Boundary value problems for transonic flow. West Sussex, England: John Wiley & Sons, Ltd; 2002.
[19] Oswatitsch K, editor. Symposium transsonicum I. Berlin: Springer-Verlag; 1962.
[20] Oswatitsch K, Rues D, editors. Symposium transsonicum II. Berlin: Springer-Verlag; 1975.
[21] Zierep J, Oertel H, editors. Symposium transsonicum III. Berlin: Springer-Verlag; 1988.
[22] Sobieczky H, editor. IUTAM symposium transsonicum IV. Dordrecht, The Netherlands: Kluwer Academic Publishers; 2003.
[23] Nixon D, editor. Progress in astronautics and aeronautics, vol. 120. Washington, DC: AIAA; 1989.
[24] Murman EM, Cole JD. Calculations of plane steady transonic flows. AIAA Journal 1971;9(1):114–21.
[25] Caughey DA, Jameson A. Development of computational techniques for transonic flows: an historical perspective. In: Sobieczky H, editor. IUTAM symposium transsonicum IV. The Netherlands: Kluwer Academic Publishers; 2003. p. 183–94.
[26] Jameson A. Requirements and trends of computational fluid dynamics as a tool for aircraft design. In: Proceedings of the 12th NAL symposium on aircraft computational aerodynamics, Tokyo, Japan, June 1994.
[27] Edwards JW, Malone JB. Current status of computational methods for transonic unsteady aerodynamic and aeroelastic applications. Paper no. 1, AGARD structures and materials panel specialist's meeting on transonic unsteady aerodynamics and aeroelasticity, San Diego, CA, October 9–11, 1991.
[28] Edwards JW. Computational aeroelasticity. In: Noor N, Venneri S, editors. Flight vehicle materials, structures and dynamics, vol. 5, structural dynamics and aeroelasticity. New York: ASME; 1993. [Chapter 7].

[29] Bendiksen OO. Modern developments in computational aeroelasticity. Journal of Aerospace Engineering, Proceedings of the Institution of Mechanical Engineers Part G 2004;218(3):157–78.

[30] Cole JD. Modern developments in transonic flow. SIAM Journal on Applied Mathematics 1975;29(4):763–87.

[31] Tijdeman H, Seebass R. Transonic flow past oscillating airfoils. Annual Reviews of Fluid Dynamics 1980:181–222.

[32] Dowell EH, Edwards J, Strganac T. Nonlinear aeroelasticity. Journal of Aircraft 2003;40(5):857–74.

[33] de C Henshaw MJ, Badcock KJ, Vio GA, Allen CB, Chamberlain J, Kaynes I, et al. Non-linear aeroelastic prediction for aircraft applications. Progress in Aerospace Sciences 2007;43(4–6):65–137.

[34] Landahl MT. Unsteady transonic flow. New York: Pergamon Press; 1961.

[35] Landahl MT. Some developments in unsteady transonic flow research. In: Oswatitsch K, Rues D, editors. Symposium transsonicum II. Berlin: Springer-Verlag; 1975.

[36] Dowell EH, Hall KC. Modeling of fluid–structure interaction. Annual Review of Fluid Mechanics 2001;33:445–90.

[37] Doggett RV Jr, Rainey AG, Morgan HG. An experimental investigation of aerodynamic effects of airfoil thickness on transonic flutter characteristics. NASA TM X-79, 1959.

[38] Schewe G, Knipfer A, Henke H. Experimentelle und numerische Untersuchung zum transonischen Flügelflattern im Hinblick auf. Unpublished manuscript, February 1999.

[39] Van Dyke M. Perturbation methods in fluid dynamics. Stanford, CA: The Parabolic Press; 1975.

[40] Kevorkian J, Cole JD. Perturbation methods in applied mathematics. New York: Springer-Verlag; 1981.

[41] Bendiksen, OO. Improved similarity rules for transonic flutter. AIAA paper 99-1350. In: Proceedings of the 40th AIAA/ASME/ASCE/AHS/ASCE SDM conference, St. Louis, MO, April 12–15, 1999.

[42] Ashley H. Role of shocks in the 'sub-transonic' flutter phenomenon. Journal of Aircraft 1980; 17(3):187–97.

[43] Bendiksen OO. Role of shock dynamics in transonic flutter. AIAA paper 92-2121. In: Proceedings of the AIAA dynamics specialists conference, Dallas, TX, April 16–17, 1992. p. 401–14.

[44] Bendiksen OO. Influence of shocks on transonic flutter of flexible wings. AIAA paper 2009-2313. In: Proceedings of the AIAA/ASME/ASCE/AHS/ASC 50th SDM conference, Palm Springs, CA, May 2009.

[45] Cole JD. Review of transonic flow theory. AIAA paper 82-0104, 1982.

[46] Steinhoff J, Jameson A. Multiple solutions of the transonic potential flow equation. AIAA Journal 1982;20(11):1521–5.

[47] Jameson A. Airfoils admitting nonunique solutions of the Euler equations. AIAA paper 91-1625, June 1991.

[48] Caughey DA. Unsteady transonic flow past "non-unique" airfoils. In: Sobieczky H, editor. IUTAM symposium transsonicum iv. The Netherlands: Kluwer Academic Publishers; 2003. p. 41–6.

[49] Hafez M. Non-uniqueness problem in transonic flows. In: Sobieczky H, editor. IUTAM symposium transsonicum IV. The Netherlands: Kluwer Academic Publishers; 2003. p. 33–40.

[50] Bendiksen OO. Nonunique solutions in transonic aeroelasticity. In: Proceedings of the international forum on aeroelasticity and structural dynamics, Rome, Italy, June 17–20, 1997. p. 425–35.

[51] Kousen KA, Bendiksen OO. Nonlinear aspects of the transonic aeroelastic stability problem. AIAA paper 88-2306. In: Proceedings of the AIAA/ASME/ASCE/AHS/ASCE 29th SDM conference, Williamsburg, VA, April 18–20, 1988. p. 760–9.

[52] Kousen KA, Bendiksen OO. Limit cycle phenomena in computational transonic aeroelasticity. Journal of Aircraft 1994;31(6):1257–63.

[53] Prandtl L, Titjens OG. Fundamentals of hydro- and aeromechanics. New York: Dover Publications; 1957.

[54] Courant R, Hilbert D. Methods of mathematical physics, vol. II. New York: Interscience; 1962.

[55] Bartels RE. Development of advanced computational aeroelasticity tools at NASA Langley Research Center. Paper AVT-RTO-154-007, NATO AVT-154 specialists' meeting on advanced methods in aeroelasticity, Loen Norway, May 5–8, 2008.

[56] Schuster DM. NASA perspective on requirements for development of advanced methods predicting unsteady aerodynamics and aeroelasticity. Paper AVT-RTO-154-011, NATO AVT-154 specialists' meeting on advanced methods in aeroelasticity, Loen Norway, May 5–8, 2008.

[57] Fureby C. Towards the use of large eddy simulation in engineering. Progress in Aerospace Sciences 2008;44(6):381–96.

[58] Davis GA, Bendiksen OO. Transonic panel flutter. AIAA paper 93-1476, April 1993.

[59] Bryson AE. An experimental investigation of transonic flow past two-dimensional wedge and circular-arc sections using a Mach–Zehnder interferometer. NACA technical note 2560, 1951.

[60] Liepmann HW, Roshko A. Elements of gas dynamics. New York: John Wiley & Sons; 1957.

[61] Jameson A, Schmidt W, Turkel E. Numerical solutions of the Euler equations by finite volume methods using Runge–Kutta time-stepping Schemes. AIAA paper 81-1259. In: AIAA 14th fluid and plasma dynamics conference, Palo Alto, California, June 1991.

[62] Chakravarthy S, Harten A, Osher S. Essentially non-oscillatory shock capturing schemes of uniformly very high accuracy. AIAA paper 86-0339. In: AIAA 24th aerospace sciences meeting, Reno, NV, 1986.

[63] Jameson A. Time-dependent calculations using multigrid, with applications to unsteady flows past airfoils and wings. AIAA paper 91-1596, June 1991.

[64] Bendiksen OO, Hwang G. Nonlinear flutter calculations for transonic wings. In: Proceedings of the international forum on aeroelasticity and structural dynamics, Rome, Italy, June 17–20, 1997. p. 105–14.

[65] Mavriplis D. Unstructured grid techniques. Annual Review of Fluid Mechanics 1997;29:473–514.

[66] Jameson A, Mavriplis DJ. Finite volume solution of the two-dimensional Euler equations on a regular triangular mesh. AIAA paper 85-0435, January 1985.

[67] Mavriplis DJ. Accurate multigrid solution of the Euler equations on unstructured and adaptive meshes. AIAA Journal 1990;28(2):213–21.

[68] Davis GA, Bendiksen OO. Unsteady transonic two-dimensional Euler solutions using finite elements. AIAA Journal 1993;31(6):1051–9.

[69] Hwang G. Parallel finite element solutions of nonlinear aeroelastic and aeroservoelastic problems in three-dimensional transonic flows. Ph.D. dissertation, Mechanical and Aerospace Engineering Department, University of California, Los Angeles, CA, March 1997.

[70] Bendiksen OO. A new approach to computational aeroelasticity. AIAA paper 91-0939. In: Proceedings of the AIAA/ASME/ASCE/AHS/ASC 32nd SDM conference, Baltimore, MD, April 8–10, 1991. p. 1712–27.

[71] Seber G, Bendiksen OO. Nonlinear flutter calculations using finite elements in a large deformation direct Eulerian–Lagrangian formulation. AIAA Journal 2008;46(6):1331–41.

[72] Theodorsen T, Garrick I. Mechanism of flutter—a theoretical and experimental investigation of the flutter problem. NACA report no. 685, 1940.

[73] Garrick I. Bending–torsion flutter calculations modified by subsonic compressibility corrections. NACA report no. 836, 1946.

[74] Bendiksen OO. Transonic similarity rules for flutter and divergence. AIAA paper 98-1726, AIAA/ASME/ASCE/AHS/ASCE 39th SDM conference, Long Beach, CA, April 20–23, 1998.

[75] Sichel M. Solution of the viscous transonic equation for flow past a wavy wall. US Army Research Office Report 01361-1-T, May 1970.

[76] Sichel M. Two-dimensional shock structures in transonic and hypersonic flows. Advances in applied mechanics, vol. 11. New York: Academic Press; 1971. p. 131–207.

[77] Edwards J. Transonic shock oscillations calculated with a new interactive boundary layer coupling method. AIAA paper 93-0777, 1993.

[78] Raveh D, Dowell EH. Frequency lock-in phenomenon in oscillating airfoils in buffeting transonic flows. Paper IFASD-2009-135. International forum on structural dynamics and aeroelasticity 2009, Seattle, WA, June 21–25, 2009.

[79] Gad GE. The possibility of normal shock waves on a body with convex surfaces in inviscid transonic flow. Zeitschrift für Angewandte Mathematik und Physik 1960;11:51–5.

[80] Oswatitsch K, Zierep J. Das Problem des Senkrechten Stossen an einer gekrümmten Wand. Zeitschrift für Angewandte Mathematik und Mechanik 1960(Suppl.):143–4.

[81] Pearcy HH. Some effects of shock-induced separation of turbulent boundary layers in transonic flow past aerofoils. In: Proceedings of the national physical laboratory symposium on boundary layer effects in aerodynamics, 1955.

[82] Zierep J. New results for the normal shock in inviscid flow at a curved surface. In: Sobieczky H, editor. IUTAM symposium transsonicum IV. The Netherlands: Kluwer Academic Publishers; 2003. p. 1–6.

[83] Davis GA. Transonic aeroelastic solutions using finite elements in an arbitrary Lagrangian–Eulerian formulation. PhD dissertation, Department of Mechanical, Aerospace and Nuclear Engineering, University of California, Los Angeles, CA, 1994.

[84] Landon RH. NACA 0012 oscillatory and transient pitching. In: Compendium of unsteady aerodynamic measurements, data set 3, AGARD-R-702, August 1982.

[85] Liu F, Ji S. Unsteady flow calculations with a multigrid Navier–Stokes method. AIAA Journal 1996;34(10):2047–53.

[86] Davis SS. NACA 64A010 (NASA Ames model) oscillatory pitching. In: Compendium of unsteady aerodynamic measurements, data set 2, AGARD-R-702, August 1982.

[87] Bendiksen OO. Transonic flutter. AIAA paper 2002-1488. In: AIAA/ASME/ASCE/AHS/ASC 43rd SDM conference, Denver, CO, April 22–25, 2002.

[88] Kuethe AM, Chow C-Y. Foundations of aerodynamics. 5th ed.. New York: John Wiley & Sons; 1998. p. 318–9.

[89] Howarth L, editor. Modern developments in fluid dynamics—high speed flow. Oxford: Claredon Press; 1953.

[90] Göthert BH. Profilmessungen im Hochgeschwindigkeitskanal 2.7m.D. Deutsche Luftfahrtforschung, F.B 1941;1490.

[91] Bendiksen OO. Transonic flutter prediction. In: Proceedings of the international forum on aeroelasticity and structural dynamics 2003, Amsterdam, The Netherlands, June 4–6, 2003.

[92] Rivera AJ Jr, Dansberry BE, Bennett RM, Durham MH, Silva WA. NACA 0012 Benchmark model experimental flutter results with unsteady pressure distributions. NASA TM 107581, March 1992.

[93] Knipfer A, Schewe G. Investigation of an oscillating supercritical 2D wing section in a transonic flow. AIAA paper 99-0653, January 1999.

[94] Schewe G, Knipfer A, Mai H, Dietz G. Experimentelle und numerische Untersuchung nichtlineare Effecte beim transonischen Flattern. DLR IB 232-2001 J03, 2001.

[95] Schewe G, Mai H, Dietz G. Nonlinear effects in transonic flutter with emphasis on manifestations of limit cycle oscillations. Journal of Fluids and Structures 2003;18(1):3–22.

[96] Försching HW. Challenges and perspectives in computational aeroelasticity. In: Proceedings of the international forum on aeroelasticity and structural dynamics, Manchester, England, 1995. p. 1.1–1.9.

[97] Tijdeman H. Investigations of the transonic flow around oscillating airfoils. Doctoral dissertation, Technical University of Delft, The Netherlands, December 1977.

[98] Silva WA, Keller DF, Florance JR, Cole SR, Scott RC. Experimental steady and unsteady aerodynamic and flutter results for HSCT semispan models. AIAA paper 2000-1697, 2000.

[99] Gursul I, Gordnier R, Visbal M. Unsteady aerodynamics of nonslender delta wings. Progress in Aerospace Sciences 2005;41(7):515–57.

[100] Edwards J. Numerical simulations of shock/boundary layer interactions using time-dependent modeling techniques: a survey of recent results. Progress in Aerospace Sciences 2008;44(6):447–65.

[101] Runyan HL. Single-degree-of-freedom flutter calculations for a wing in subsonic potential flow and comparison with an experiment. NACA report, no. 1089, 1952.

[102] Bisplinghoff RL, Ashley H. Principles of aeroelasticity. New York: John Wiley & Sons; 1962.

[103] Bratt JB, Chinneck A. Measurements of mid-chord pitching moment derivatives at high speed. ARC R&M 2680, 1954.

[104] Bratt JB, Raymer WG, Townsend JEG. Measurements of the direct pitching-moment derivatives for two-dimensional flow at subsonic and supersonic speeds and for a wing of aspect ratio 4 at subsonic speeds. ARC R&M 3257, 1962.

[105] Lambourne NC. Some instabilities arising from the interactions between shock waves and boundary layers. AGARD report, no. 182, April 1958.

[106] Jones WP. Research on unsteady flow. Journal of the Aerospace Sciences 1963;29(3):249–63.

[107] Whitehead DS. Torsional flutter of unstalled cascade blades at zero deflection. ARC R&M 3429, 1964.

[108] Platzer MF, Chalkey HG. Theoretical investigation of supersonic cascade flutter and related interference problems. AIAA paper 72-377, 1972.

[109] Verdon JM, McCune JE. Unsteady supersonic cascade in subsonic axial flow. AIAA Journal 1975;13(2):193–201.

[110] Bendiksen OO, Friedmann PP. Coupled bending–torsion flutter in a supersonic cascade. AIAA Journal 1981;19(6):774–81.

[111] Bendiksen OO. Aeroelastic problems in turbomachines. In: Noor A, Venneri S, editors. Flight-vehicle materials, structures and dynamics, vol. 5: structural dynamics and aeroelasticity. New York: American Society of Mechanical Engineers; 1993. [Chapter 5].

[112] Bendiksen OO. Transonic bending flutter in rotors and cascades. In: Ferrand P, Aubert S, editors. Proceedings of the ninth international symposium on unsteady aerodynamics, aeroacoustics and aeroelasticity of turbomachines, Lyon, France, September 4–7, 2000. Grenoble University Presses, 2000. p. 791–802.

[113] Bendiksen OO. Transonic limit cycle flutter/LCO. AIAA paper 2004-1694. In: Proceedings of the 45th AIAA/ASME/ASCE/AHS/ASC structures, structural dynamics, and materials conference, Palm Springs, CA, April 19–22, 2004.

[114] Schewe G, Knipfer A, Mai H, Dietz G. Nonlinear effects in transonic flutter. international forum on structural dynamics and aeroelasticity 2001, Madrid, Spain, June 2001.

[115] Bendiksen OO. Multiple limit cycles in transonic flow and some computational and experimental implications. Paper AVT-152-024. In: NATO AVT-152 symposium on limit cycle oscillation and other amplitude-limited self excited oscillations, Loen, Norway, May 5–8, 2008.

[116] Thomas JP, Dowell EH, Hall KC. Modeling viscous transonic limit cycle oscillation behavior using a harmonic balance approach. AIAA paper 2002-1414. In: AIAA/ASME/ASCE/AHS/ASC 43rd SDM conference, Denver, CO, April 22–25, 2002.

[117] Weber S, Jones KD, Ekaterinaris JA, Platzer MF. Transonic flutter computations for a 2D supercritical wing. AIAA paper 99-0798. In: 36th aerospace sciences meeting and exhibit, Reno, NV, January 1999.

[118] Tang L, Bartels RE, Chen PC, Liu DD. Simulation of transonic limit cycle oscillations using a CFD time-marching method. AIAA paper 2001-1290, AIAA/ASME/ASCE/AHS/ASC 42nd SDM conference, Seattle, WA, April 2001.

[119] Barmby JG, Cunningham HJ, Garrick IE. Study of effects of sweep on the flutter of cantilever wings. NACA report 1014, 1951.

[120] Dietz G, Schewe G, Kiessling F, Sinapius M. Limit-cycle-oscillation experiments at a transport aircraft wing model. In: Proceedings of the international forum on structural dynamics and aeroelasticity, Amsterdam, The Netherlands, June 4–6, 2003.

[121] Bendiksen OO. Transonic limit cycle flutter of high-aspect-ratio swept wings. Journal of Aircraft 2008;45(5):1522–33.

[122] Bendiksen OO. High-altitude limit cycle flutter of transonic wings. Journal of Aircraft 2009;46(1):123–36.

[123] Bendiksen OO. Effect of wing deformations and sweep on transonic limit cycle flutter of flexible wings. Paper IF-031. In: Proceedings of the international forum on aeroelasticity and structural dynamics, Stockholm, Sweden, June 18–20, 2007.

[124] Bendiksen OO. Nonlinear mode interactions and period-tripling flutter in transonic flow. Journal of Fluids and Structures 2004;19(6):591–606.

[125] Daley BN, Dick RS. Effects of thickness, camber, and thickness distribution on airfoil characteristics at Mach numbers up to 1.0. NACA TN 3607, March 1956.

[126] Bendiksen OO. Effect of wing thickness and geometry on transonic flutter. IFASD2009 paper 043. In: International forum on structural dynamics and aeroelasticity, Seattle WA, June 21–25, 2009.

[127] Roache PJ. Verification of codes and calculations. AIAA Journal 1998;36(5):696–702.